

REVIEW

## From contact electrification to triboelectric nanogenerators

To cite this article: Zhong Lin Wang 2021 *Rep. Prog. Phys.* **84** 096502

View the [article online](#) for updates and enhancements.



**IOP | ebooks™**

Bringing together innovative digital publishing with leading authors from the global scientific community.

Start exploring the collection—download the first chapter of every title for free.

## Review

# From contact electrification to triboelectric nanogenerators

Zhong Lin Wang \*<sup>ID</sup>

Beijing Institute of Nanoenergy and Nanosystems, Chinese Academy of Sciences, Beijing, 100083, People's Republic of China  
School of Materials Science and Engineering, Georgia Institute of Technology, Atlanta, GA 30332, United States of America  
School of Nanoscience and Technology, University of Chinese Academy of Sciences, Beijing 100049, China

E-mail: [zhong.wang@mse.gatech.edu](mailto:zhong.wang@mse.gatech.edu)

Received 7 February 2021, revised 26 May 2021

Accepted for publication 10 June 2021

Published 7 September 2021



### Abstract

Although the contact electrification (CE) (or usually called 'triboelectrification') effect has been known for over 2600 years, its scientific mechanism still remains debated after decades. Interest in studying CE has been recently revisited due to the invention of triboelectric nanogenerators (TENGs), which are the most effective approach for converting random, low-frequency mechanical energy (called high entropy energy) into electric power for distributed energy applications. This review is composed of three parts that are coherently linked, ranging from basic physics, through classical electrodynamics, to technological advances and engineering applications. First, the mechanisms of CE are studied for general cases involving solids, liquids and gas phases. Various physics models are presented to explain the fundamentals of CE by illustrating that electron transfer is the dominant mechanism for CE for solid–solid interfaces. Electron transfer also occurs in the CE at liquid–solid and liquid–liquid interfaces. An electron-cloud overlap model is proposed to explain CE in general. This electron transfer model is extended to liquid–solid interfaces, leading to a revision of the formation mechanism of the electric double layer at liquid–solid interfaces. Second, by adding a time-dependent polarization term  $\mathbf{P}_s$  created by the CE-induced surface electrostatic charges in the displacement field  $\mathbf{D}$ , we expand Maxwell's equations to include both the medium polarizations due to electric field ( $\mathbf{P}$ ) and mechanical agitation and medium boundary movement induced polarization term ( $\mathbf{P}_s$ ). From these, the output power, electromagnetic (EM) behaviour and current transport equation for a TENG are systematically derived from first principles. A general solution is presented for the modified Maxwell's equations, and analytical solutions for the output potential are provided for a few cases. The displacement current arising from  $\varepsilon\partial\mathbf{E}/\partial t$  is responsible for EM waves, while the newly added term  $\partial\mathbf{P}_s/\partial t$  is responsible for energy and sensors. This work sets the standard theory for quantifying the performance and EM behaviour of TENGs in general. Finally, we review the applications of TENGs for harvesting all kinds of available mechanical energy that is wasted in our daily life, such as human motion, walking, vibration, mechanical triggering, rotating tires, wind, flowing water and more. A summary is provided about the applications of TENGs in energy science, environmental protection, wearable electronics, self-powered sensors, medical science, robotics and artificial intelligence.

\* Author to whom any correspondence should be addressed.

'Corresponding Editor Professor Horst-Guenther Rubahn'.

**Keywords:** contact electrification, triboelectric nanogenerator, self-powered sensor, displacement current

(Some figures may appear in colour only in the online journal)

## 1. Contact electrification and triboelectricity

Triboelectrification (TE) is one of the most conventional phenomena that occurs in our daily life. TE has been known for more than  $\sim 2600$  years since ancient Greek civilization, and it exists everywhere, anywhere and at any time in our life. When children learn physics in middle school, TE is the first effect introduced about electricity (figure 1(a)). Although this universal phenomenon occurs for all known matter in all phases, solid, liquid and even gas (figure 1(b)), the understanding of the mechanism of TE has been long debated and is still inconclusive. *Nature* published an article on triboelectric charging nearly a century ago, noting ‘this class of research is simple-seeming. But those who have spent time on the subject will allow that it is very baffling; those who have not done so will at least remember that despite great efforts by physicists the subject has not yet passed the pioneer stage’ [1]. Since then, 100 years have passed, and this statement is still true. A recent review by Lacks and Shinbrot [2] covers the important progress made in our understanding of TE in the last century, but the mechanism regarding TE still remains unclear (figure 2). So the questions are what is new about our recent understanding, why do we still care about TE, and what will be the outcome and impact if we fully understand TE?

The scientific term for TE is contact electrification (CE), which means that two different materials (even chemically the same type of materials) become electrically charged after they are separated from physical contact. CE and TE are conventionally treated the same by many readers, but the two have major differences. TE is a ‘convolution’ of CE and friction. CE occurs in TE, but friction is not necessary for charge transfer. Friction includes both production of debris and a friction coefficient. Therefore, CE is a scientific effect in which no friction is necessary, while TE is an engineering operation. Given that CE occurs for solid, liquid and gas phases of almost any materials, and is present in the process of friction, there has been a long debate regarding whether CE is due to electron transfer, ion transfer or even material species transfer. The idea for a role for ion transfer in CE is due to the presence of liquid phases in some cases and the presence of moisture in others, while that for material species transfer is probably due to the practice of mechanical rubbing.

Although TE is a basic effect of electricity, studying the mechanisms of TE is rather cumbersome, for several reasons. First, TE is a very complex process that not only involves the basic processes occurring in tribology, but also interfacial charge exchange and tunneling. Neglecting the distinction between TE and CE has made the study rather difficult. Second, the TE effect occurs for all matter and all phases, so it

is rather challenging to propose a unified physical model that covers such a broad range of materials and phases. Third, the lack of tools for probing nano-scale TE was a major limitation for the field until the invention of Kelvin probe force microscopy (KPFM) [3]. Last, TE has always been regarded as a negative effect due to the fact that it can create electric fires and discharge, disrupt flow [4, 5] and blending [6] in pharmaceutical processing, and lead to increased friction [7] and energy losses [8]. On the other hand, despite TE being the basis of the first technique used by ancient humans to create fire for heating and cooking purposes through friction, there are few uses for TE in today’s advanced technologies.

The interest for studying the mechanism of CE is being revisited owing to the invention of the triboelectric nanogenerator (TENG) [9, 10], which is a fundamental technology for converting irregular, low-frequency and distributed mechanical energy (called high entropy energy) into electric power by using a conjunction of TE and electrostatic induction. The area power density of TENGs has reached  $500 \text{ W m}^{-2}$ , and a conversion efficiency of  $>50\%$  has been demonstrated [11]. TENGs can harvest all kinds of mechanical energy that is ubiquitously available but wasted in our daily lives, such as human motion, walking, vibration, mechanical triggering, rotating tires, wind, flowing water and more, and thus has important applications in the internet of things and networks of distributed energy [12]. Therefore, a fundamental understanding of CE is of great importance for the improvement of TENGs into a major energy technology. Furthermore, TENGs can also be used as self-powered sensors for actively detecting the dynamic processes arising from mechanical agitation using their electrical output signals. Self-powered sensors have potential applications in robotics, soft and flexible electronics and artificial intelligence. Therefore, the invention and future applications of TENGs provide reasons to study the fundamental science of CE, aimed at establishing the scientific basis of this new energy technology and significantly improving its performance. In fact, to our surprise, this is a ‘forgotten corner’ in physics that has not yet been extensively studied.

The objectives of this review are to answer the following fundamental questions based on the studies made in the last two decades: (1) How are the electrostatic charges being created when two materials are physically contacted and what is their physical nature? Our focus is to illustrate the electron transfer between different phases of materials in several interface configurations, such as solid–solid, liquid–solid and liquid–liquid. (2) How do the electrostatic charges on the surfaces of dielectrics drive electrons to flow and give power for TENGs? We expand Maxwell’s equations by introducing the polarization produced by non-electric field terms, and use them

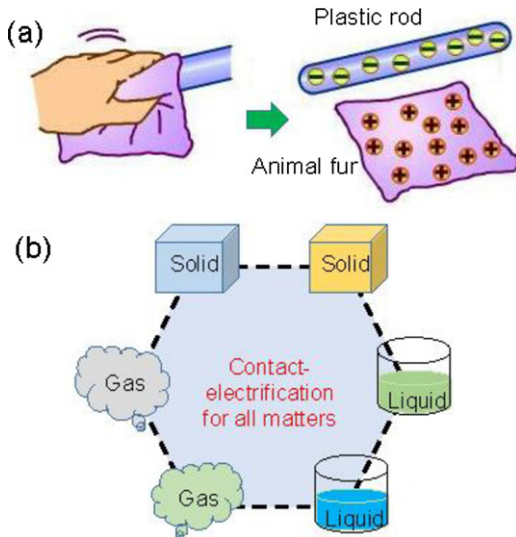


**Figure 1.** Schematic illustration of TE (a) by rubbing a fur against a plastic rod, which is normally the first class for teaching children about electricity. (b) TE is a universal phenomenon that occurs at interfaces between solids, liquids and gases.

and the related first principle theory to derive a theory for TENGs. (3) What are the standards for quantifying the surface charge density as a result of CE? (4) What are the major applications of TENGs? This section is about the technological reasons why we are studying the fundamentals of CE and its technological impacts. The aim of this review is to coherently and comprehensively introduce the science, technology and practical impacts arising from CE.

## 2. Physical mechanisms of CE

Studying the mechanism of TE has been a long history, but there is no self-consistent and unified conclusion. Owing to the nature of TE occurring for solids, liquids and gas, it has been proposed that TE could be due to electron transfer [13], ion transfer [14–16] and/or even material species transfer [17], which means that anything is possible. Considering the presence of water in the ambient atmosphere, it was suggested that  $H^+$  and  $OH^-$  ions from adsorbed water may transfer charges between surfaces [18]. The first-principle simulations [19] on surfaces of alumina and silica support the role of adsorbed water in surface charging:  $OH^-$  may be a dominant charge ion.  $OH^-$  ions are believed to accumulate at interfaces and thus produce the observed electrification [20].

In the solid–solid cases, studying CE at various elevated temperatures and photon excitations has clearly ruled out the contribution made by ion transfer [18, 21]. First, the mechanism of releasing surface charges follows the electron thermionic emission model, which is possible only for electrons. Ion transfer satisfies the Boltzmann distribution [13], which indicates that more triboelectric charges would be transferred at higher temperatures. Second, water plays a very important role in the ion transfer model [22], but fewer surface charges are found experimentally to transfer at higher moisture levels, and maximum charge transfer has been found to

occur at  $\sim 0\%$  relative humidity; moisture tends to discharge the accumulated charges [23]. A recent study carried out for triboelectric charging in oil showed that water is not necessary for CE to occur [24]. Third, CE between Ti-SiO<sub>2</sub> was observed even at 623 K, at which there are hardly any water-related ions remaining on the solid surface [25]. Fourth, studies by Wang *et al* [26] indicated that CE at a vacuum of  $10^{-6}$  torr was five times higher than that at one atmosphere pressure. There are hardly any water molecules adsorbed on solid surfaces at such a high vacuum in comparison to ambient cases. Finally, Liu *et al* [27] showed that a sustainable tunneling current had been produced using an unbiased, triboelectrically charged metal–insulator–semiconductor point contact system. All of these phenomena indicate that water ions are not mandatory for CE, and the CE has to be an electron-dominated transfer process. Therefore, owing to the vast selection of materials in the categories of metals, dielectrics, glasses, ceramics and semiconductors that exhibit a TE effect, there is hardly any convergence in scientific understanding about the nature of TE.

In this section, we systematically review the studies that have been carried out for exploring the nature of CE using KPFM and provide a unified picture for understanding CE in several interface configurations. By clearly distinguishing CE from TE, our conclusion is that electron transfer is the dominant mechanism for CE among solids, liquids, and gases. Electron transfer occurs only when the interatomic separation between the two atoms/molecules/materials is forced to a distance shorter than the normal bonding length, typically 0.15–0.2 nm, which is the result of rubbing one material against another by applying an external force to achieve a close contact. It is only at this short-range contact that electron transfer is possible. As a result, we can redefine CE to be a quantum mechanical electron transfer process that occurs for any material, in any state (solid, liquid, gas), in any application environment, and in a wide range of temperatures up to  $\sim 400$  °C. Such an effect is universal and is fundamentally unique in nature [28]. Previously, a comprehensive review about CE at solid–solid interfaces has been given by Wang and Wang [29]; our review here will focus on CE between semiconductors, liquids and other cases that have not been covered before.

A typical surface charge density related to CE is up to  $\sim 10^{-3}$  C m<sup>-2</sup>, which corresponds to  $\sim 1$  excess electron charge per 1600 nm<sup>2</sup> of surface area. The average distance between two adjacent charges is  $\sim 40$  nm. Thus, the probability of electron transfer is about one out of  $\sim 40\,000$  surface atoms. Although the probability appears rather small, this charge transfer is an important quantum mechanical process for many interface chemical, biochemical and catalysis processes that occur in our life at any place and any time.

### 2.1. CE at solid–solid interfaces

**2.1.1. Metal–dielectric.** In our daily life, rubbing a metal rod on a rock surface results in sparks, which is the result of TE and related air discharges in a metal–dielectric (M–D) case. This phenomenon at the nano-scale has been studied using KPFM by scanning a Pt tip on a SiO<sub>2</sub> surface [30]. Since the Fermi

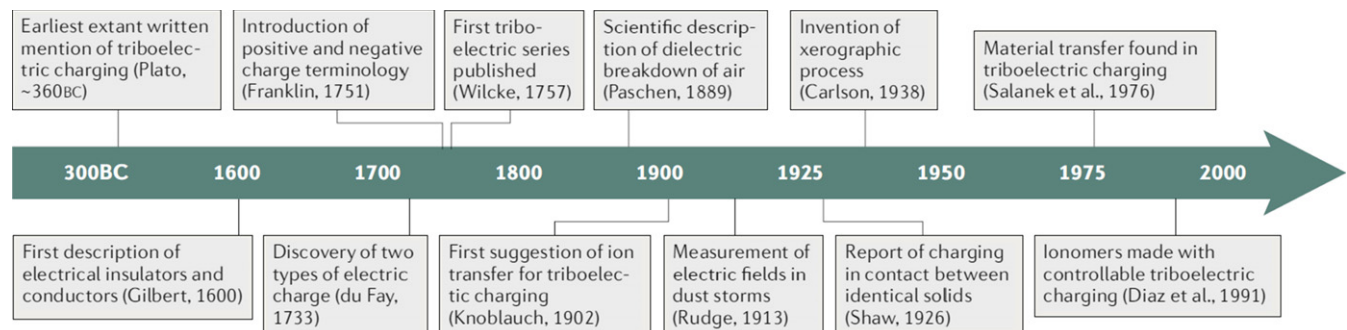


**Figure 2.** Major developments in the history of studying triboelectric charging through the year 2000. Reprinted by permission from Springer Nature Customer Service Centre GmbH: *Nature. Nat. Rev. Chem.* [2] © 2019.

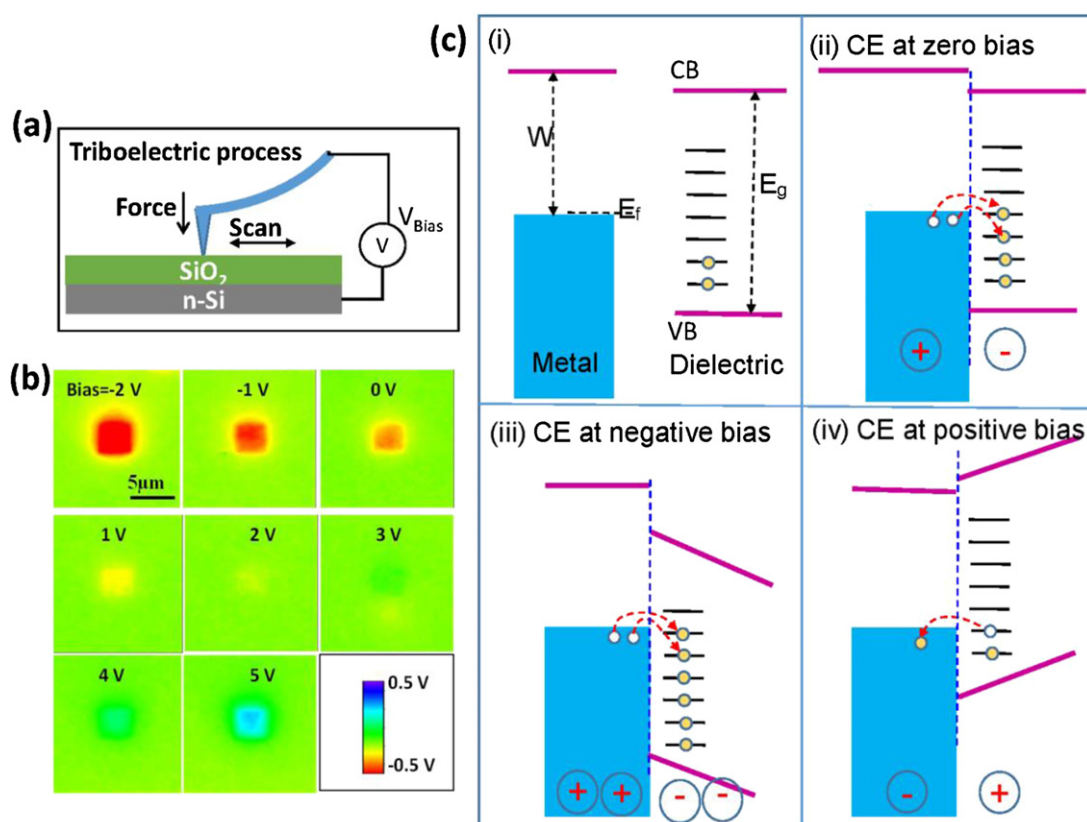


**Figure 3.** (a) Schematic of experimental setup of the AFM tip and the KPFM to map the surface potential distribution. (b) Surface potential distributions of the parylene film including the areas that were rubbed by the Pt-coated AFM tip at different bias from  $-2$  to  $5$  V. (c) Schematic energy band diagrams for the metal and dielectric materials in the situations of pre-contact (i), in contact with no bias (ii), and in equilibrium with negative (iii) and positive (iv) bias. Reprinted from [29], Copyright (2019), with permission from Elsevier.

level of the metal can be controlled by applying a bias voltage (figure 3(a)), the amount and sign of the charges to be delivered on the  $\text{SiO}_2$  surface can be manipulated and switched by the applied bias voltage (figure 3(b)) [31]. By tuning the applied bias on the metal tip from  $-5$  V to  $+5$  V, the charges delivered to the surface changed from negative to positive, and there was almost no charge exchange observed when the applied bias was set at  $3$  to  $4$  V. The data indicate that the nature of the transferred charges must be electrons. The mechanism of CE in M–D cases can be explained well using an energy band diagram, in which the metal is characterized by its Fermi level. The dielectric surface is characterized using its band diagram

composed of conduction band (CB) and valence band (VB), but the surface/defect states are assumed to present at the surface (figures 3(c-i)) [32]. If the edge of the VB of the dielectric is below the Fermi level ( $E_f$ ) of the metal, some of the surface states in the bandgap  $E_g$  with energy below  $E_f$  could be filled up by the electrons transferred from the metal into the dielectric, resulting in negative charges on the dielectric surface (figure 3(c-ii)) [33, 34]. If a negative bias is applied on the metal tip (figure 3(c-iii)), the surface states on the dielectric side tend to be pushed down to even lower energy levels in reference to the Fermi level of the metal, resulting in more electrons being transferred from metal to dielectric. If

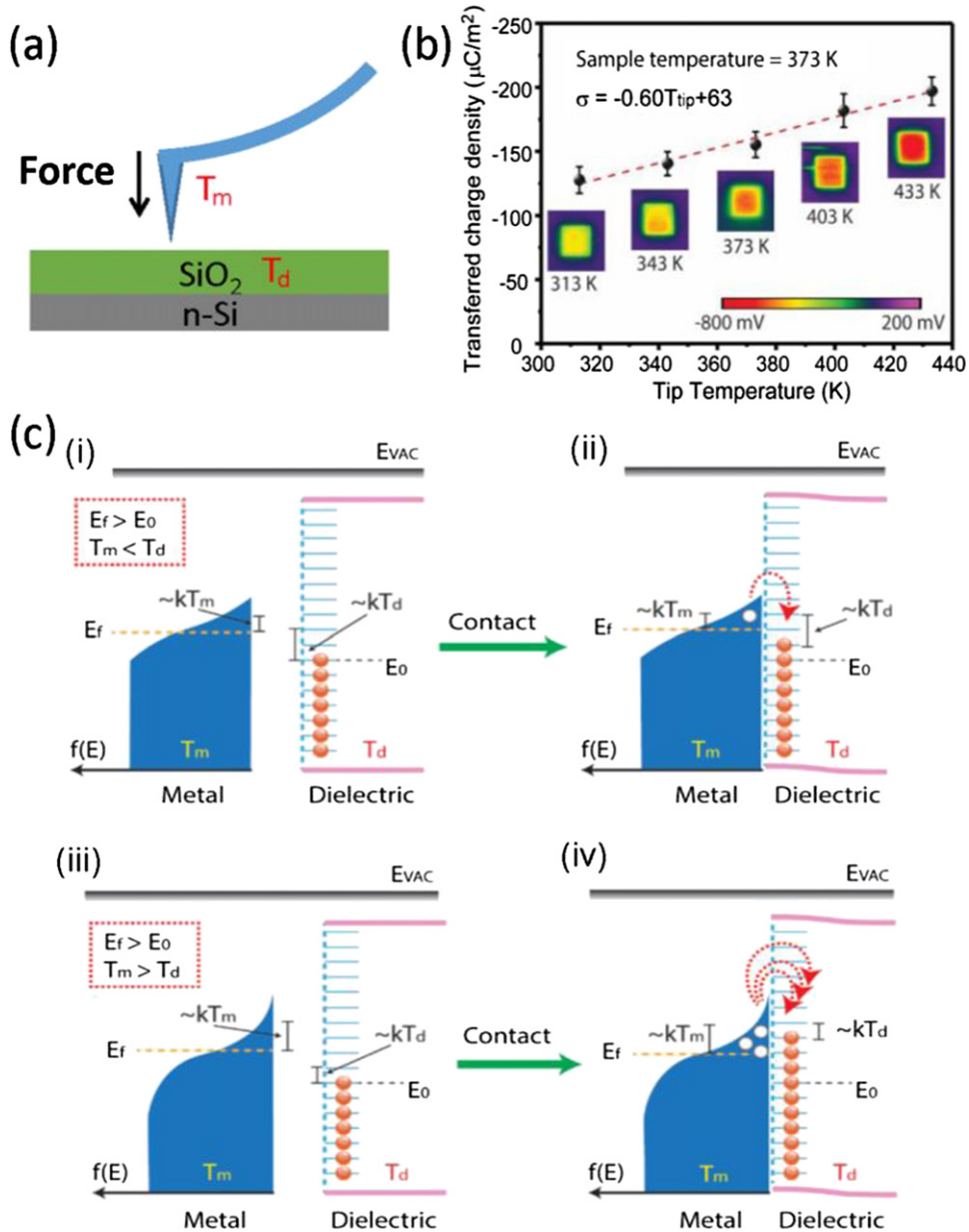


**Figure 4.** Proving the effect of temperature differences on CE between an Au-coated tip and the  $\text{SiO}_2$  sample by KPFM at nano-scale. (a) and (b) The sample temperature was set at 373 K, while the tip temperature varied from 313 K to 433 K. (c) The band structure model of the temperature difference induced charge transfer ( $E_f > E_0$ ). The band structure of the metal and surface states of the dielectric, when (i) the metal temperature is lower than the dielectric temperature, (iii) the metal temperature is higher than the dielectric temperature. Illustrations of contact-induced charge transfer between a metal and a dielectric when (ii) the metal temperature is lower than the dielectric temperature, and (iv) the metal temperature is higher than the dielectric temperature. [41] John Wiley & Sons. © 2019 WILEY-VCH Verlag GmbH & Co. KGaA, Weinheim.

a positive bias is applied (figure 3(c-iv)), the surface states in the dielectric side would be moved up to higher energy levels depending on the magnitude of the bias, and the electrons that occupy the surface states could be transferred to the metal, resulting in positive charges on the dielectric side. A recent AFM study also supports that CE in M–D cases is an electron transfer process [35]. KPFM has provided nano-scale charge transfer information for these cases [36–39]. The above discussion is valid if the electronic structure of the dielectric can be described by a band structure as we have presented; otherwise other models have to be introduced.

Recent advances have made it possible to independently control the temperatures of a scanning tip and the sample in KPFM (figure 4(a)) [40]. It is possible that the electrons would be thermally excited and transferred from the hotter material side to the cooler side. Hence, the charge transfers between the tip and the sample may be manipulated by setting the tip and sample at different temperatures. To verify this, the tip temperature was controlled at 373 K, while the  $\text{SiO}_2$  sample temperature was varied from 313 K to 403 K. As shown in figure 4(b), the transferred charge density increased linearly with raised tip temperature.

The observed result can be explained using an energy band diagram, as shown in figure 4(c). Considering the temperature effect, the distribution of electrons in the metal tip at different energies follows the Fermi–Dirac function:

$$f(E) = \frac{1}{e^{((E-E_f)/kT)} + 1}, \quad (1)$$

where  $f(E)$  denotes the probability of an electron in the energy level  $E$ , and  $E_f$  denotes the Fermi level of the metal. Above the Fermi level, there is a tail filled with electrons.

In the first case, we assume that the Fermi level ( $E_f$ ) of the metal is higher than the highest occupied surface state level ( $E_0$ ) of the dielectric, and the metal tip temperature ( $T_m$ ) is lower than the dielectric temperature ( $T_d$ ) ( $T_m < T_d$ ) (figure 4(c-i)), hence the energy increase of electrons in the metal ( $\sim kT_m$ ) will be lower than the increase of electron energy in the dielectric ( $\sim kT_d$ ). In this case, the electrons transfer from the metal to the dielectric in CE, as shown in figure 4(c-ii). If the metal temperature is increased while the dielectric temperature remains unchanged ( $T_m > T_d$ ), as shown in figure 4(c-iii), the increase of electron energy in the metal ( $\sim kT_m$ ) will be higher than the increase of electron energy in the dielectric ( $\sim kT_d$ ). This leads to more electrons hopping from the metal tip to the dielectric side (figure 4(c-iv)).

Electron transfer between metal and dielectrics is affected by the potential barrier at the interface. To explain the effect of the energy barrier in the charge transfer process from Al to polyimide (PI), films with functional groups were investigated with density functional theory (DFT) calculations and the measured output powers were compared with the efficiency of the charge transfer [42]. Figure 5(a) shows the energy band diagrams of three monomers, of which energy levels are aligned with respect to vacuum energy level, between LUMO and LUMO + 5. It is observed that the 6FDA-APS PI has significantly lower LUMO energy levels than those of the other polymers (6FDA-ODA PI and 6FDA-PDA PI). Figure 5(b) shows the electrostatic planar average potentials of three polymers, where the end-group of the monomer is located at 0.25 nm above the Al (111) surface. The energy barrier heights, which are based on the Fermi energy level of Al (111), of 6FDA-ODA PI, 6FDA-PDA PI, and 6FDA-APS PI are calculated to be 1.97, 1.75, and 1.10 eV, respectively. This implies that the negative charges are most easily transferred from electrode to 6FDA-APS PI among the polymers, which is supported by the output powers measured from experiments in terms of energy barriers and LUMO levels from DFT calculations, as shown in figure 1(c).

**2.1.2. Metal–semiconductor case—tribovoltaic effect.** The study of metal–semiconductor contact is interesting because of the convoluted property of semiconductor and interface CE. AFM studies by Liu *et al* [35] for a metal-MoS<sub>2</sub> system revealed that a DC current is generated by contacting a metal tip on the WS<sub>2</sub> surface. Lin *et al* [43] found a similar effect by sliding a metal electrode on the top of a semiconductor. By sliding a metal contact on the surface of a semiconductor wafer back and forth, a DC current output across an external load

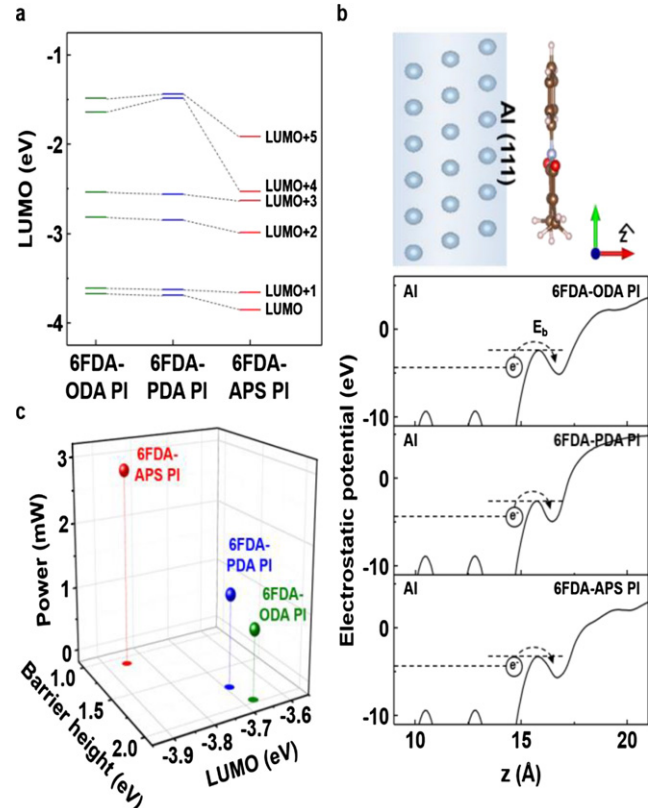


**Figure 5.** Effect of interface potential barrier on the electron transfer between metal and polymer. (a) Energy diagram of three monomers, of which energy levels are aligned with respect to vacuum energy level, between LUMO and LUMO + 5. (b) Electrostatic planar average potentials and the corresponding energy barrier heights for electron transfer from Al electrode to monomers. (c) The output powers of the PI-based TENGs with barrier height and LUMO level. [42] John Wiley & Sons. © 2019 WILEY-VCH Verlag GmbH & Co. KGaA, Weinheim.

was observed (figures 6(a)–(d)), which is distinctly different from the output of TENG fabricated using insulator dielectrics that usually gives an AC output. The output voltage and current correspond well to the position and velocity of the metal contact on the surface. There are two possible interpretations. First, once a metal piece slides on the surface of the semiconductor, new bonds would be formed at the interface area that is newly formed during sliding. It is known that the energy required to separate the charged surfaces is comparable to the fracture energies of materials, which reveals that the electrification is associated with the interactions in electron clouds [44]. The energy released by forming a bond is equivalent to an ‘energy quantum’ (so-called ‘bindington’) that could excite electron–hole pairs at the semiconductor side (figure 6(e), process I), and the electrons will be separated from the holes due to the presence of the Schottky barrier, possibly resulting in a DC current. This is similar to the result of photovoltaic effect except the energy is provided by the tribo-process rather than photons. This may be simply referred to as the *tribovoltaic effect* [29, 45, 46].

The second possibility is that the electron from the metal side can transit to the unoccupied surface states at the semicon-

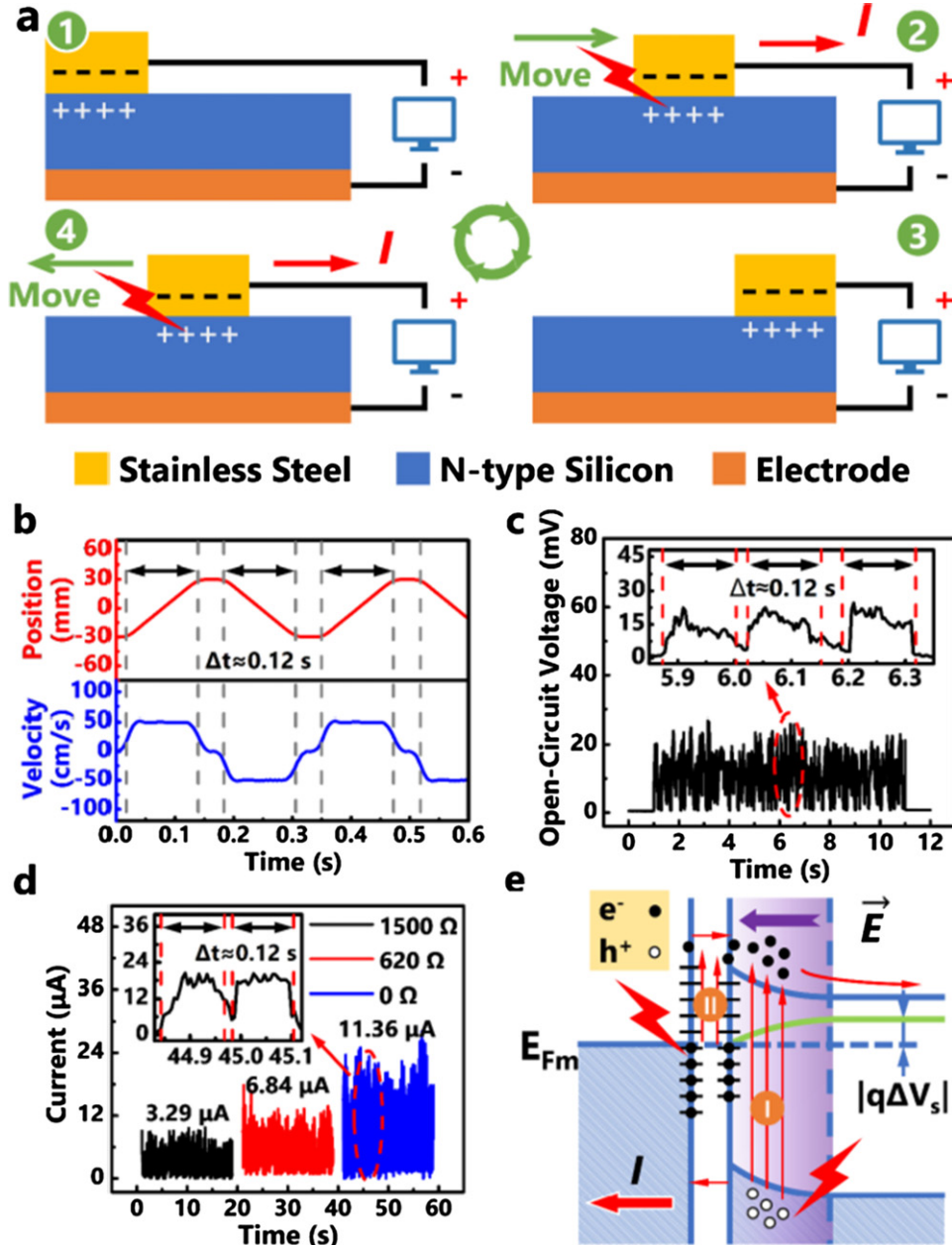


**Figure 6.** The electric output characteristics of the metal–semiconductor-based direct-current TENG. (a) The 3D schematic illustrations of the measurement setup and the external circuit. (b) The relative position and velocity of the metal slider and the silicon wafer as a function of time. (c) The oscilloscope of open-circuit (OC) voltage. Inset: partial magnified view of the voltage. There is continuous voltage output during a sliding period ( $\Delta t$ ). (d) The current output with different load resistances (1500, 620 and 0  $\Omega$ ). The above currents are calculated by the average of the selected 20 s current data. Inset: partial magnified view of the short-circuit (SC) current. (e) Energy band diagram of a metal–semiconductor junction for illustrating the tribovoltaic effect. [45] John Wiley & Sons. © 2020 WILEY-VCH Verlag GmbH & Co. KGaA, Weinheim.

ductor side, and the energy released could stimulate the tunneling/transition of electrons from the metal side to the semiconductor side (figure 6(e), process II). However, the energy exhibited by the electron may not be enough to excite the electron–hole pair at the semiconductor side.

**2.1.3. Semiconductor–semiconductor case.** Following the design of the TENG in contact-separation (CS) mode, a piece of p-type Si wafer is periodically contacting an n-type Si wafer (figure 7(a)), a non-symmetric AC current has been observed in the external circuit [47], with a large current

observed when the two pieces are separated and a smaller current is received when the two pieces are in contact with each other (figure 7(b)). It is noticed that the current generated for separating the two pieces is much larger than that when the two are contacted. There are three possible processes involved in the generation of current. First, as shown in figure 7(c), once two semiconductors are in contact (figure 7(c2)), holes and electrons diffuse across the interface into the counterpart to form an intrinsic electric field and the Fermi levels are aligned. The current generated in this process is an internal current, and

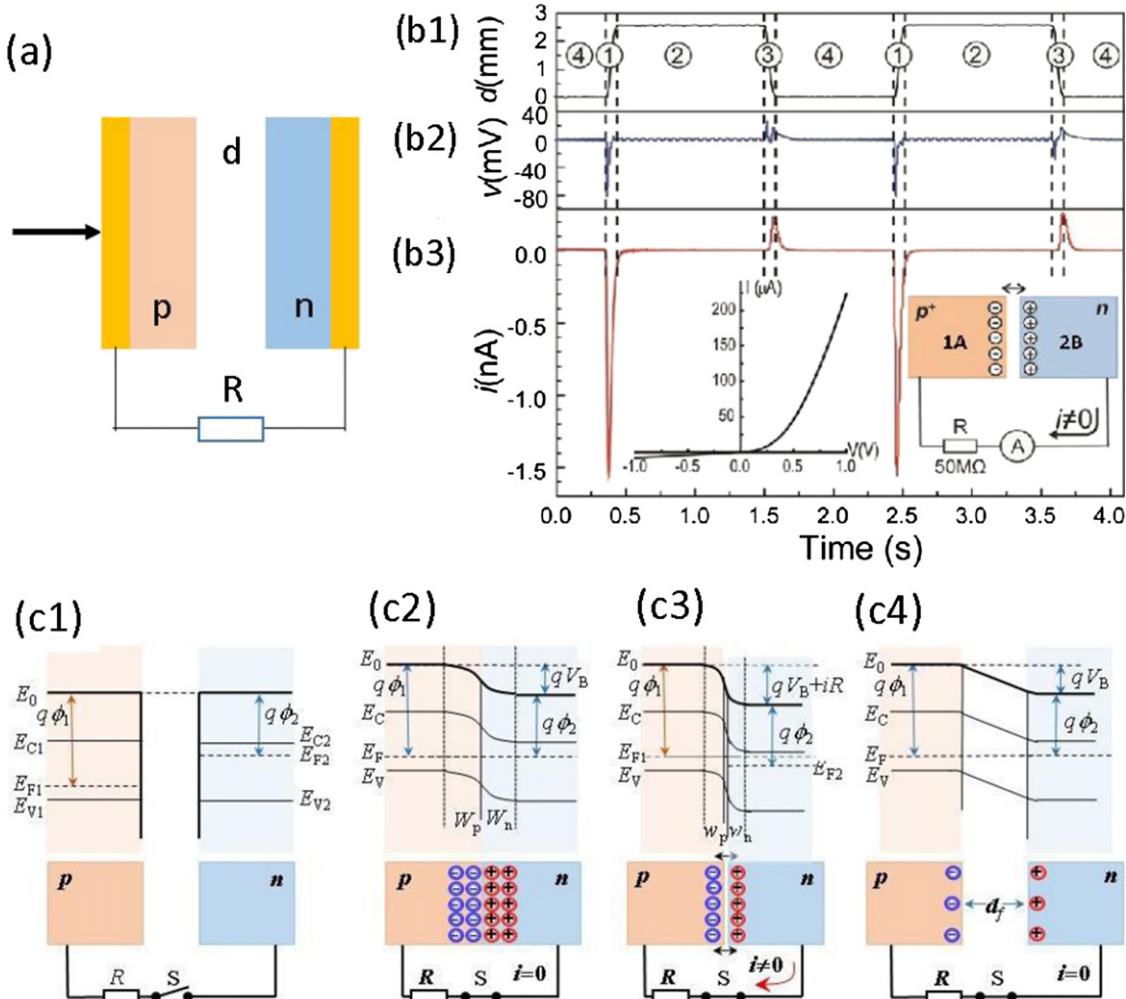


**Figure 7.** Output of a tribovoltaic cell fabricated using p-type and n-type semiconductors in the CS mode. (a) Schematic of the TENG. (b1) The gap width  $d$  between the two semiconductor wafers, (b2) the voltage dropped across the load  $R$  and (b3) the output current in the contacted stage ④, the separating stage ①, the separated stage ② and the approaching stage ③. inset (left): the current  $I$  as a function of the biased voltage  $V$  when the two electrodes are in contact. inset (right): the schematic measurement circuit. (c) The energy band diagrams for a pair of n- and p-type semiconductors and the corresponding space charge distribution at (c1) the disconnected stage, (c2) the contacted stage, (c3) the separating stage and (c4) the separated stage. Reprinted from [47], Copyright (2018), with permission from Elsevier.

no current is expected to be observed in the external circuit. Once the two are being separated (figure 7(c3)), the holes diffused to the n-side would be conducted through the external load into the p-side, resulting in an observed current. Such a process stops if the two pieces are separated wide enough apart (figure 7(c4)). The DC current is expected to flow from the n-side to the p-side when the n- and p-semiconductors are separated owing to carrier redistribution. Second, considering the CE between the n- and p-side, surface charges are inevitably formed at the two surfaces, respectively, and a contact and separation of the two pieces would result in an AC current in the external load. This is the general mechanism of TENG. Finally, a contact of the two semiconductors would create atomic bonds at the interface, which would release energy. Such energy can generate electro-hole pairs via the tribovoltaic effect [29, 47], which is a DC signal flowing from the p-side to the n-side when the n and p semiconductors are contacted. The experimentally observed current is a sum of the three processes. It is

likely that the current signal in figure 7(b3) is non-symmetric in magnitude.

Sliding an n-type semiconductor on a p-type semiconductor as for the sliding mode TENG, a DC current has been received to flow from the p-side to the n-side (figure 8(b)). The observed current strongly depends on the nature of the semiconductor and its conductivity. This effect can be explained as a result of tribovoltaic effect (see section 2.1.2). Contacting an n-type on a p-type semiconductor, an internal electric field would be generated and an equilibrium is reached (figure 8(c2)). Once the n-type slides on the p-type, new atomic bonds would be formed at the newly formed interface area, which would release energy owing to the formation of new bonds. Such energy would generate electron–hole pairs at the interface region, the separation of which by the pn junction would generate a DC current (figure 8(c3)). In this process, the current contributed by CE is negligible because the total contact area between the two

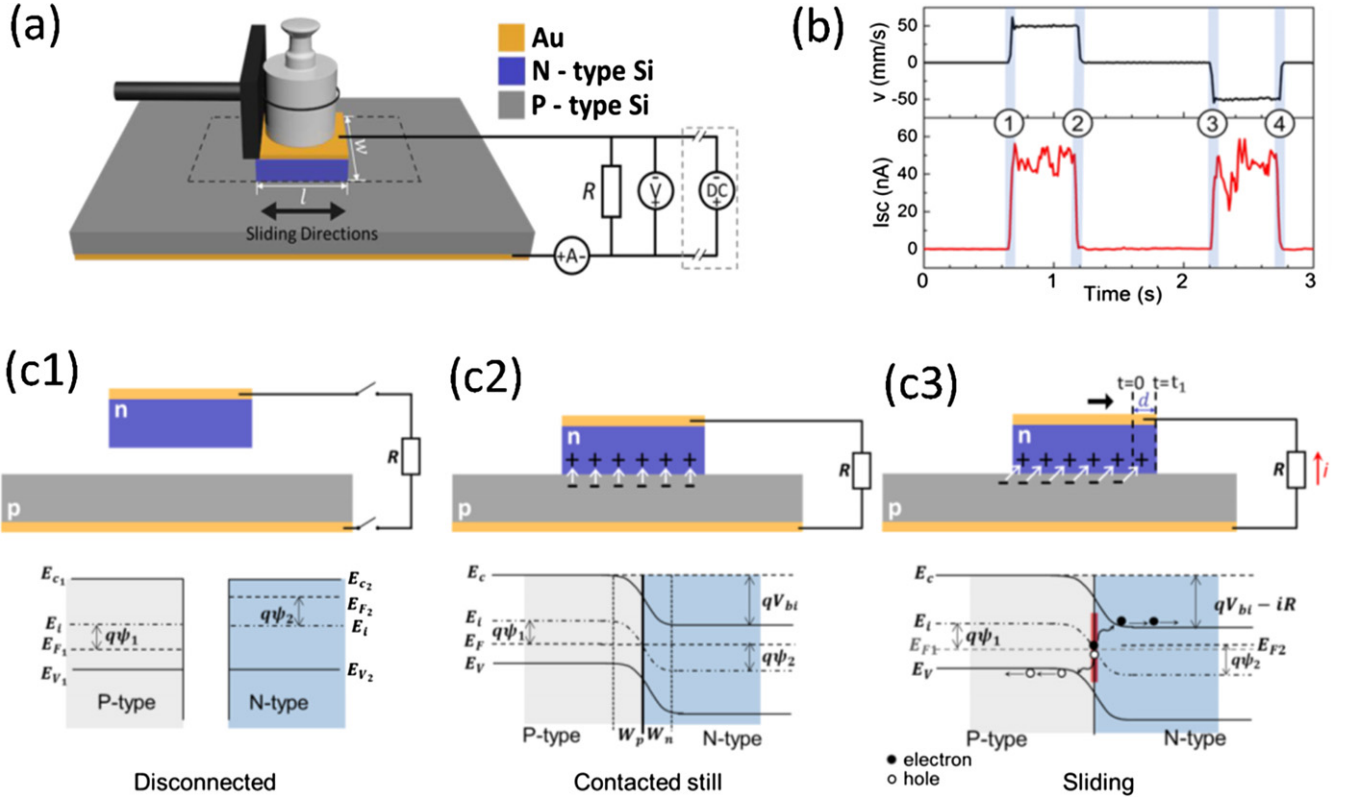


**Figure 8.** Output of a tribovoltaic cell fabricated using a p-type and n-type semiconductors in the sliding mode. (a) A 3D schematic for the experiment setup and the external circuit. (b) The displacement (upper) of the top electrode with respect to the other electrode and  $I_{SC}$  (lower) as a function of time for four sliding stages in one sliding cycle. The schematics and energy band diagrams for a triboelectric cell with an n-type semiconductor as the top electrode and a p-type semiconductor as the bottom electrode. (c) The mechanism of the tribovoltaic cell: (c1) the disconnected stage, (c2) the contacted still stage, (c3) the top is being laterally slid on the bottom electrode. Reprinted from [49], Copyright (2019), with permission from Elsevier.

pieces remains the same. The current contributed by the carrier redistribution is confined inside the pn junction, and thus, no output current would be observed by this process. The existence of the tribovoltaic effect has been further verified by contacting a diamond AFM tip on a silicon surface [48].

#### 2.1.4. Dielectric–dielectric case.

**2.1.4.1. The surface state model.** CE is a universal phenomenon that occurs for all materials, which is the challenge behind developing a unified picture to explain CE across the diverse spectrum of materials. For materials whose electronic structures can be represented by energy bands, CE between two materials can be easily presented as in figure 9 by using the surface state model [25, 50, 51]. This is reasonable because the presence of a surface means an interruption of the crystal periodicity, e.g. an abrupt change of the periodical crystal lattice, leading to the formation of energy states within the bandgap. The presence of defects (surface defect structures) could result in the occupation of surface states by electrons. Owing to the different valance band and CB structures of each material, the occupied surface states in material A could have higher energy than that of the unoccupied surface states of material B (figure 9(a)). Once the two materials physically contact, some of the electrons could transfer from material A's surface to the surface of material B due to an energy drive,

leading to CE. Such electrons will not transfer back to material A even after the two materials are separated if no thermal or phonon excitation is applied, resulting in net positive electrostatic charges on material A and negative electrostatic charges on material B (figure 9(b)). Such charges are surface state bound charges and cannot freely flow in general cases if the conductivity of the materials is rather low; thus, they are expected to remain on surfaces permanently. However, in the presence of thermal energy fluctuations and raised temperatures, these bound electrons can be released from surface states according to the thermionic emission model. The surface state model is the mostly easy and acceptable for understanding the charge transfer between two solids, provided each of the solids can be described by the energy band diagram.

**2.1.4.2. The overlapped electron cloud model.** The surface state model is valid if the electronic structure of the dielectric can be represented by a band diagram with the presence of surface and defect states. As for general materials such as polymers and rubber materials, their electronic structures are represented by molecular orbitals and chain alignment rather than the energy band diagram. Furthermore, for materials that may not have a well characterized molecular structure or in the presence of composite phases, as in natural materials such as wool, wood, animal fur, and human hair, there is no simple electronic structure model that can represent these materials.

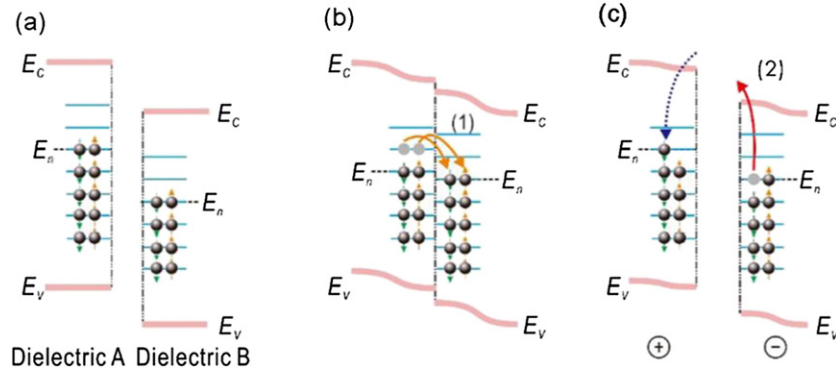


**Figure 9.** Charge transfer (a) before contact, (b) in contact, and (c) after contact between two different insulator dielectrics for a case where  $E_n$  of the former is higher than that of the latter and the band structure model holds.

We do know that all of these existing materials exhibit CE, and therefore a general model is needed for explaining CE at the atomic and molecular levels.

We start from experimental observations based on KPFM study. The first question is: how close must the two atoms be before CE occurs? This question has been answered by KPFM study [52]. By correlating the phase and amplitude measured for the AFM tip at resonance with the measured surface potential difference ( $\Delta V$ ), the interaction force between the tip and the surface can be probed. When the tip experiences a net attractive force from the surface, it is in the attractive regime, and there is an increase of the phase shift ( $\Delta\varphi > 0$ ). In contrast, if the tip experiences a net repulsive interaction force from the surface, it will be in the repulsive force regime, and there will be a decrease from the original phase shift ( $\Delta\varphi < 0$ ). Therefore, the sign of  $\Delta\varphi$  could be regarded as the symbol of the net tip–sample interaction force for each vibration cycle. The result shows that the distance between the tip and the sample for electron transfer to occur should be smaller than the interatomic distance at equilibrium, where the long range attractive force is equal to the short-range repulsive force.

The repulsive and attraction interactions between atoms can be easily understood from the interatomic interaction potential [25]. For two atoms that form a bond, which means some sort of overlap in electron clouds or wave function, an equilibrium distance  $a$  is established, which is called the bond length or interatomic distance. If the interatomic distance  $x$  is larger than  $a$ , the two atoms tend to attract with each other (figure 10(a1)), in which case the overlap between the electron clouds of the two atoms is negligible, and thus no electron transfer is possible. If the interatomic distance  $x$  is shorter than  $a$ , the two atoms tend to repel each other owing to the increased overlap of electron clouds (figure 10(b1)). It is in such a range that electron transfer occurs.

One of the key factors in CE is an external force that has to be applied in order for the two surfaces to be contacted. The role played by such an externally applied force is to create local high pressure at certain contacting points even at the atomic and nano-scales, where the interatomic distance  $x$  is forced to be shorter than the bonding length between the local contacting points, resulting in local repulsive force. This is why CE is indispensable from friction in practice.

The experimental results indicate that the distance between the AFM tip and the surface has to be shorter than the atomic bonding length in order for the CE to occur. In the repulsive region, the increased overlap in local electron clouds results in electron transition from one material to the other. Therefore, we can propose an atomic-scale charge transfer mechanism for CE [53]. Figure 10(a2) shows a case in which, prior to the atomic-scale contact of the two materials, their respective electron clouds remain separated without overlap. This is the attractive force region. The potential well bounds the electrons tightly in specific orbitals and stops them from freely escaping, which is the case for non-conducting materials. When the two atoms belonging to two materials, respectively, get close and contact with each other, the electron clouds overlap between the two atoms to form a bond. The bonding lengths are shortened even more if an external compression force is applied. In this case, the initial single potential wells become an asymmetric double-well potential, and the energy barrier between the two is lowered as a result of strong electron cloud overlap. Then electrons can then transfer from one atom to the other, resulting in CE. The role played by mechanical contact of the two materials is to shorten the distance between the atoms and cause a strong overlap of their electron clouds in the repulsive region, at least in the area at which the atomic-scale contact occurs, despite the samples being larger. The process presented in figure 10(b2) is referred to as the Wang transition.

From the schematic shown in figure 10, it appears that CE may occur for all atoms/matters. In reality, it is important to note that only a very small fraction of surface areas of the two materials will reach atomic scale contact considering the atomic roughness of the surfaces. This also explains why more charges are transferred if one material is rubbed harder against the other owing to the strongly overlapped electron clouds under the applied pressure. On the other hand, applied force can even cause local fractures and plastic deformation, which is why CE is always convoluted with the friction process, possibly with the generation of debris. After being separated, the transferred electrons remain as static charges on the surfaces.

From the electron transfer model presented in figure 10(b2) for the interatomic transition, several photon emission processes are proposed. Energy can be released by two processes. One is the energy difference between the electronic states

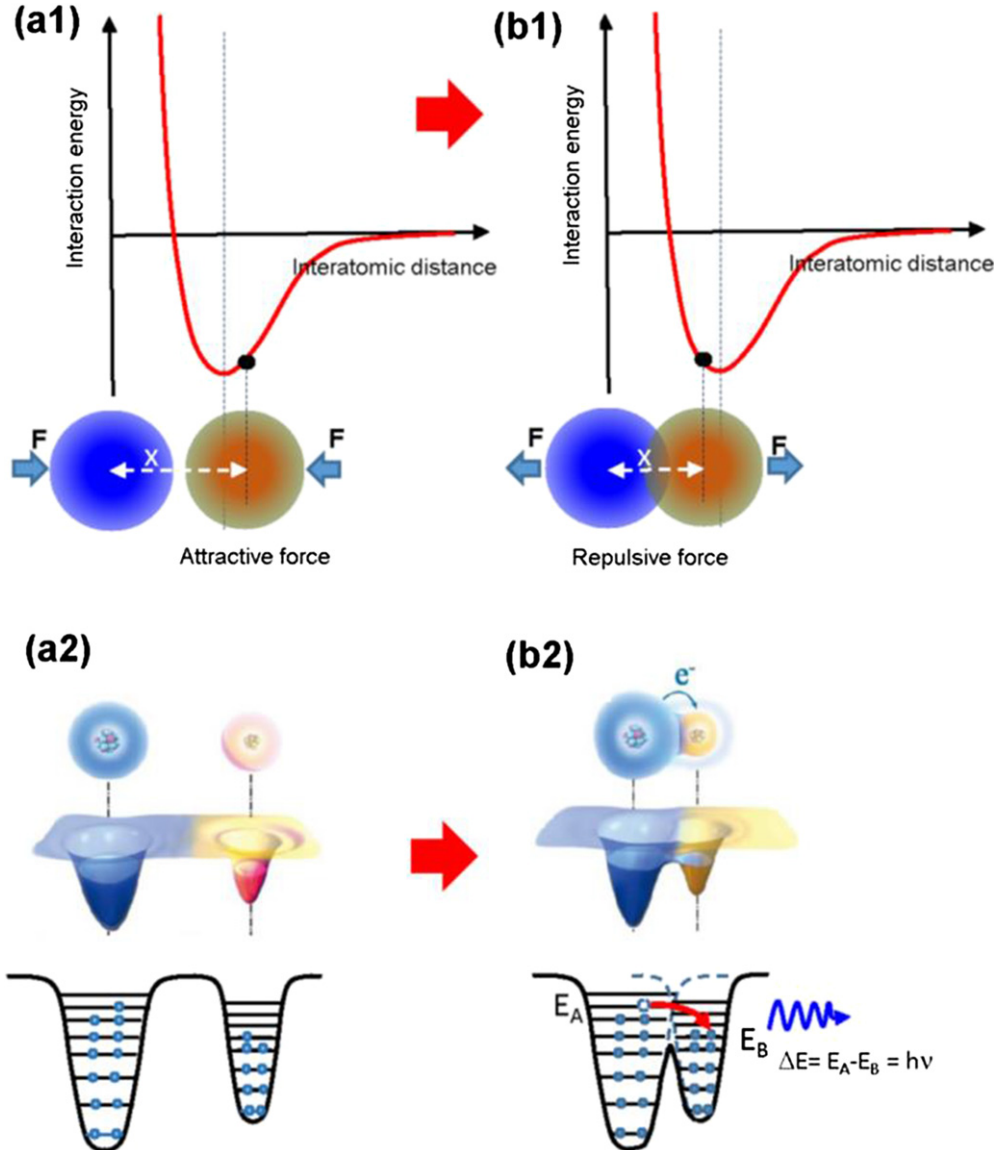


**Figure 10.** The electron cloud/wave-function overlap model for CE. Interatomic interaction potential between two atoms and the force between the two when they are (a1) with little electron cloud/wave-function overlap, (b1) with strong electron cloud/wave-function overlap in the repulsive region. (a2) and (b2) are the corresponding (3D and 2D) atomic potential energy model and the electronic states of two atoms belonging to two materials A and B, respectively, when they are before contact and in contact, respectively, showing electron transfer from one atom to the other after being forced to have electron cloud overlap. Detailed illustration to show that the increased electron cloud overlap results in a lower potential barrier between the two atoms, leading to interatomic electron transition and possible photon emission, which is indicated in (b2). The transition shown in (b2) is called the Wang transition.

between the two atoms as indicated in figure 10(b2), which could be in the form of photon emission, plasmon excitation and/or phonon excitation [29]. Photon emission, if possible, can be used for studying the transition from the surface states of dielectric A to the surface states of dielectric B. The emitted photon should have energy in tens of eV, possibly resulting in UV, visible light, microwave and even THz wave emission when two materials contact. The above proposed processes, if potentially observable as light emission, could give birth to a new interface optical spectroscopy for studying electronic transitions at interfaces. These results remain to be verified experimentally. Recently, we have observed the first atomic featured photon emission spectra during CE between two solid

materials. The photon emissions are the evidence that electron transfer takes place at the interface from one atom in one material to another atom in the other material during CE. This process is CE-induced interface photon emission spectroscopy [54]. It naturally paves a way to a spectroscopy corresponding to the CE at an interface, which might have a fundamental impact on understanding the interaction among solids, liquids and gases.

The energy of the CE-produced electron is not expected to exceed tens to hundreds of eV. By bombarding a metal plate using electrons emitted during peeling a piece of tape in vacuum, continuous x-rays with energies centered around 15 keV have been observed [55]. Considering the high electric field generated by CE charges, in the order of  $10^5$ – $10^6$  V m<sup>-1</sup>, it

is possible to generate a high voltage. Freely released electrons accelerated by such high voltages could result in strong x-ray radiation [56]. On the other hand, air can be broken down by such a high electric field, resulting in discharge of air molecules. Such emission needs to be excluded in practical measurement.

The last process for energy release is the energy from forming a bond. It is generally known that forming a bond places the two atoms into a lower energy state, resulting in energy release. This released ‘energy quantum’ can generate electron–hole pairs at the semiconductor surface/interface, e.g. tribovoltaic effect, which is what is presented in sections 2.1.2 and 2.1.3.

The model proposed in figure 10 is also supported by quantum mechanical calculations. A quantum-mechanical treatment of CE involving photon emission/absorption (figure 11(a)) was provided by Willatzen and Wang [57]. To simplify the analysis and emphasize the general principles of photon-assisted CE, consider two interacting atomic systems *A* and *B* with a total of *N* electrons that can jump between atoms of the two systems. We denote the number of atoms in systems *A* and *B*, occupied by aforementioned electrons, *N<sub>B</sub>* and *N<sub>A</sub>*, such that *N* = *N<sub>B</sub>* + *N<sub>A</sub>* at any time. The Einstein rate equations for two coupled atomic systems *A* and *B* are

$$\frac{dN_B}{dt} = -N_B A_{BA} - N_B B_{BA}\rho(\omega) + N_A B_{AB}\rho(\omega), \quad (2)$$

$$\frac{dN_A}{dt} = N_B A_{BA} + N_B B_{BA}\rho(\omega) - N_A B_{AB}\rho(\omega), \quad (3)$$

where the rate of spontaneous emission is given by

$$A_{BA} = \frac{\omega^3}{3\pi c^3 \varepsilon_0 \hbar} |\langle |f| \mathbf{e} \mathbf{r} |i\rangle|^2 = \frac{e^2 \omega}{3\pi m_0^2 c^3 \varepsilon_0 \hbar} |\langle |f| \mathbf{p} |i\rangle|^2. \quad (4)$$

Use of the Einstein rate equations for two-level atomic systems and Planck’s blackbody radiation formula in thermal equilibrium provides a relationship between the spontaneous emission rate and the stimulated emission and absorption rates assigned *B<sub>AB</sub>* and *B<sub>BA</sub>*, respectively,

$$B_{AB} = B_{BA}, \quad (5)$$

$$B_{BA} = \frac{\pi^2 c^3}{\omega^3 \hbar} A_{BA}. \quad (6)$$

Considering the following initial conditions *N<sub>B</sub>*(*t* = 0) = *N*, *N<sub>A</sub>*(*t* = 0) = 0, assuming electrons only occupy ground states of atomic systems *A* and *B* and *E<sub>A</sub>* − *E<sub>B</sub>* =  $\hbar\omega$  > 0, we may use the following simple expression of the dipole matrix elements:

$$\begin{aligned} & \langle \psi_{100}^B | \mathbf{p} | \psi_{100}^A \rangle \\ &= \frac{1}{\pi} \frac{i\hbar Z_A}{\alpha_0^4} (Z_A Z_B)^{\frac{3}{2}} \\ & \times \int d^3 \mathbf{r} \exp \left[ -Z_A \sqrt{\left( \frac{x}{a_0} \right)^2 + \left( \frac{y}{a_0} \right)^2 + \left( \frac{z}{a_0} \right)^2} \right] \end{aligned}$$

$$\begin{aligned} & \times \left( \frac{\left( \frac{x}{a_0} \right)}{\sqrt{\left( \frac{x}{a_0} \right)^2 + \left( \frac{y}{a_0} \right)^2 + \left( \frac{z}{a_0} \right)^2}} \right) \\ & \times \exp \left[ -Z_B \sqrt{\left( \frac{x - x_0}{a_0} \right)^2 + \left( \frac{y}{a_0} \right)^2 + \left( \frac{z}{a_0} \right)^2} \right], \end{aligned} \quad (7)$$

where *a<sub>0</sub>* = 0.053 nm is the Bohr radius. As shown in figure 11(b), setting atomic numbers for atomic systems *A* and *B* as equal, i.e. *Z<sub>A</sub>* = *Z<sub>B</sub>*, the relaxation rate dynamics of *N<sub>B</sub>* depend strongly on the fixed-in-time distance *x<sub>0</sub>* between the two atom systems. When atoms are separated by a few Bohr radii, CE is most efficient. This is a consequence of two properties: (1) momentum matrix elements between ground states having the same parity vanish identically, and (2) electron wave functions must overlap so as to have a nonzero matrix element. Requirement (1) ensures that the momentum matrix elements vanish in the case of complete overlap of *A* and *B* wave functions. This spatial behavior of maximum CE efficiency for atomic systems separated by a few Bohr radii agrees well with experimental observations in solids (metal, semiconductors, and dielectrics) supporting the electron cloud overlapping model. CE of solids using a tight-binding atomistic model has been presented by Willatzen and Wang [58] and Willatzen *et al* [59]. The density function theoretical calculations of Shen *et al* [60] for Al<sub>2</sub>O<sub>3</sub> and SiO<sub>2</sub> also support the electron exchange at interfaces if the distance between the two is in the repulsive region (figure 11(c)). Electron transfer occurs such that the Al<sub>2</sub>O<sub>3</sub> surface has net positive charges and the SiO<sub>2</sub> surface has net negative charges. The magnitude of electron transfers decreases to zero as the separation increases. It is important to note that the theoretically calculated charge density is orders of magnitude higher than that observed experimentally, which is due to the ignorance of electrostatic breakdown.

### 2.1.5. Contacts between two chemically identical materials.

It is generally known that physical contact of two dissimilar materials produces electrostatic charges, which is easy to understand when considering the differences in chemical potential and electronic structure. However, experiments have shown that contact between two chemically identical insulators (e.g. two pieces of the same material) also produces static charges [61]. In particulate materials, such as sand, smaller particles tend to be negatively charged and larger particles of the same material tend to be positively charged [62, 63].

In order to understand the underlying mechanism, we have carried out detailed studies of the CE of two pieces of chemically identical materials that possess different curvatures, such as polytetrafluoro-ethylene (PTFE), Kapton, polyester, and nylon [64]. By rationally designing materials with different surface curvatures, our results indicate that CE of two pieces of chemically identical materials results in concave surfaces

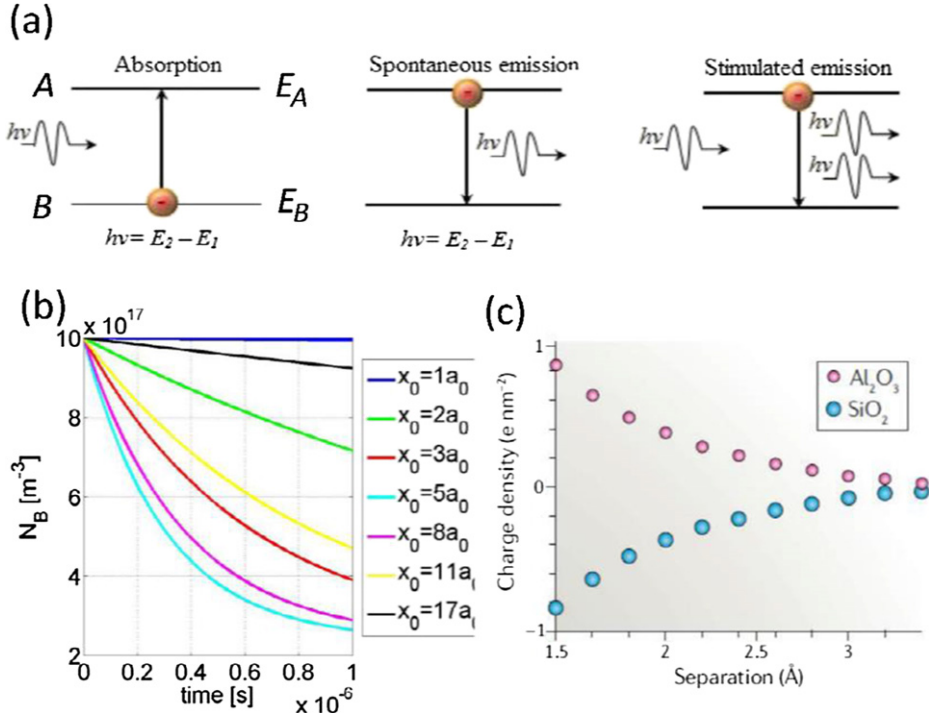


**Figure 11.** (a) Absorption, stimulated emission and stimulated absorption in atomic systems. (b) Electron dynamics and CE in a system of two atomic systems  $A$  and  $B$ .  $a_0$  is the Bohr radius: 0.053 nm. Reproduced from [58]. CC BY 4.0. (c) Charge transfer between  $\text{Al}_2\text{O}_3$  and  $\text{SiO}_2$  surfaces as a function of their separation calculated using DFT. Reprinted from [60], Copyright (2016), with permission from Elsevier.

being positively charged, and convex surfaces being negatively charged (figures 12(a)–(c)). Owing to the fact that surfaces with different curvatures would have different surface energies, possibly due to the stretched or compressed surface molecules or surface tension, the energies for specific surface states of the materials would be shifted considering the effects from surface energy (figure 12(d)). As a result, an electron can transfer from one material surface to another chemically identical surface with shifted surface states once they are physically in contact (figure 12(e)). Furthermore, this means that the presence of a curved surface ‘breaks’ the symmetry of the two sides, thus shifting the energy levels of surface states, resulting in electron transition, which is supported by theoretical study [65]. Considering a variation on surface morphology at the nano-level and a rise of local temperature during probe scanning, mosaic surface charge distribution has been observed on surfaces [66]. Recently, the flexoelectric effect has been proposed as the driving force for the transport of electrons across an interface [67]. Considering the magnitude of the electric field provided by the flexoelectric effect, this suggestion may only valid for the CE of chemically identical materials.

## 2.2. CE at liquid–solid interfaces

Interface between a liquid and a solid is fundamentally important for catalysis, surface chemical reaction, electrochemistry, chemical engineering and cellular-level biology, because charge transfer at the interface dictates many chemical and biological processes. As for the case of liquid–solid CE, it is usually assumed to be ion transfer without concrete studies, simply because ions are often present in solution, such

as  $\text{H}^+$  and  $\text{OH}^-$  in water. In this section, we will examine the charge transfer process and the nature of the charges at the liquid–solid interface. A newly revised model is proposed regarding the formation of an electric double layer (EDL).

**2.2.1. Liquid–dielectric case.** Using some of the conventional dielectric materials, such as  $\text{SiO}_2$ ,  $\text{Al}_2\text{O}_3$ ,  $\text{MgO}$ ,  $\text{Ta}_2\text{O}_5$ ,  $\text{HfO}_2$ ,  $\text{AlN}$  and  $\text{Si}_3\text{N}_4$ , we studied their charge transfer with a liquid droplet, such as DI water,  $\text{NaCl}$ ,  $\text{HCl}$  and  $\text{NaOH}$  solutions [68]. By dropping a liquid droplet on a virgin surface that has no electrostatic charges and waiting for its complete vaporization, the surface charge densities on the ceramic surfaces were measured by using KPFM at different substrate temperatures. We assume that both electron and ion transfers occur in a liquid–solid interaction. When the solid is heated by a sample heater, the electrons will be thermally excited and emitted from the solid surface (see section 2.4.1), as shown in figure 13(a), while the  $\text{O}^-$  ions may remain on the surface, since they formed covalent bonds with the Si atoms on the  $\text{SiO}_2$  surface and are hardly removed by the applied moderate temperature.

In the experiments, the CE between the  $\text{SiO}_2$  and the DI water was first performed, and figure 13(b) gives the results about the decay of CE charges on the  $\text{SiO}_2$  surfaces at different temperatures. The surface charge density on  $\text{SiO}_2$  remains almost unchanged at 313 K and slight decay of the surface charge density is observed at 343 K. As the sample temperature continues to rise, the decay rate of the surface charges increases. However, it appears that the charge density reaches a steady value after some time (about  $-180 \mu\text{C m}^{-2}$ ), which cannot be removed even when the temperature rises up to 434 K

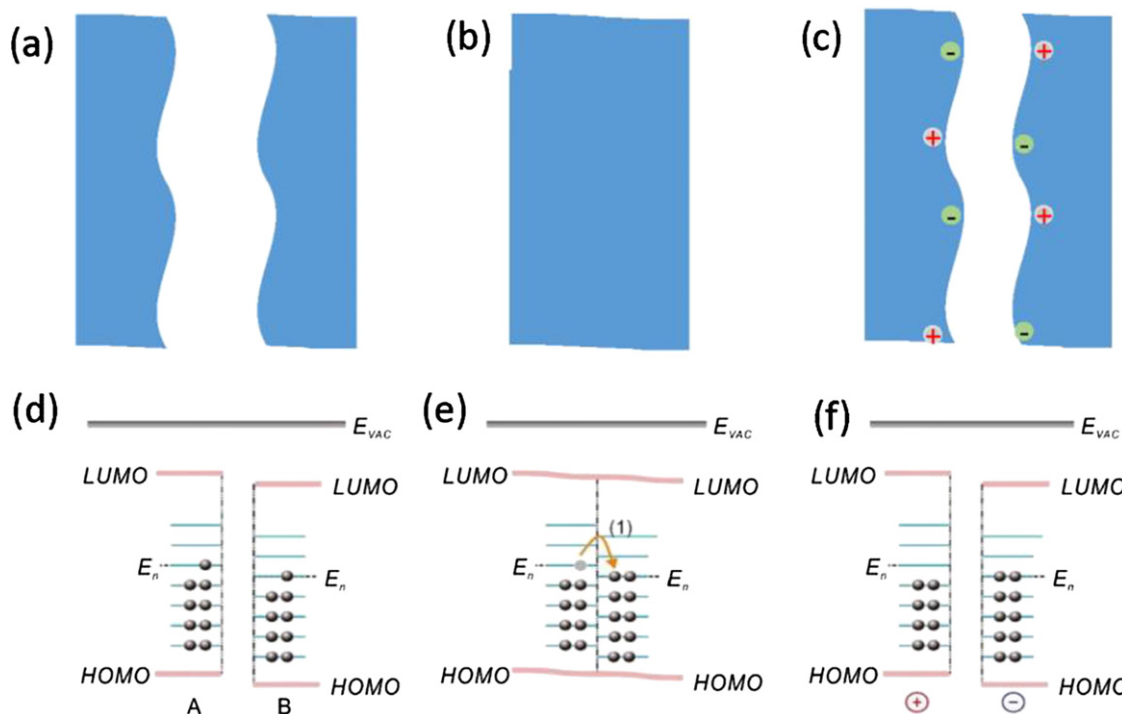


**Figure 12.** Mechanism of CE between identical polymer materials of different surface curvatures. (a)–(c) Charge transfer before contact, in contact, and after contact between two identical material surfaces *A* and *B* but with different surface curvatures, and (d)–(f) corresponding explanation of the surface charge transfer by the surface state model. LUMO, lowest unoccupied molecular orbital;  $E_n$ , neutral level of surface states; HOMO, highest occupied molecular orbital. Reprinted with permission from [64]. Copyright (2019) American Chemical Society.

and 473 K. For the removed charges, their decay behaviors are consistent with the thermionic emission theory, in which the electrons are considered to obtain more energy, and the electron density decays faster at higher temperatures.

In each cycle of the measurement, the  $\text{SiO}_2$  sample is contacted with a DI water droplet first, and then the sample is heated to 513 K and maintained at this temperature for 10 min to remove the electrons on the surface via thermionic emission. In the first cycle, the  $\text{SiO}_2$  is negatively charged when it is contacted with the DI water, and the density of the remaining charges is  $-180 \mu\text{C m}^{-2}$  as expected. Surprisingly, in the second cycle of the experiment, it is found that the density of the remaining charges increases to  $-300 \mu\text{C m}^{-2}$ , and it continuously increases with the number of the cycles until it reaches saturation. The remaining charges on the surface after heating to 513 K should be ions, such as  $\text{O}^-$  ions, instead of electrons. It appears that the total number of density of surface charges is fixed, and they are either occupied by electrons or ions depending on their competition. The heating removes electrons and opens up some ‘seats’ so that they can be partially occupied by ions (figure 13(d)). Since only electrons can be emitted from the surface by heating, the ‘vacant sites’ occupied by electrons will eventually be taken over by ions. This is probably the reason that only ions, if not exclusively, remain on the surface after multiple cycles of repeated heating and liquid contacts. Considering the leakage of electrons even at room temperature, the surface could be eventually occupied by ion adsorptions, which can be physical adsorptions and/or chemical adsorptions. On the other hand, if the leakage is rather

small at room temperature, then a certain portion of the surface charges are electrons if no heating is applied.

Based on the above analysis, we found a way of distinguishing electron transfer from ion transfer in the CE by performing the thermionic emission experiments (see section 2.4.1). The results indicate that there are both electron and ion transfers in the CE between  $\text{SiO}_2$  and DI water. If one considers the single contact between the two, the density of transferred electrons is measured to be  $-630 \mu\text{C m}^{-2}$  and the density of transferred ions is about  $-180 \mu\text{C m}^{-2}$  on the  $\text{SiO}_2$  surface. It means that the electron transfers, which account for 77% of the total charges, are dominant in the CE between  $\text{SiO}_2$  and DI water for the very first contact. For cases where the temperature is relatively low or even at room temperature, the chance for electron leakage is rather small, so that both electrons and ions are at the liquid–solid interface. Considering the large differences between the size, and mobility/diffusion/conductivity of electrons and ions, the dynamic characteristics of the interface will be strongly affected if there are electrons present. This is why the revision of the electric double layer in the next section has fundamental importance for chemistry, electrochemistry and even biology.

By changing the materials to be contacted with DI water, figure 14 shows the KPFM measured charge densities on the surfaces of  $\text{MgO}$ ,  $\text{Si}_3\text{N}_4$ ,  $\text{Ta}_2\text{O}_5$ ,  $\text{HfO}_2$ ,  $\text{Al}_2\text{O}_3$  and  $\text{AlN}$  at 433 K that were only contacted with DI water for the first time. The densities of ions and electrons on surfaces can be derived from the measured data. For  $\text{MgO}$ , the surface receives electrons from liquid, and also adsorbs  $\text{H}^+$  ions on the surface,

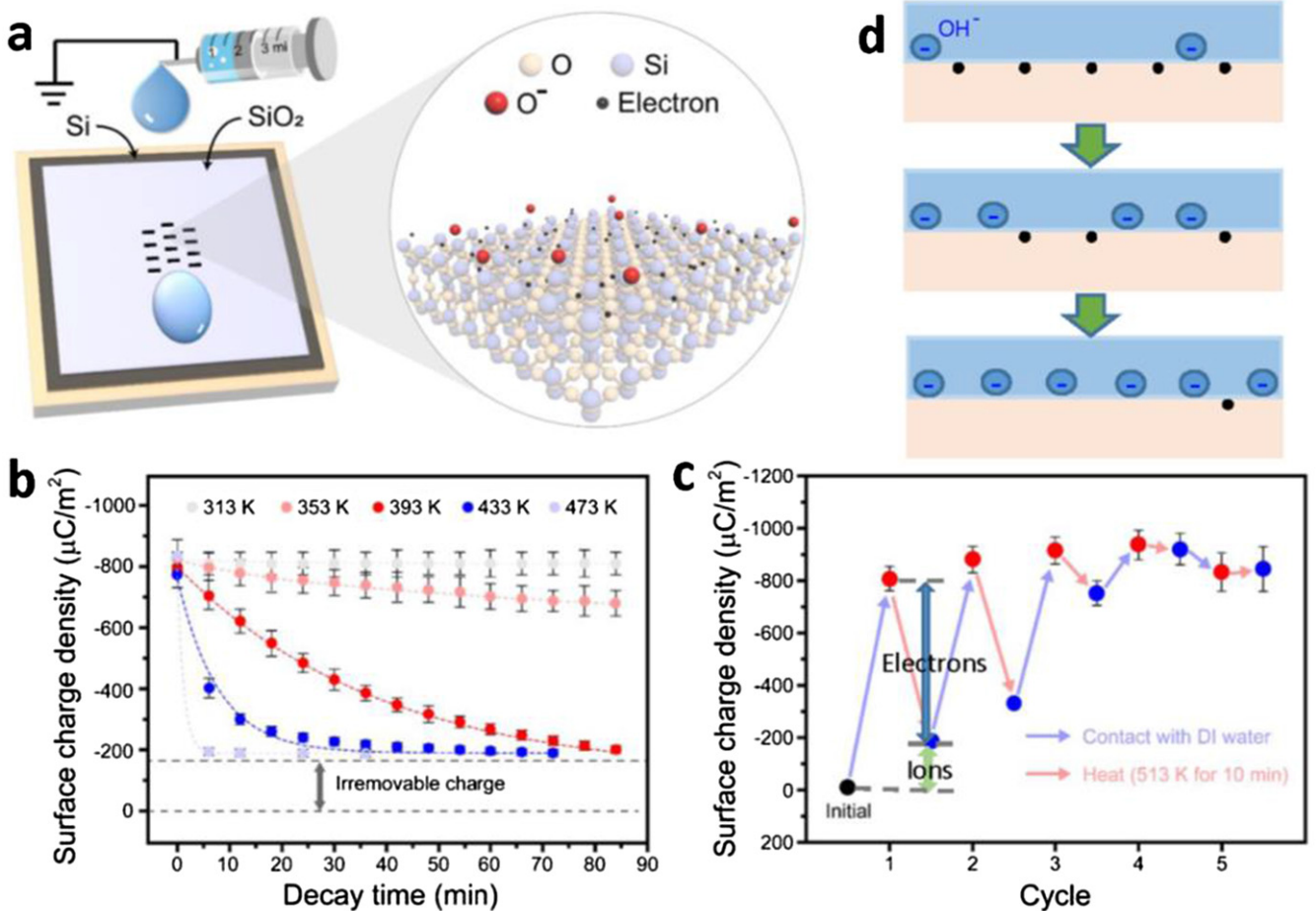


**Figure 13.** Experimental approach for separating electron transfer from ion transfers at the interface between DI water and  $\text{SiO}_2$ . (a) The setup of AFM platform for the thermionic emission experiments. (b) The decay of the CE charges (created by contacting with the DI water at room temperature) on the  $\text{SiO}_2$  surface at different substrate temperatures. (c) The CE charge density on the  $\text{SiO}_2$  sample surface in the repeated charging via liquid contact and repeated heating (at 513 K for 10 min) cycles, showing the ‘substitutions’ of surface-transferred electrons by ions. (d) Schematic illustration of the charge transfer process at the DI water and  $\text{SiO}_2$  interface according to the data shown in (c) after multiple cycles of dropping-heating experiments. Reproduced from [68]. CC BY 4.0.

which is apparently chemical adsorption (figure 14(a)). For the surfaces of  $\text{Si}_3\text{N}_4$ ,  $\text{Ta}_2\text{O}_5$ ,  $\text{HfO}_2$ ,  $\text{Al}_2\text{O}_3$  and  $\text{AlN}$ , the surface loses electrons, but the adsorbed ions can be  $\text{H}^+$  or  $\text{OH}^-$ , indicating that both physical adsorption ( $\text{Si}_3\text{N}_4$ ,  $\text{Ta}_2\text{O}_5$ ,  $\text{HfO}_2$ ) and chemical adsorption ( $\text{Al}_2\text{O}_3$  and  $\text{AlN}$ ) are possible.

The type of ions adsorbed on surfaces can be controlled by the pH of the solution. When the pH value of the solution is 11, the transferred ions on the surfaces of  $\text{Al}_2\text{O}_3$ ,  $\text{AlN}$  and  $\text{Si}_3\text{N}_4$  are negative  $\text{OH}^-$ , but  $\text{Al}_2\text{O}_3$  gains electrons, while  $\text{AlN}$  and  $\text{Si}_3\text{N}_4$  lose electrons, corresponding to physical and chemical adsorptions, respectively (figures 15(a)–(c)). Once the pH is 3, the three surfaces all lose electrons, corresponding to  $\text{H}^+$  physical adsorption (figures 15(e) and (f)).

These results show that no matter what the aqueous solution is, there are always both electron transfers and ion transfers in liquid–solid CE. The electron transfers between aqueous solution and solid are sensitive to solutes in the liquids, such as  $\text{Na}^+$ ,  $\text{Cl}^-$ ,  $\text{OH}^-$  and  $\text{H}^+$ , etc. Meanwhile, ion

transfers are mainly affected by the pH value of the solution, which dominates the ionization reactions on the insulator surfaces.

The charge transfers between deionized water and PTFE are mainly electron transfers. This is further verified by Nie *et al* [69] by using several polymer films with similar main chains but different functional groups on the side chains in order to quantify their behavior in CE with DI water (figure 16). The polymers with strong electron-withdrawing groups on the side chains are more likely to obtain electrons during CE. Among all materials, the fluorine group on the carbon chain shows the strongest electron withdrawing ability, and the fluorinated ethylene propylene (FEP) film with  $-\text{CF}_3$  group can provide the highest charge density. Similar rules can be applied to CE of polymer-Al and polymer-liquid. More importantly, it reveals for the first time the contribution of unsaturated groups on the PTFE molecular chain to CE [70].

**2.2.2. Electron transfer in the formation of electric dipole layer.** CE between liquid–solid is the root of the formation of the electric double layer. The classical model for EDL is an

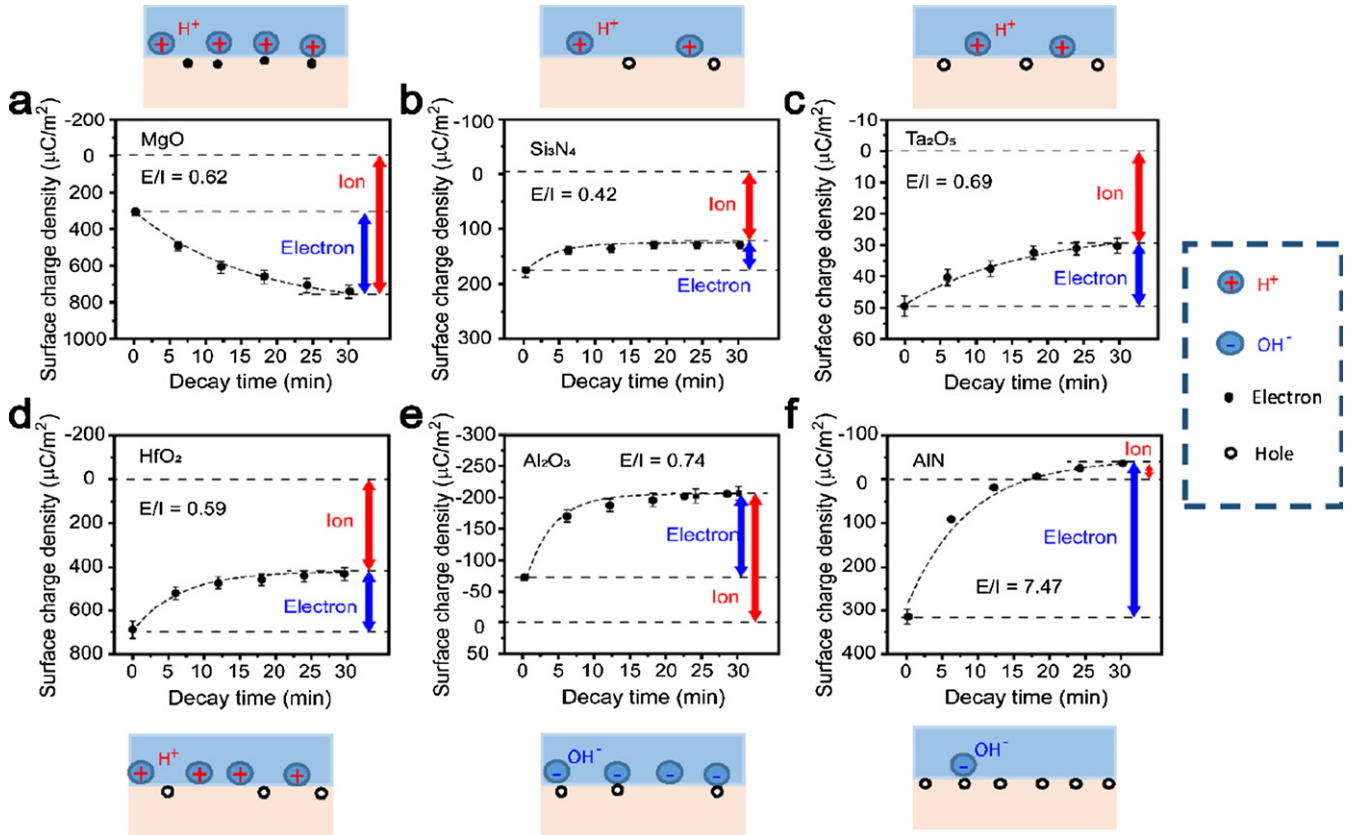


**Figure 14.** Decay of the surface charge density created by the CE between DI water and various solid surfaces at room temperature on (a)  $MgO$ , (b)  $Si_3N_4$ , (c)  $Ta_2O_5$ , (d)  $HfO_2$ , (e)  $Al_2O_3$  and (f) AlN surfaces at 433 K, and the amount of the electron transfer and the ion transfer in the CE between the DI water and different insulators. Based on the number of electron and ion transfers, schematic surface charges and ion adsorption (chemical or physical) are indicated at the tops and bottoms of the corresponding figures. Reproduced from [68]. CC BY 4.0.

adsorption of a layer of ions on the solid surface, which tends to attract the ions of opposite sign of charges, while repelling the ions of the same signs of charges in the solution, forming a distribution of electric potential near the liquid–solid interface. This model is entirely based on there being only ion adsorptions at the liquid–solid interface without including the involvement of electron transfer. Based on the study presented in the last few sections, the formation of EDL must be revised.

Recently, it was proposed by Wang and Wang [29] that the formation of EDL may have two steps. The first step is an electron exchange process between liquid and solid surfaces via CE, which makes the atoms on the solid surface to be ions. The second step is the interaction of the ions with the ions in the liquid, resulting in a gradient distribution of cations and anions near the interface. The traditional model ignores the first step, just considering the second step. In practice, electron exchange and ion adsorption can occur simultaneously and co-exist in the liquid–solid interaction [68, 69]. Such a revision of the model for EDL could subsequently affect some related understanding about the interface chemistry, electrochemistry and even cellular-level interactions. Therefore, for simple reference, the two-step model is called the Wang model for EDL.

Based on the classical model, the EDL refers to two parallel layers of charges surrounding the solid surface. The first layer consists of ions physically adsorbed onto the surface.

The second layer is composed of ions attracted adjacent to the surface via Coulomb interaction to electrically screen the first layer. Considering the liquid property of the solution, this second layer is made of free ions that move in the liquid under the influence of electric attraction and thermal motion rather than being firmly anchored. Although the existence of EDL is a fact, its structure is clear and it has been used for understanding many liquid–solid interface-related chemical processes, a fundamental question is what is the cause for the first layer becoming charged at the very beginning when it first contacts with a liquid? A possibility is the initial electron exchange between liquid molecules and solid surface atoms at the very first contact.

The formation of the EDL is proposed as a two-step process. In the first step, when the molecules in the solution first approach a virgin surface that has no pre-existing surface charges (figure 17(a)), it may be possible that the atoms/molecules in the solution directly interact with the atoms on the solid surface to form a strong overlap of electron clouds; thus, electron transfer is possible as a result of CE at the liquid–solid interface (see figure 10). Electron transfer occurs first to make the ‘neutral’ atoms on the solid surface become charged, i.e. the formation of ions (figure 17(b)). Then the question is what is the ‘molecule’ if a water molecule loses one electron? This may not be simply understood from a single molecule point of view, just as we do in traditional chemistry,

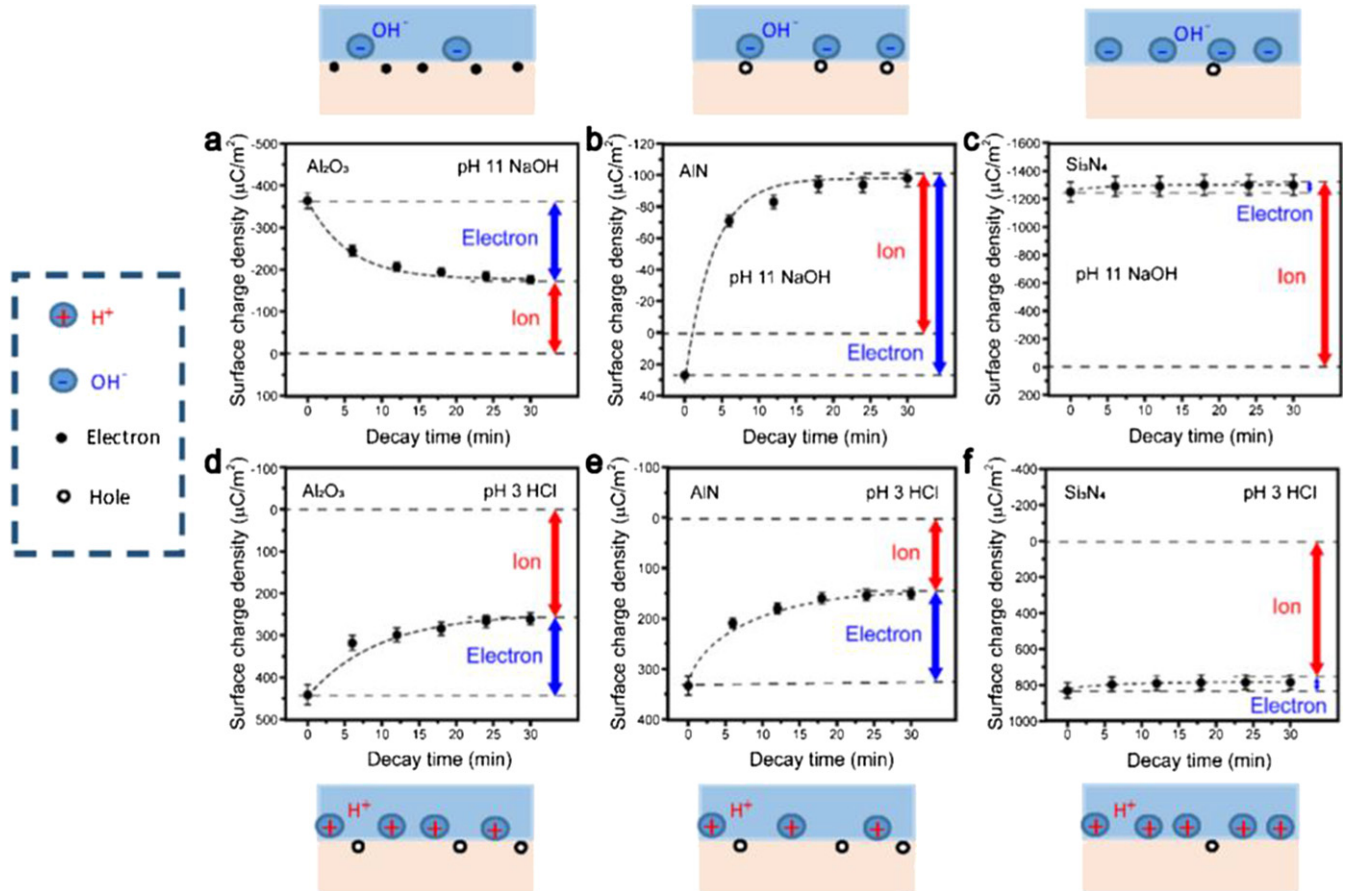


**Figure 15.** The decay of surface charge density on various solid surfaces created by contact with solutions at pH 11 in NaOH solution and pH 3 in HCl solution: (a) Al<sub>2</sub>O<sub>3</sub>, (b) AlN and (c) Si<sub>3</sub>N<sub>4</sub> surfaces at 433 K. Based on the number of electron and ion transfers, schematic surface charges and ion adsorption (chemical or physical) are indicated at the tops and bottoms of the corresponding figures. Reproduced from [68]. CC BY 4.0

but a liquid behavior. A collection of water molecules in liquid can be considered as a unit that are linked by electron interaction. This unit can lose one electron as a whole to the solid surface, so that it cannot be easily understood by the traditional ionic or covalent bond. This is analogous to the band structure for solids; gaining or losing one electron cannot be easily narrowed down to one specific atom, but the matter as a whole. A water molecule could lose an electron and become an H<sub>2</sub>O<sup>+</sup> ion. Recently, using time-resolved x-ray absorption spectroscopy, it has been found that the ionization of H<sub>2</sub>O produces an H<sub>2</sub>O<sup>+</sup> ion [71]. However, the lifetime of H<sub>2</sub>O<sup>+</sup> is about 200 ps before it decomposes into OH + H<sub>3</sub>O<sup>+</sup>. This result supports the proposed model and confirms that electron transfer is possible at the liquid–solid interface. Furthermore, under the pressure of the liquid flow or turbulence as a result of finite temperature, the liquid molecules that are adjacent to the solid surface are thus forced/pushed off of the interface region by breaking the formed ‘bonds’, leaving a layer of ions affixed to the solid surface (figure 17(c)).

In the second step, if there are ions existing in the liquid, such as H<sup>+</sup> and OH<sup>-</sup>, the loosely distributed negative ions in the solution would be tend to migrate toward the surface bonded ions due to electrostatic interactions, forming an EDL. Our suggestion here is that the origin of forming the

EDL is likely the result of CE due to electron transfer at the very first step. Once the EDL is formed, many discussions and models in the literatures regarding related potential distribution and surface chemistry are applicable. Considering the large differences in mass, diffusion rate and sizes, the transport or leakage behavior of the electrons and ions on the surface can be hugely different, which eventually affects the chemical processes at the surfaces for the purpose of energy storage using a supercapacitor, corrosion, redox reaction and ion exchange.

**2.2.3. Liquid–semiconductor case.** As we presented in the last few sections, CE can occur if there is a strong overlap between electron clouds. CE in the liquid–semiconductor case can be interesting because of the semiconductor property. To test this feasibility, we used a metal tip to drag a droplet of DI water on the surface of a silicon wafer back and forth (figure 18(a)). The measured current from silicon into the metal tip is a DC current disregarding the moving direction of the water droplet [48]. A possible explanation is the tribovoltaic effect [29]. Once a water droplet moves on the surface and in the freshly formed liquid–solid interface, electron transfer from water molecules to the semiconductor results in the formation of a bond at the interface, which leads to an

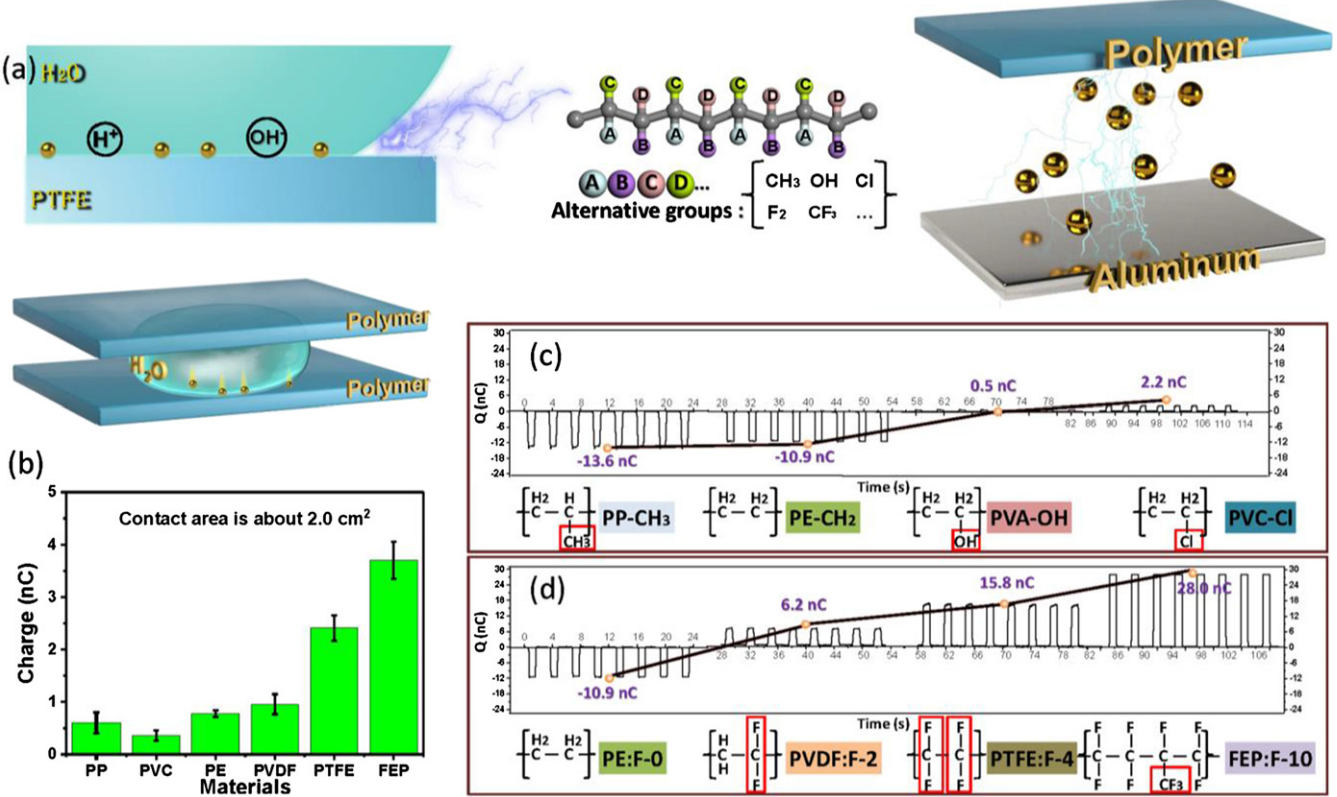


**Figure 16.** (a) CE between deionized water and PTFE includes both ion transfers and electron transfers [69] John Wiley & Sons. © 2020 WILEY-VCH Verlag GmbH & Co. KGaA, Weinheim. (b) and (c) Several polymer films with similar main chains but different functional groups on the side chains have been used to clarify the contribution of functional groups to electrification. The fluorine group on the carbon chain shows the strongest electron withdrawing ability, and the FEP film with  $-CF_3$  group can provide the highest charge density. The unsaturated groups on the PTFE molecular chain have been proved to make very significant contributions to electrification. [70] John Wiley & Sons. © 2020 WILEY-VCH Verlag GmbH & Co. KGaA, Weinheim.

energy release (figures 18(e-i)). Such energy can excite the electron–hole pair at the semiconductor side (figure 18(e-iii)), and the formed junction at the interface separates the electron from the hole, forming a DC current flowing from silicon to water droplet through an external circuit. This experiment proves the existence of electron transfer at the liquid–semiconductor interface.

### 2.3. CE at liquid–liquid interfaces

CE between liquid–liquid pairs should also exist, but it is rather difficult to probe. Recently, by using the single-electrode TENG as a probe, its electrical output has been measured once it is inserted through the paraffin oil/NaOH solution interface (as shown in the inset image of figure 19) [72]. Multiple insertion and pulling out of the TENG probe gives an output current peak as soon as the TENG reaches the interface, as marked in figures 19(c) and (d). The pH dependence of the electrophoretic mobility of the oil droplet, which increases with increased pH of the aqueous phase, suggests that the negative interfacial charges originate from preferential adsorption of hydroxyl ions ( $OH^-$ ) at the oil/water interface [73–75]. A reliable explanation of preferential  $OH^-$  adsorption is that the interfacial water molecules are preferentially oriented with the oxygen atoms toward the hydrophobic phase, thus adsorbing

$OH^-$  through the strong dipole or hydrogen bonding of the  $OH^-$  ions with the hydrogen atoms of the interfacial water molecules (as shown in figure 19(e)). Therefore, when the bottom of the TENG contacts the oil/water interface, the negative charges on the interface will induce an interfacial voltage drop and a corresponding interfacial current ( $I_{\text{interface}}$ ) by electrostatic induction.

A L–L TENG based on the interaction between liquid droplets and liquid membranes was demonstrated [69] (figure 20). The L–L TENG is prepared by passing liquid droplets through a freely suspended liquid membrane, and it has two working modes: grounded membrane mode and precharged membrane mode. The grounded membrane can remove and collect electrostatic charges from solid objects, indicating a permeable sensor or charge filter for electronic applications. Moreover, when a droplet (about  $40\text{ }\mu\text{l}$ ) penetrates a precharged membrane, it can generate an OC voltage of 4 V, an SC current of 60 nA, a transferred charge of 1 nC, and a peak power of 137.4 nW. By alternately stacking two modes of liquid membrane in the vertical direction, a droplet passing through the multi-layer system can increase the amount of power generation several times. The output of the L–L TENG proves the charge exchange between the liquid droplet and the liquid membrane. This study has been recently extended using a sonic wave suspended droplet by contacting

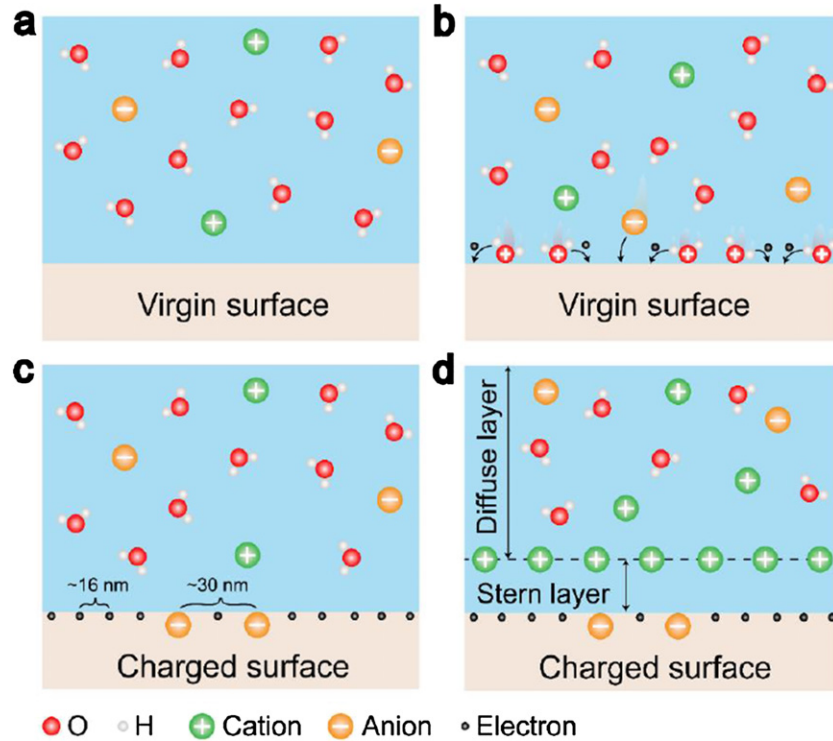


**Figure 17.** A proposed two-step model (Wang model) on the procedures for forming an electric double layer at a liquid–solid interface. The first step: formation of the very first layer of electrostatic charges on the solid surface. (a) Schematic representation of molecules in solution; (b) the adsorption of molecules on the surface and electron transfers resulting in the surface being charged; (c) the adsorbed molecules being pushed off the adsorbed sites due to pressure of the liquid. The second step: segregation of ions in the liquid. (d) The presence of the charged surface as a result of the first step; (e) adsorption of ions in liquid on charged solid surface, forming the EDL. Reproduced from [68]. CC BY 4.0

with a solid ball or a liquid ball. Using TENG as a probe, the charge transfer between a water droplet and oil has also been studied [77]. Both sets of experiments have proved that the charge transfer between oil and water is electron [78]. We are convinced that electron transfer is a general principle for CE among solid–liquid–gas phases.

#### 2.4. Releasing mechanisms of surface charges

**2.4.1. Thermionic emission effect.** Theoretically, the triboelectric charges on insulator surfaces are supposed to remain, but the electrostatic charges on surfaces tend to disappear in ambient conditions, possibly due to three reasons: humidity, temperature and photon excitation. The loss of charges due to humidity can be a screening of surface charges and improved surface conductivity for leakage. The effect of temperature on the surface charges has been studied using TENG, which can be fabricated using temperature-stable materials such as  $\text{Al}_2\text{O}_3$ ,  $\text{SiO}_2$ , Ti and Au. Such an experiment was carried out using TENG operated at different temperatures. The measured total charges  $Q_{\text{sc}}$  flowing under the short circuit condition is a direct measure of the surface charge density. Based on the CS mode, TENG study has revealed a surprising result: TE disappears at high temperatures [25]. A TENG was constructed from thermally stable materials such as Ti and  $\text{SiO}_2$  as shown in figure 21(a), so that the operating temperature could be uniformly increased. Figure 21(a) shows the residual charges on the TENG of measured at different temperatures, and the inset is a schematic diagram of the Ti– $\text{SiO}_2$  TENG. The residual

charges decreased more rapidly with the increase of temperature, and a fast drop is observed when the temperature is higher than 533 K. Figure 21(b) shows the time-dependent change of total output charges  $Q_{\text{sc}}$  of the TENG at temperatures of 353 K, 533 K and 583 K, demonstrating that the charge density decreases more rapidly at higher temperatures. When the temperature reached 583 K, the charges quickly disappeared, similar to the disappearance of magnetism above the Curie temperature.

By quantitatively comparing the charge dissipation curve as a function of temperature, we conclude that the release of charges is best described by the thermionic electron emission model, and the measured  $Q_{\text{sc}}$  values may be fitted according to the thermionic emission equation [79, 80]:

$$J = \lambda A_0 T^2 e^{-\frac{W}{kT}} \left[ e^{\frac{\Delta W}{kT}} - 1 \right], \quad (8)$$

where  $J$  is the current density,  $\lambda$  is the material-specific correction factor,  $A_0$  is the Richardson constant of a free electron,  $T$  is the temperature,  $W$  is the height of the potential barrier,  $k$  is the Boltzmann constant and  $\Delta W$  is the potential barrier height variation due to the surface electric field  $E$ . When  $\Delta W \ll kT$ , the emission current density is related to the total transferred charges in a TENG by Xu *et al* [25].

$$J \approx \frac{\lambda_1 A_0}{k} T e^{-\frac{W}{kT}} Q_{\text{sc}}. \quad (9)$$

Therefore, the dissipation of the charges on the surface follows the electron thermionic emission model.

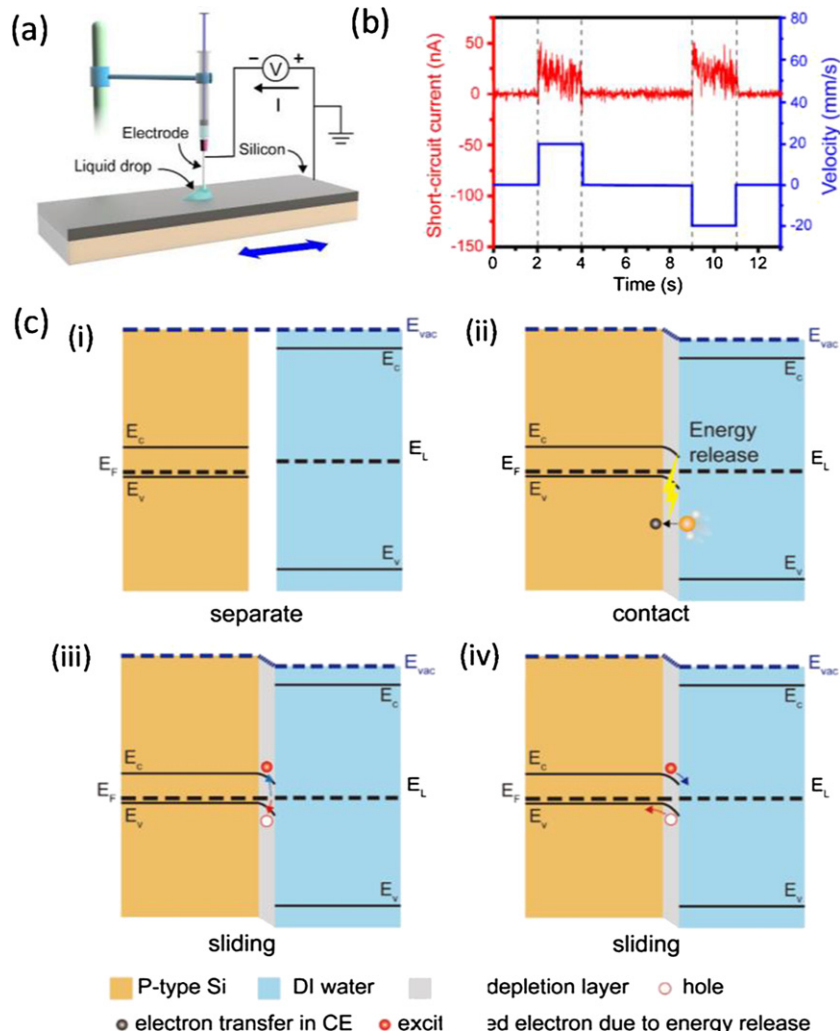


**Figure 18.** The tribovoltaic effect at the DI water–silicon interface. (a) The setup of the tribovoltaic experiments and the external circuit. (b) The output SC current when a DI water droplet slides over a P-type silicon wafer ( $0.1 \Omega \text{ cm}$ ) at  $20 \text{ mm s}^{-1}$ , and the droplet static contact diameter is  $2.5 \text{ mm}$ . (c) Energy band diagram of the tribovoltaic effect at a liquid–solid junction (i) before contact, (ii) in contact, (iii) in sliding, and (iv) with electron–hole separation at the liquid–solid interface in sliding. ( $E_c$  is the bottom of the CB,  $E_F$  is the Fermi level of P-type silicon,  $E_L$  is the ‘Fermi level’ of DI water and  $E_v$  is the top of the VB.) Reprinted from [48], Copyright (2020), with permission from Elsevier.

**2.4.2. Photon excitation effect.** Surface electrostatic charges can also be released under photon excitation, provided its energy is sufficiently high [41]. This process has been investigated by illuminating an insulator surface with light at a specific wavelength and intensity. As shown in figure 21(c), the triboelectric charges on the insulator surface were generated by using the peakforce tapping mode. After the CE, the triboelectric charge density (TECD) on the insulator surface was measured using the KPFM. Furthermore, the charged area on the insulator surface was irradiated by UV light, and the TECD remaining on the surface was measured at fixed time intervals to record the charge decay. Figure 21(d) shows the effect of the incident light wavelength on the decay of triboelectric charges from the  $\text{SiO}_2$  surface. The charge decay rate was fastest when the wavelength was  $240 \text{ nm}$ , and the decay rate decreased with the increase of wavelength. In particular, the number of triboelectric charges remained constant when the wavelength rose up to  $300 \text{ nm}$ . The probability of the electrons, which were

trapped in surface states following CE, being excited out of the surface was the largest under the irradiation of the light with a wavelength of  $240 \text{ nm}$ . When the light wavelength reached up to  $300 \text{ nm}$ , the energy of the photons was not enough to excite the trapped electrons, and the density of the triboelectric charges remained constant. The threshold energy of the incident photons should be higher than  $4.13 \text{ eV}$  to excite the electrons trapped in the surface states of  $\text{SiO}_2$ . The study shows that there exists a threshold photon energy above which surface electrostatic charges will be released. This has been explained by the photoelectron emission model. For the electrons trapped by surface states, a threshold energy is needed in order to excite an electron trapped in surface states into a free electron.

## 2.5. Quantification of triboelectric series

TE is a universal effect that occurs anywhere and at any time for all the materials in solid, liquid and gas states. Even for

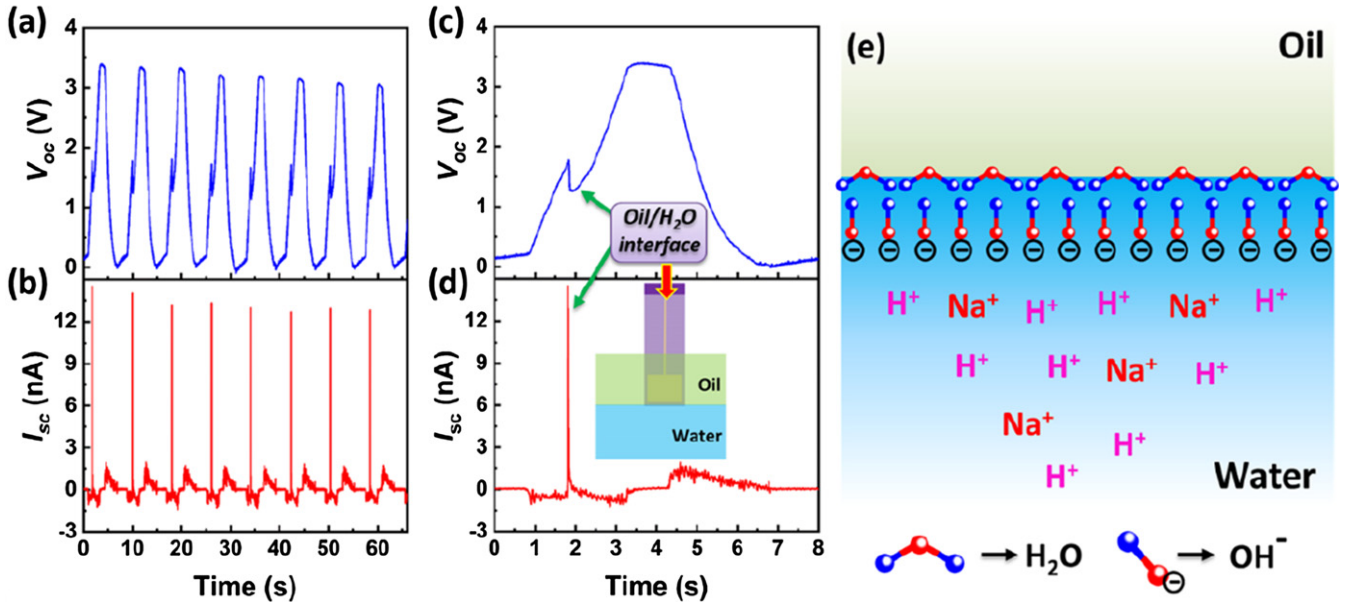


**Figure 19.** TENG as a probe for detecting charge distribution at the liquid–liquid interface. (a) OC voltage ( $V_{oc}$ ) and (b) SC current ( $I_{sc}$ ) of TENG in paraffin oil/water ( $NaOH$ ) multiphase. (c) and (d) Enlarged view of single cycle of  $V_{oc}$  (c) and  $I_{sc}$  (d) (the  $I_{interface}$  is indicated). (e) Schematic illustration of oil/water interfacial charges. [72] John Wiley & Sons. © 2019 WILEY-VCH Verlag GmbH & Co. KGaA, Weinheim.

such a popular effect, the only available source commonly circulated in textbooks is a triboelectric series that gives a very inaccurate qualitative ranking of the triboelectric polarization of some common materials without numerical data. Quantification of CE is difficult due to the following aspects. First, since CE is a two-materials problem, the performance of one material depends on its respective partner. Which material can be the reference partner material for all standardized measurements? Second, CE is a surface property, which is strongly affected by the roughness of the two surfaces, true contact area, surface contamination and atmospheric conditions, as well as humidity. A standardized method must be established to uniformly measure all of the materials.

We recently introduced a universal standard method to quantify the triboelectric series for a wide range of polymers, establishing a fundamental materials property of quantitative TE [81]. To maximize the contact of a material with the reference material, we chose liquid metal as the counter contact, which is likely to have the maximum atomic-scale contact, shape adaptability and softness. This method standardizes the experimental setup for uniformly quantifying the surface TE of general materials. The normalized TECD was defined and derived to reveal the intrinsic tendency of polymers to gain or lose electrons. A table is given regarding the TECD of over 50 organic materials (figure 22) and over 30 functional oxide films (figure 23). The measured results for oxides are closely related to the workfunctions of the materials. This first quantitative triboelectric series will be a textbook standard for implementing the application of TE for energy harvesting and self-powered sensing.

2D materials make an interesting system for investigating CE because of their nanometer thickness. This study has been carried out by Seol *et al* [83] for systems such as  $MoS_2$ ,  $MoSe_2$ ,

$WS_2$ ,  $WSe_2$ , graphene, and graphene oxide. By using the CS mode TENG, the triboelectric series for 2D materials has been established (figure 24), and the results are obviously related to their effective work functions. The charging polarity indicates the similar behavior regardless of the synthetic method and film thickness ranging from a few hundred nanometers to a few nanometers (for chemical vapor deposited films).

### 3. Theory of nanogenerators from expanded Maxwell's equations

Nanogenerators (NGs) are mainly based on three effects: piezoelectricity, triboelectricity, and pyroelectricity. They are called nanogenerators because they were first introduced when using a single  $ZnO$  nanowire as triggered by the tip of an atomic force microscope for converting tiny mechanical energy into electric power. However, with the further physics understanding and development of the field, NGs are now referred to as a field that uses displacement current as the driving force for effectively converting mechanical energy into electric power/signal, disregarding if nanomaterials are used or not. The first piezoelectric NG (PENG) was invented by Wang and Song [84], and the first triboelectric NG (TENG) was invented by Fan *et al* [9]. As of now, research in NGs has attracted worldwide interest owing to their applications as micro-/nano-power sources, self-powered sensors, harvesting blue energy, high-voltage sources and scanning probes [10]. NGs are referred to as the energy technology for the new era—the era of the internet of things [85].

In 2017, Wang [86] expanded the expression of displacement current and first introduced a term  $\mathbf{P}_s$  in  $\mathbf{D}$  for deriving the output power of NGs [87], where  $\mathbf{P}_s$  is the polarization created by the electrostatic surface charges on medium that

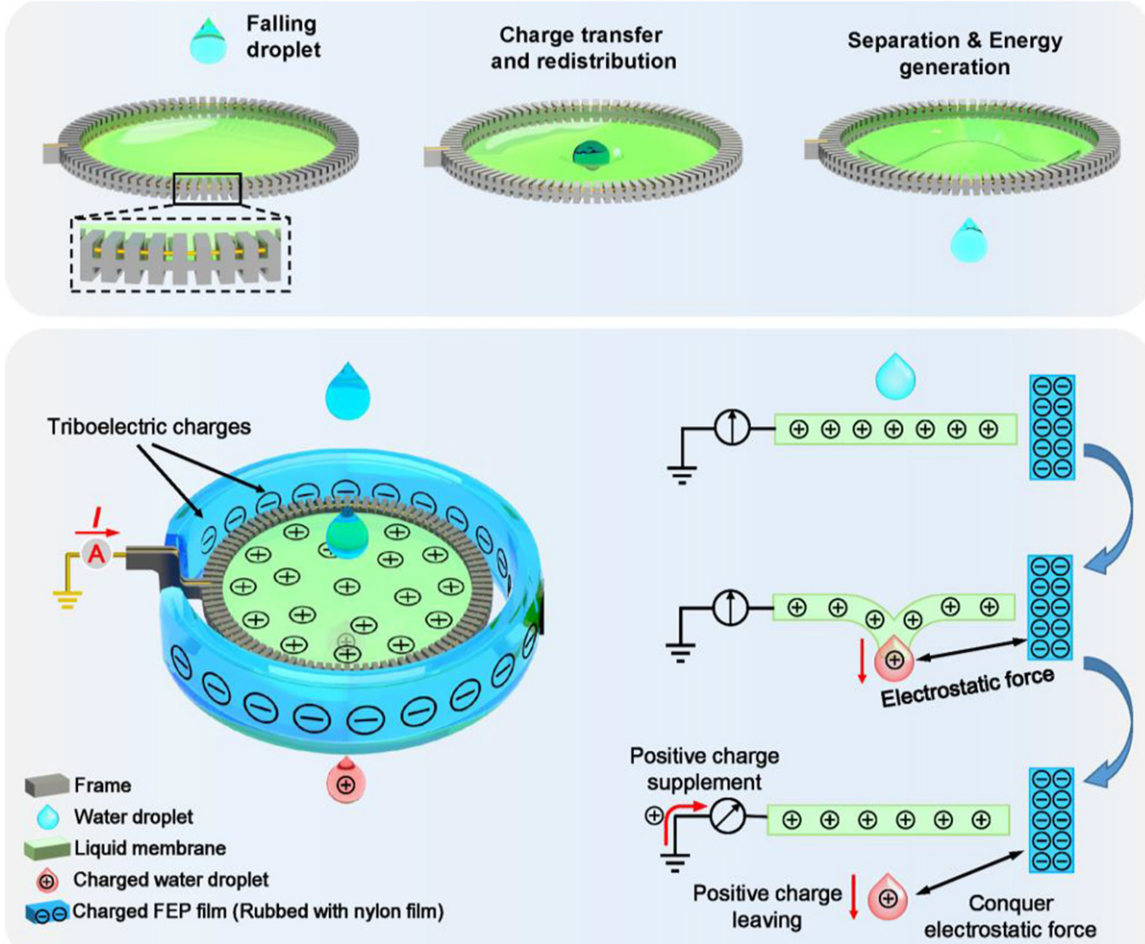


**Figure 20.** A liquid–liquid TENG (L–L TENG) based on the interaction between liquid droplets and liquid membranes. The L–L TENG is prepared by passing liquid droplets through a freely suspended liquid membrane, and the corresponding model for charge exchange. Reproduced from [76]. CC BY 4.0.

'passes-by' in space owing to mechanical triggering, which is different from that of electric field-induced medium polarization  $\mathbf{P}$ . Such charges are from piezoelectric polarization and TE regardless of whether there is an externally applied electric field or not. As a result, the theory for NGs has been set from the first principle point of view. Recently, using the theory of displacement current, theoretical calculations for different modes of TENGs have developed well for explaining the observed power output.

Maxwell's equations are among the top 10 most important equations for physics. Ever since their first introduction in 1861 and theoretical prediction about the existence of electromagnetic (EM) waves, especially after the first experimental observation of EM waves in 1886 by Hertz, Maxwell's equations have been the foundation of modern wireless communication, photonics, light communication and many more. Their vast applications cover almost every corner of our life. The theory of EM waves is a direct result of Maxwell's equations, which is our general understanding about their practical implications. One of the greatest creative ideas by Maxwell in 1861 was the introduction of a displacement current,  $\partial\mathbf{D}/\partial t$ , in Ampere's law, in order to satisfy the conservation law of charges, which resulted in the unification of

electricity and magnetism, where  $\mathbf{D}$  is called the electric displacement vector, based on which Maxwell proves the equivalence of electricity and magnetism. Our general understanding is that Maxwell's equations are the theory for EM wave and light, so that they are most well known in communication and optics sciences. We first start from Maxwell's equations:

$$\nabla \cdot \mathbf{D} = \rho \quad (10)$$

$$\nabla \cdot \mathbf{B} = 0 \quad (11)$$

$$\nabla \times \mathbf{E} = -\frac{\partial \mathbf{B}}{\partial t} \quad (12)$$

$$\nabla \times \mathbf{H} = \mathbf{J} + \frac{\partial \mathbf{D}}{\partial t}. \quad (13)$$

Note that  $\rho$  in equation (10) is the distribution of free charges in space,  $\mathbf{J}$  in equation (13) is the density of free conduction current density in space as a result of charge flow, and  $\mathbf{D}$  is called the electric displacement vector,  $\mathbf{D} = \epsilon_0 \mathbf{E} + \mathbf{P}$ . We know that the effect of polarization with the presence of the electric field is to produce accumulations of bound charges,  $\rho_b = -\nabla \cdot \mathbf{P}$  within the volume of the media and  $\sigma_b = \mathbf{P} \cdot \mathbf{n}$  on the media surface, where the  $\mathbf{P}$  is the medium polarization vector and  $\mathbf{n}$  is the unit vector of the normal direction of the

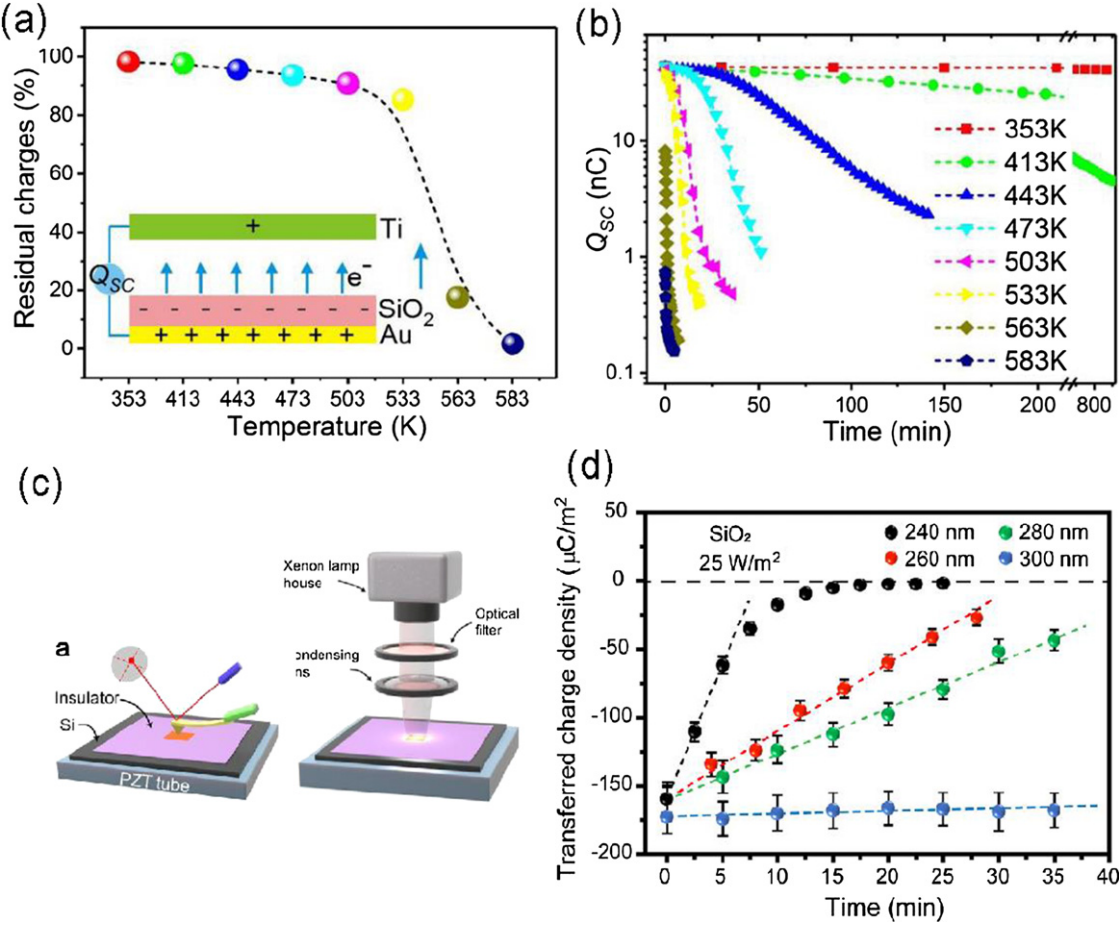


**Figure 21.** (a) and (b) Probing the temperature dependence of the surface charge density in CE by using the output of a TENG, as a new method for quantitative analysis of CE. The TENG is made of a Ti and  $\text{SiO}_2$  pair with metal electrodes at the top and bottom surfaces, respectively. (a) The percentage of residual charges on the TENG measured at different temperatures. Inset is a diagram of the working model of the TENG. (b)  $Q_{SC}$  evolution with time under high temperatures. [25] John Wiley & Sons. © 2018 WILEY-VCH Verlag GmbH & Co. KGaA, Weinheim. (c) and (d) Probing the effect of photon excitation on the CE between an Au-coated tip and  $\text{SiO}_2$  sample by KPFM at the nano-scale. [41] John Wiley & Sons. © 2019 WILEY-VCH Verlag GmbH & Co. KGaA, Weinheim. (c) Schematic illustration of the AFM and UV light irradiation experiments. (d) The effects of light wavelength on the charge decay on  $\text{SiO}_2$  surface.

surface. The field due to polarization of the medium is just the field of the bounded charges.

In general, with the presence of the electric field  $\mathbf{E}$ , the dielectric will be polarized and  $\mathbf{P}$  is expressed as  $\mathbf{P} = (\epsilon - \epsilon_0)\mathbf{E}$  for an isotropic dielectric medium, which is a result of electric field-induced medium polarization. In general,  $\mathbf{P}$  vanishes if  $\mathbf{E} = 0$ . Thus,  $\mathbf{D} = \epsilon\mathbf{E}$ , which means that there is no displacement current if there is no electric field ( $\mathbf{E} = 0$ ), or there is no polarization if there is no external electric field. This is the general case for EM waves, and all of the theories and applications have been developed for this case [88].

It must be pointed out that the Maxwell's equaitons in equations (10)–(13) were derived from the integral form with one important assumption, which is that the volume and surfaces/boundaries of the media are independent of time  $t$ ! In exact, the results derived from Maxwell's equaitons apply only to media whose boundary does not change! However, situation in practice could vary, so that an approximated solution has to be found if the speed at which the boundary moves is relatively slow, so that each moment can be viewed as ‘quasi-static’ situation.

### 3.1. Polarization introduced by dynamic deformation

A NG is made of dielectric media that produce the strain-induced electrostatic charges on surfaces, the electrodes that have free charge distribution  $\rho$ , and interconnect conductive wire across the external load that carries the free-flowing current ( $\mathbf{J}$ ). Once a mechanical agitation is acting on the media (e.g. NG), the distribution and/or configuration of the electrostatic charges and media shapes vary with time; thus, an additional polarization term  $\mathbf{P}_s$  has to be introduced in the displacement vector  $\mathbf{D}$  in order to account for such medium polarization, which is derived as follows. If the surface charge density function  $\sigma_s(\mathbf{r}, t)$  on the surfaces of the media is defined by a shape function of  $f(\mathbf{r}, t) = 0$ , where the time is introduced to represent the instantaneous shape of the media with considering external triggering (figure 25), the equation for defining  $\mathbf{P}_s$  can be expressed as [28]

$$\nabla \cdot \mathbf{P}_s = -\sigma_s(\mathbf{r}, t) \cdot \delta(f(\mathbf{r}, t)), \quad (14)$$

where  $\delta(f(\mathbf{r}, t))$  is a delta function that is introduced to confine the shape of the media  $f(\mathbf{r}, t) = 0$  so that the polarization

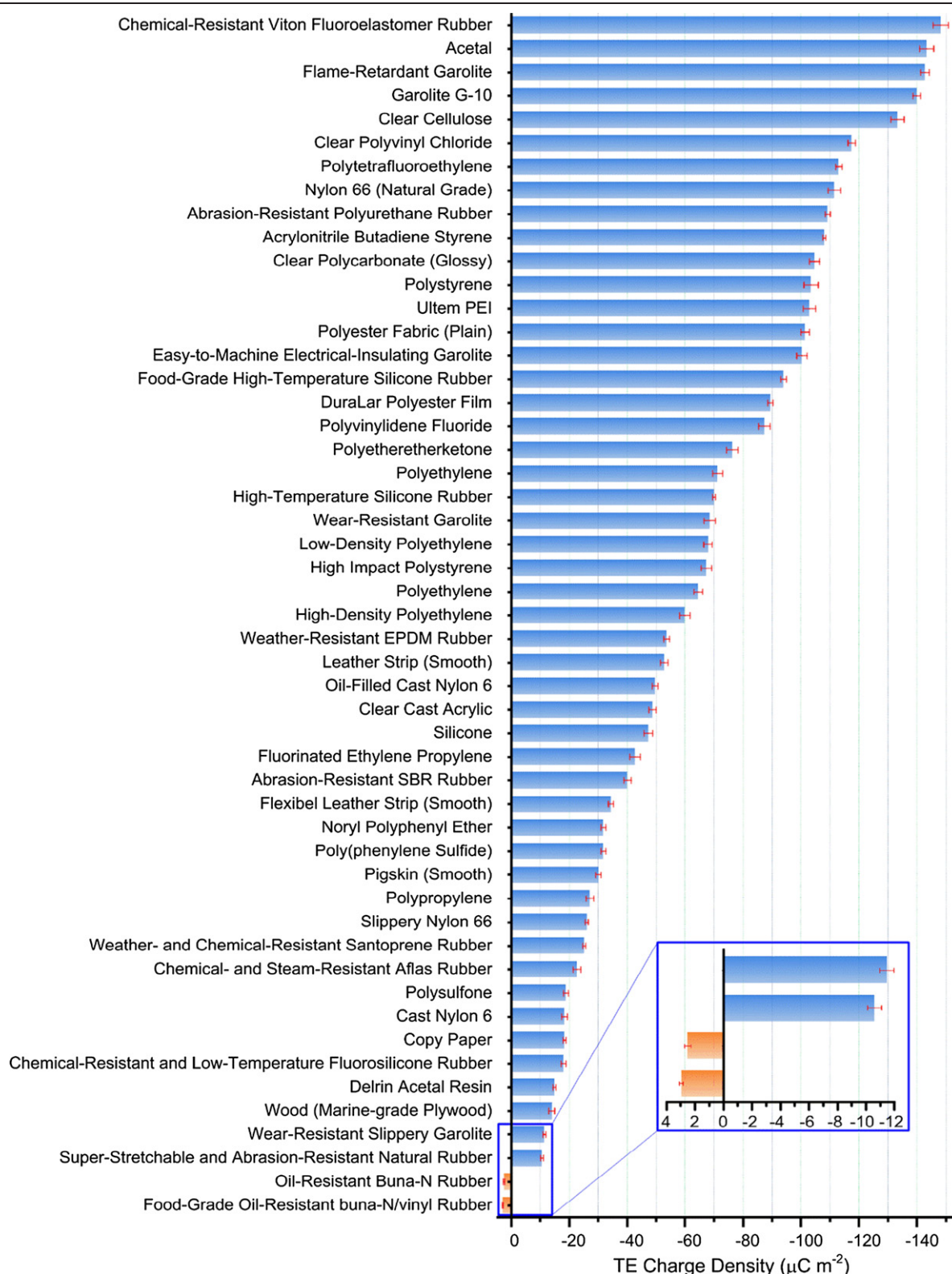


**Figure 22.** Quantified triboelectric series for over 50 different polymer materials. The error bar indicates the range within a standard deviation. Reproduced from [81]. CC BY 4.0.

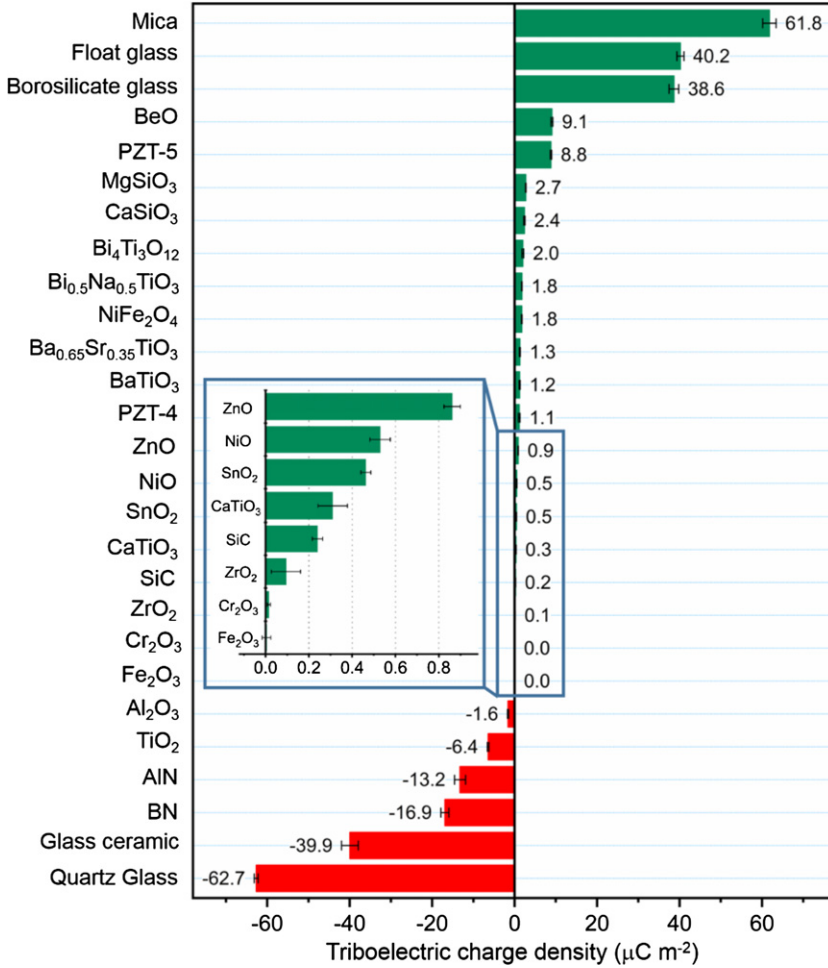


**Figure 23.** Quantified triboelectric series for over 30 different functional oxide materials. Reproduced from [82]. CC BY 4.0.

charges produced by the non-electric field are confined on the medium surface, and which is defined as follows:

$$\delta(f(\mathbf{r}, t)) = \begin{cases} \infty & \text{if } f(\mathbf{r}, t) = 0 \\ 0 & \text{otherwise} \end{cases} \quad (15a)$$

$$\int_{-\infty}^{\infty} \delta(f(\mathbf{r}, t)) d\mathbf{n} = 1, \quad (15b)$$

where  $\mathbf{n}$  is the normal direction of the local surface, and  $d\mathbf{n}$  is an integral along the surface normal direction of the media. This is a simple representation of the charges confined to the surface. It is important to note that the shape of the dielectric media depends on time, and the media distribution also depends on time because of externally applied mechanical triggering, the shape and distribution of the dielectric media can vary, which is the reason for introducing the time  $t$  in  $f(\mathbf{r}, t)$ . If we define the ‘potential’ induced by  $\mathbf{P}_s$  by:  $\mathbf{P}_s = -\nabla\varphi_s(\mathbf{r}, t)$ , we have

$$\nabla^2\varphi_s(\mathbf{r}, t) = \sigma_s(\mathbf{r}, t) \cdot \delta(f(\mathbf{r}, t)). \quad (16)$$

The solution is thus given by

$$\varphi_s(\mathbf{r}, t) = \frac{1}{4\pi} \int \frac{\sigma_s(\mathbf{r}', t') \delta(f(\mathbf{r}', t'))}{|\mathbf{r} - \mathbf{r}'|} d\mathbf{r}' = \frac{1}{4\pi} \int \frac{\sigma_s(\mathbf{r}', t')}{|\mathbf{r} - \mathbf{r}'|} ds', \quad (17)$$

where  $ds'$  is an integral over the surface  $f(\mathbf{r}, t) = 0$  of the dielectric media (figure 25). Therefore, the polarization arising from the surface charge density is

$$\begin{aligned} \mathbf{P}_s &= -\nabla\varphi_s(\mathbf{r}, t) = -\frac{1}{4\pi} \nabla \int \frac{\sigma_s(\mathbf{r}', t')}{|\mathbf{r} - \mathbf{r}'|} ds' \\ &= \frac{1}{4\pi} \int \sigma_s(\mathbf{r}', t') \frac{\mathbf{r} - \mathbf{r}'}{|\mathbf{r} - \mathbf{r}'|^3} ds' \\ &\quad + \frac{1}{4\pi c} \int \frac{\partial \sigma_s(\mathbf{r}'', t')}{\partial t'} \frac{\mathbf{r} - \mathbf{r}'}{|\mathbf{r} - \mathbf{r}'|^2} ds' \end{aligned} \quad (18a)$$

$$\begin{aligned} \frac{\partial \mathbf{P}_s}{\partial t} &= \frac{1}{4\pi} \frac{\partial}{\partial t} \left\{ \int \sigma_s(\mathbf{r}', t) \frac{\mathbf{r} - \mathbf{r}'}{|\mathbf{r} - \mathbf{r}'|^3} ds'(t) \right. \\ &\quad \left. + \frac{1}{c} \int \frac{\partial \sigma_s(\mathbf{r}'', t')}{\partial t'} \frac{\mathbf{r} - \mathbf{r}'}{|\mathbf{r} - \mathbf{r}'|^2} ds'(t) \right\}. \end{aligned} \quad (18b)$$

It is important to note that the shape of the dielectric boundaries/surfaces  $S(t)$  is a function of time since it is being triggered by an external force (figure 25), so that the differentiation over time cannot be simply exchange sequence with the surface integral in equation (18b). As for NGs, so that the time differentiation also applies to the boundary of the dielectric media that changes under external mechanical triggering.

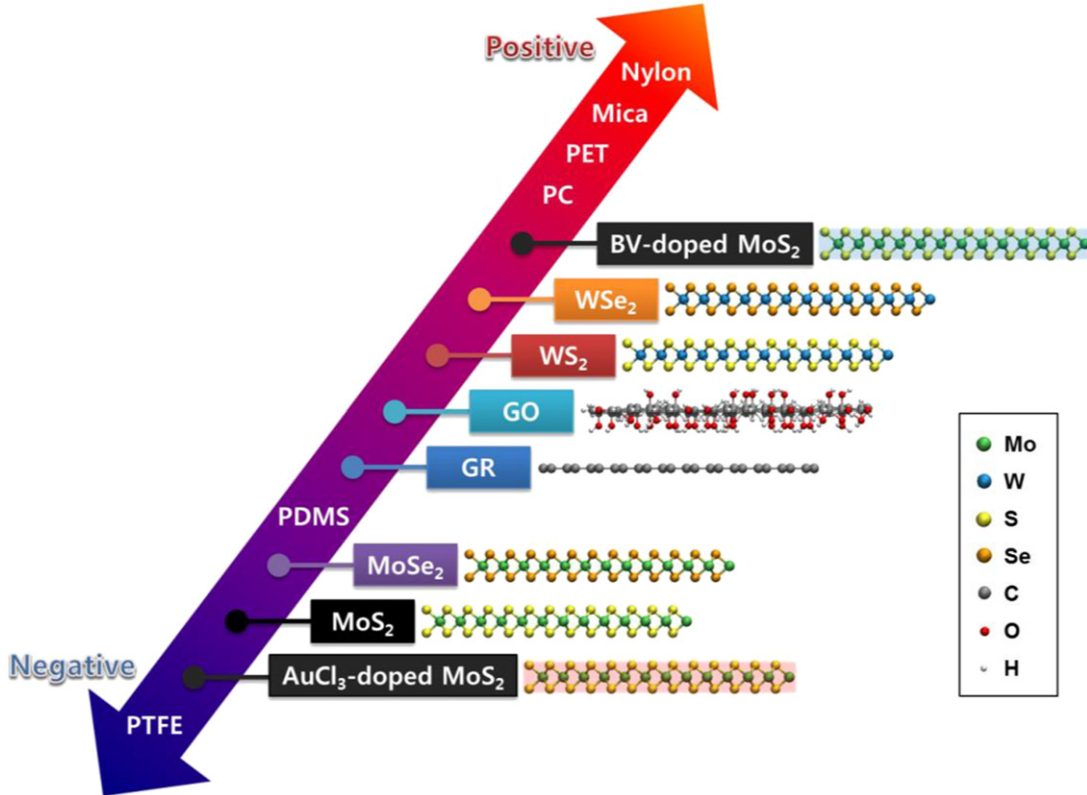


**Figure 24.** Triboelectric series by introducing the 2D materials. The molecular structure is shown on the right of the corresponding material. [83] John Wiley & Sons. © 2018 WILEY-VCH Verlag GmbH & Co. KGaA, Weinheim.

If we ignore the time delay term for the medial moving speed is rather low compare to the speed of light for NGs, which is the case in practice,

$$\mathbf{P}_s \approx \frac{1}{4\pi} \int \sigma_s(\mathbf{r}', t) \frac{\mathbf{r} - \mathbf{r}'}{|\mathbf{r} - \mathbf{r}'|^3} d\mathbf{s}' \quad (19a)$$

$$\frac{\partial \mathbf{P}_s}{\partial t} = \frac{1}{4\pi} \frac{\partial}{\partial t} \left\{ \int \sigma_s(\mathbf{r}', t) \frac{\mathbf{r} - \mathbf{r}'}{|\mathbf{r} - \mathbf{r}'|^3} d\mathbf{s}'(t) \right\}. \quad (19b)$$

### 3.2. Expanded Maxwell's equations

In the piezoelectric case, surface polarization charges are created due to the strain-induced ions on crystal surfaces. In the case of TENGs, triboelectric charges are produced on surfaces simply due to a physical contact between two different materials. To account for the contribution made by the CE-induced electrostatic charges and the medium shape change during mechanical agitation for power generation, an additional term  $\mathbf{P}_s$  is added in  $\mathbf{D}$  by Wang [86] and Wang *et al* [87]:

$$\mathbf{D} = \epsilon_0 \mathbf{E} + \mathbf{P} + \mathbf{P}_s. \quad (20)$$

Here, the first term polarization vector  $\mathbf{P}$  is due to the existence of an external electric field, and the added term  $\mathbf{P}_s$  is mainly due to the existence of the surface charges created by piezoelectric/triboelectric effect and the time variation in boundary shapes during mechanical agitation. Substituting

equation (20) into Maxwell's equations, we define

$$\mathbf{D}' = \epsilon_0 \mathbf{E} + \mathbf{P}. \quad (21)$$

From the above, Maxwell's equations can be expanded into a new set of self-consistent equations [28]:

$$\nabla \cdot \mathbf{D}' = \rho' \quad (22)$$

$$\nabla \cdot \mathbf{B} = 0 \quad (23)$$

$$\nabla \times \mathbf{E} = -\frac{\partial \mathbf{B}}{\partial t} \quad (24)$$

$$\nabla \times \mathbf{H} = \mathbf{J}' + \frac{\partial \mathbf{D}'}{\partial t}. \quad (25)$$

Therefore, the volume charge density and the density of current density can be redefined as

$$\rho' = \rho - \nabla \cdot \mathbf{P}_s \quad (26a)$$

$$\mathbf{J}' = \mathbf{J} + \frac{\partial \mathbf{P}_s}{\partial t} \quad (26b)$$

which satisfies the charge conservation and continuation equation:

$$\nabla \cdot \mathbf{J}' + \frac{\partial \rho'}{\partial t} = 0. \quad (27)$$

From equation (25), the conduction current is  $J$ , and the total displacement current is:

$$\mathbf{J}_D = \frac{\partial \mathbf{D}'}{\partial t} + \frac{\partial \mathbf{P}_s}{\partial t}, \quad (28)$$

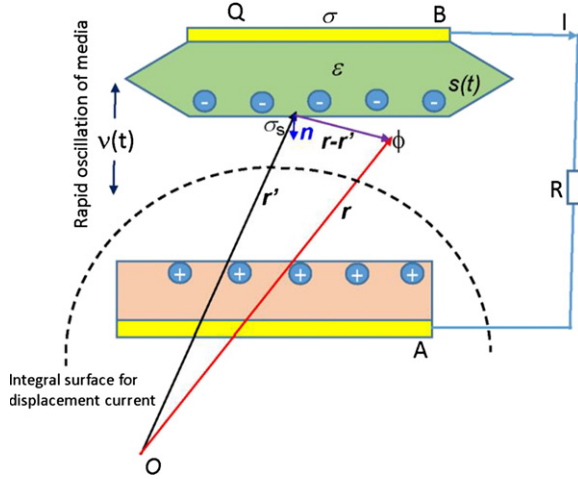


**Figure 25.** Schematic illustration of a general TENG and the associated coordination system for theoretical study.

where  $\frac{\partial \mathbf{D}'}{\partial t}$  represents the displacement current due to time variation of electric field, and the term  $\frac{\partial \mathbf{P}_s}{\partial t}$  is the current due to the change in media boundaries, which is referred to as the Wang term. These equations are the cornerstones for deriving the output characteristics of NGs.

The space distribution of current in the NG is given by equation (26b), where the first term is the observed conduction current across a load (figure 25), and the second term is the displacement current inside the NG that is the driving force for power generation.

### 3.3. General solution in frequency space

To include the frequency in the entire theory, we use the Fourier transform and inverse Fourier transform in time and frequency space as defined by:

$$\mathbf{a}(\mathbf{r}, \omega) = \int_{-\infty}^{\infty} dt e^{i\omega t} \mathbf{a}(\mathbf{r}, t) \quad (29a)$$

$$\mathbf{a}(\mathbf{r}, t) = \frac{1}{2\pi} \int_{-\infty}^{\infty} d\omega e^{-i\omega t} \mathbf{a}(\mathbf{r}, \omega). \quad (29b)$$

Note that we use the same symbols to represent the real space and reciprocal space except the variables. Then, equations (22)–(25) can be transformed in the frequency space as:

$$\nabla \cdot \mathbf{D}'(\mathbf{r}, \omega) = \rho'(\mathbf{r}, \omega) \quad (30)$$

$$\nabla \cdot \mathbf{B}(\mathbf{r}, \omega) = 0 \quad (31)$$

$$\nabla \times \mathbf{E}(\mathbf{r}, \omega) = i\omega \mathbf{B}(\mathbf{r}, \omega) \quad (32)$$

$$\nabla \times \mathbf{H}(\mathbf{r}, \omega) = \mathbf{J}'(\mathbf{r}, \omega) - i\omega \mathbf{D}'(\mathbf{r}, \omega). \quad (33)$$

The purpose of introducing frequency space is to simplify the relationship between the displacement field  $\mathbf{D}'$  and electric field  $\mathbf{E}$ , magnetic field  $\mathbf{H}$  and magnetic flux density  $\mathbf{B}$  as follows:

$$\mathbf{D}'(\mathbf{r}, \omega) = \varepsilon(\omega) \mathbf{E}(\mathbf{r}, \omega) \quad (34)$$

$$\mathbf{B}(\mathbf{r}, \omega) = \mu(\omega) \mathbf{H}(\mathbf{r}, \omega). \quad (35)$$

Otherwise,  $\mathbf{D}'$  is a convolution of  $\varepsilon$  and  $\mathbf{E}$  in time space. We now use the Hertz vector  $\Pi(\mathbf{r}, \omega)$  to reformulate Maxwell's equations [89], by defining

$$\mathbf{E}(\mathbf{r}, \omega) = \nabla [\nabla \cdot \Pi(\mathbf{r}, \omega)] + \mu \varepsilon(\omega) \omega^2 \Pi(\mathbf{r}, \omega) \quad (36)$$

$$\mathbf{H}(\mathbf{r}, \omega) = -i\omega \varepsilon(\omega) \nabla \times \Pi(\mathbf{r}, \omega). \quad (37)$$

Substitute equations (36) and (37) to equation (33),

$$\begin{aligned} \nabla \times \mathbf{H}(\mathbf{r}, \omega) &= -i\omega \varepsilon(\omega) \nabla \times [\nabla \times \Pi] \\ &= -i\omega \varepsilon(\omega) [\nabla (\nabla \cdot \Pi) - \nabla^2 \Pi] \\ &= \mathbf{J}' - i\omega \varepsilon(\omega) [\nabla (\nabla \cdot \Pi) + \mu \varepsilon \omega^2 \Pi]. \end{aligned} \quad (38)$$

So, we have:

$$(\nabla^2 + \omega^2 \varepsilon(\omega) \mu(\omega)) \Pi(\mathbf{r}, \omega) = \frac{\mathbf{J}'(\mathbf{r}, \omega)}{i\omega \varepsilon}. \quad (39)$$

It can be proved that equations (30)–(32) are automatically satisfied with the use of equation (39) and charge conservation law:

$$\nabla \cdot \mathbf{J}'(\mathbf{r}, \omega) - i\omega \rho'(\mathbf{r}, \omega) = 0. \quad (40)$$

The full solution of Hertz vector has two components: homogeneous solution that is determined by:

$$(\nabla^2 + \omega^2 \varepsilon \mu) \Pi_h(\mathbf{r}, \omega) = 0. \quad (41)$$

And a special solution that satisfies:

$$(\nabla^2 + \omega^2 \varepsilon \mu) \Pi_s(\mathbf{r}, \omega) = \frac{\mathbf{J}'(\mathbf{r}, \omega)}{i\omega \varepsilon}. \quad (42)$$

The special solution  $\Pi_s$  can be derived using Green's function [88],

$$\Pi_s(\mathbf{r}, \omega) = -\frac{1}{4\pi i\omega \varepsilon} \int \frac{\exp[i\omega \sqrt{\varepsilon \mu} |\mathbf{r} - \mathbf{r}'|]}{|\mathbf{r} - \mathbf{r}'|} \mathbf{J}'(\mathbf{r}', \omega) d\mathbf{r}'. \quad (43)$$

$\mathbf{E}$  and  $\mathbf{B}$  can be calculated from  $\Pi = \Pi_h + \Pi_s$ . In the classical electrodynamics, the total solution needs to satisfy the following boundary conditions:

$$[\mathbf{E}_1(\mathbf{r}, \omega) - \mathbf{E}_2(\mathbf{r}, \omega)] \times \mathbf{n}(\mathbf{r}) = 0 \quad (44a)$$

$$[\mathbf{B}_2(\mathbf{r}, \omega) - \mathbf{B}_1(\mathbf{r}, \omega)] \cdot \mathbf{n}(\mathbf{r}) = 0 \quad (44b)$$

$$\mathbf{n}(\mathbf{r}) \times [\mathbf{H}_2(\mathbf{r}, \omega) - \mathbf{H}_1(\mathbf{r}, \omega)] = \mathbf{j}'_s(\mathbf{r}, \omega) \quad (44c)$$

$$[\mathbf{D}'_2(\mathbf{r}, \omega) - \mathbf{D}'_1(\mathbf{r}, \omega)] \cdot \mathbf{n}(\mathbf{r}) = \sigma'(\mathbf{r}, \omega), \quad (44d)$$

where  $\mathbf{n}(\mathbf{r})$  is a unit vector normal to the interface/boundary pointing from medium-1 into medium-2. The quantity  $\sigma'$  is the surface charge density on the boundary surface/interface, such as the surface charge density on dielectric surface  $\sigma_s$  and that on the surface of conductive electrode  $\sigma$  (figure 25).  $\mathbf{j}'_s$  is the surface current density.

It must be pointed out that the condition for applying the boundary conditions in equations (44a)–(44d) is that the shapes of the dielectric media and the boundary are independent of time so that they are fixed boundaries. This is the

case for most of the EM wave cases, as assumed in classical electrodynamics.

However, if the boundaries of the dielectric media do vary with time so that  $\mathbf{n}(\mathbf{r}, t)$  is a function of time, under the quasi-static approximation, the boundary condition must be met in time space rather than in frequency space:

$$[\mathbf{E}_1(\mathbf{r}, t) - \mathbf{E}_2(\mathbf{r}, t)] \times \mathbf{n}(\mathbf{r}, t) = 0 \quad (45a)$$

$$[\mathbf{B}_2(\mathbf{r}, t) - \mathbf{B}_1(\mathbf{r}, t)] \cdot \mathbf{n}(\mathbf{r}, t) = 0 \quad (45b)$$

$$\mathbf{n}(\mathbf{r}, t) \times [\mathbf{H}_2(\mathbf{r}, t) - \mathbf{H}_1(\mathbf{r}, t)] = \mathbf{j}'_s(\mathbf{r}, t) \quad (45c)$$

$$[\mathbf{D}'_2(\mathbf{r}, t) - \mathbf{D}'_1(\mathbf{r}, t)] \cdot \mathbf{n}(\mathbf{r}, t) = \sigma'(\mathbf{r}, t), \quad (45d)$$

where all  $\mathbf{E}(\mathbf{r}, t)$ ,  $\mathbf{D}'(\mathbf{r}, t)$ ,  $\mathbf{B}(\mathbf{r}, t)$  and  $\mathbf{H}(\mathbf{r}, t)$  are the inverse Fourier transforms of  $\mathbf{E}(\mathbf{r}, \omega)$ ,  $\mathbf{D}'(\mathbf{r}, \omega)$ ,  $\mathbf{B}(\mathbf{r}, \omega)$  and  $\mathbf{H}(\mathbf{r}, \omega)$ , respectively. This is the case for TENG in general, and it may be essential if the media moving speed is rather high.

To make the calculation realistic and easy to accomplish, an approximation can be made that the boundary conditions are met in frequency space under a quasi-static approximation if the moving speed of the media is much smaller than the speed of light, which is the case for all of the practical applications. The quasi-static approximation means that at any given time  $t$ , the EM behavior can be described using Maxwell's equations, and the boundary/interface can be treated as instantaneously 'static' so that it does not have to be converted into the frequency space.

**3.3.1. Case a: the dielectric permittivity of the media is independent of frequency.** In this case, we need to start from the time-dependent Maxwell's equations using the Hertz vector [90], and the electric field and magnetic field can be stated as:

$$\mathbf{E}(\mathbf{r}, t) = \nabla[\nabla \cdot \mathbf{\Pi}(\mathbf{r}, t)] - \mu\epsilon \frac{\partial^2 \mathbf{\Pi}(\mathbf{r}, t)}{\partial t^2} \quad (46)$$

$$\mathbf{H}(\mathbf{r}, t) = \epsilon \nabla \times \frac{\partial \mathbf{\Pi}(\mathbf{r}, t)}{\partial t}. \quad (47)$$

Maxwell's equations become:

$$\left[ \nabla^2 \mathbf{\Pi}(\mathbf{r}, t) - \mu\epsilon \frac{\partial^2 \mathbf{\Pi}(\mathbf{r}, t)}{\partial t^2} \right] = -\frac{\mathbf{P}_J(\mathbf{r}, t) + \mathbf{P}_s(\mathbf{r}, t)}{\epsilon}, \quad (48)$$

where  $\mathbf{P}_J$  is a vector that is related to the free current density  $\mathbf{J}$  by:

$$\mathbf{J} = \frac{\partial \mathbf{P}_J(\mathbf{r}, t)}{\partial t}. \quad (49)$$

The homogeneous solution of equation (48) is

$$\left[ \nabla^2 \mathbf{\Pi}_h(\mathbf{r}, t) - \mu\epsilon \frac{\partial^2 \mathbf{\Pi}_h(\mathbf{r}, t)}{\partial t^2} \right] = 0. \quad (50)$$

And the special solution of equation (48) is

$$\mathbf{\Pi}_s(\mathbf{r}, t) = \frac{1}{4\pi\epsilon} \int \frac{\mathbf{P}_J(\mathbf{r}', t') + \mathbf{P}_s(\mathbf{r}', t')}{|\mathbf{r} - \mathbf{r}'|} d\mathbf{r}', \quad (51)$$

where  $t' = t - \sqrt{\epsilon\mu} |\mathbf{r} - \mathbf{r}'|$ . The total solution needs to satisfy the boundary conditions in equations (45a)–(45d).

**3.3.2. Case b: ignoring retardation by assuming  $\mathbf{c} \rightarrow \infty$ .** In such a case, the permittivity can still depend on frequency, starting from equation (41)

$$\nabla^2 \mathbf{\Pi}_h(\mathbf{r}, \omega) \cong 0. \quad (52)$$

And the special solution that satisfies:

$$\nabla^2 \mathbf{\Pi}_s(\mathbf{r}, \omega) \cong \frac{\mathbf{J}'(\mathbf{r}, \omega)}{i\omega\epsilon}. \quad (53)$$

The solution of which is given by:

$$\mathbf{\Pi}_s(\mathbf{r}, \omega) = -\frac{1}{4\pi i\omega\epsilon} \int \frac{\mathbf{J}'(\mathbf{r}', \omega)}{|\mathbf{r} - \mathbf{r}'|} d\mathbf{r}'. \quad (54)$$

The electric field and magnetic field can be calculated by

$$\mathbf{E}(\mathbf{r}, \omega) \cong \nabla[\nabla \cdot \mathbf{\Pi}(\mathbf{r}, \omega)] \quad (55)$$

$$\mathbf{H}(\mathbf{r}, \omega) \cong -i\omega\epsilon \nabla \times \mathbf{\Pi}(\mathbf{r}, \omega). \quad (56)$$

The same boundary conditions as specified in equations (44a)–(44d) apply if the boundaries are time-independent, which is an excellent approximation for PENG and pyroelectric NG, in both cases the volume or shape change of the dielectric media is negligible. If the potential distribution is defined as

$$\mathbf{E}(\mathbf{r}, \omega) = -\nabla\phi(\mathbf{r}, \omega) \quad (57)$$

$$\phi(\mathbf{r}, \omega) = -\nabla \cdot \mathbf{\Pi}(\mathbf{r}, \omega). \quad (58)$$

The total displacement current is given by

$$\begin{aligned} \mathbf{J}_D(\mathbf{r}, \omega) &= -i\omega\mathbf{D}'(\mathbf{r}, \omega) - i\omega\mathbf{P}_s(\mathbf{r}, \omega) \\ &= -i\omega\{\epsilon\nabla[\nabla \cdot \mathbf{\Pi}(\mathbf{r}, \omega)] + \mathbf{P}_s(\mathbf{r}, \omega)\}. \end{aligned} \quad (59)$$

$\mathbf{P}_s(\mathbf{r}, \omega)$  is the Fourier transform of

$$\mathbf{P}_s(\mathbf{r}, t) = \frac{1}{4\pi} \int \sigma_s(\mathbf{r}', t) \frac{\mathbf{r} - \mathbf{r}'}{|\mathbf{r} - \mathbf{r}'|^3} ds(t) \quad (60)$$

but do note that the shape function of the dielectric media can be time-dependent such as for TENG.

**3.3.3. Case c: assume  $\mathbf{c} \rightarrow \infty$  and the permittivity does not depend on frequency.** In this case, equations (46) and (47) become:

$$\mathbf{E}(\mathbf{r}, t) \cong \nabla[\nabla \cdot \mathbf{\Pi}(\mathbf{r}, t)] \quad (61)$$

$$\mathbf{H}(\mathbf{r}, t) \cong \epsilon \nabla \times \frac{\partial \mathbf{\Pi}(\mathbf{r}, t)}{\partial t}. \quad (62)$$

The Maxwell's equations become:

$$\nabla^2 \mathbf{\Pi}(\mathbf{r}, t) = -\frac{\mathbf{P}_J(\mathbf{r}, t) + \mathbf{P}_s(\mathbf{r}, t)}{\epsilon}. \quad (63)$$

The homogeneous solution of which is

$$\nabla^2 \mathbf{\Pi}_h(\mathbf{r}, t) \cong 0. \quad (64)$$

And the special solution that satisfies:

$$\Pi_s(\mathbf{r}, t) = \frac{1}{4\pi\epsilon} \int \frac{\mathbf{P}_J(\mathbf{r}', t) + \mathbf{P}_s(\mathbf{r}', t)}{|\mathbf{r} - \mathbf{r}'|} d\mathbf{r}'. \quad (65)$$

The total solution satisfies boundary condition equations (45a)–(45d).

**3.3.4. The output of the NG.** As for TENG, the configuration of the dielectric media sensitively depends on time and the degree of shape change is significant. If the potential distribution is defined as

$$\mathbf{E}(\mathbf{r}, t) = -\nabla\phi(\mathbf{r}, t) \quad (66)$$

$$\phi(\mathbf{r}, t) = -\nabla \cdot \Pi(\mathbf{r}, t). \quad (67)$$

The total displacement current is given by

$$\mathbf{J}_D(\mathbf{r}, t) = \epsilon\nabla \left[ \nabla \cdot \frac{\partial\Pi(\mathbf{r}, t)}{\partial t} \right] + \frac{\partial\mathbf{P}_s(\mathbf{r}, t)}{\partial t}. \quad (68)$$

Note that the time differentiation needs to consider the change in the shape and volume of the dielectric media during mechanical triggering.

**3.3.4.1. The output voltage.** The output potential  $\phi$  of TENG is determined by:

$$\mathbf{E}(\mathbf{r}, t) = -\nabla\phi(\mathbf{r}, t) \quad (69)$$

$$\epsilon\nabla^2\phi(\mathbf{r}, t) = -\rho'(\mathbf{r}, t). \quad (70)$$

The corresponding boundary conditions are:

$$[\mathbf{E}_1(\mathbf{r}, t) - \mathbf{E}_2(\mathbf{r}, t)] \times \mathbf{n}(\mathbf{r}, t) = 0 \quad (71a)$$

$$[\mathbf{D}'_2(\mathbf{r}, t) - \mathbf{D}'_1(\mathbf{r}, t)] \cdot \mathbf{n}(\mathbf{r}, t) = \sigma'(\mathbf{r}, t). \quad (71b)$$

**3.3.4.2. The output current.** The total displacement current is an integration of the current density over the surface of the receiving plane:

$$I_D(t) = \int \left[ \frac{\partial\mathbf{D}'(\mathbf{r}, t)}{\partial t} + \frac{\partial\mathbf{P}_s(\mathbf{r}, t)}{\partial t} \right] ds. \quad (72)$$

If the integral of the surface is for a fully enclosed surface:

$$I_D(t) = \frac{\partial}{\partial t} \int \nabla \cdot [\mathbf{D}'(\mathbf{r}, t) + \mathbf{P}_s(\mathbf{r}, t)] d\mathbf{r} = \frac{\partial}{\partial t} \int \rho d\mathbf{r} = \frac{\partial Q(t)}{\partial t}, \quad (73)$$

where  $Q$  is the total free charges on the electrode.

There are two types of electric currents in nature: the conduction current that is the result of free electron flow, and the displacement current that is contributed by the time-varying electric field per Maxwell's definition (figure 26). The EM generator is based on the Lorentz force driven electron flow in conduction wire, which is the major principle for power generation. Meanwhile for piezoelectric, pyroelectric, triboelectric, electrostatic and electret effects-based generators, the current is driven by the displacement current inside the generator. This type of generator is called NGs that physically represent a field

that uses displacement current as the driving force for effectively converting mechanical energy into electric power/signal. Equation (73) means that the internal circuit in the NG is dominated by the displacement current, and the observed current in the external circuit is the capacitive conduction current. The internal circuit and external circuit meet at the two electrodes, forming a complete loop. Therefore, the displacement current is the intrinsic physical core of current generation and it is the internal driving force, and the capacitive conduction current in an external circuit is the external manifestation of the displacement current (see the bottom of figure 26).

**3.3.4.3. The output power.** By calculating the potential drop from the  $B$  electrode to the  $A$  electrode (figure 25), the transport equation across the load  $R$  is:

$$\phi_{BA} = \int_A^B \mathbf{E}(\mathbf{r}, t) \cdot d\mathbf{L} = R \frac{\partial Q(\mathbf{r}, t)}{\partial t}. \quad (74)$$

This is the transport equation for the TENG, which needs to be solved using the boundary condition  $Q(t=0)=0$ . The power delivered to the load is:

$$p = \left[ \frac{\partial Q}{\partial t} \right]^2 R. \quad (75)$$

### 3.4. General integral solutions

The general solution presented in section 3.3 applies to any case if proper boundary conditions are considered. However, such solutions are rather complex and only a numerical solution is possible. In some cases, a simplified solution is needed. As for cases where the dielectric materials for fabricating the TENG are rather thin, and the volume occupied by dielectrics and electrodes based on thin films and sheets is rather small in comparison to the open space between the layers, the solution based on the integral expression of the Maxwell's equations can be reasonably applied. This is reasonable because the polarization in the very thin media can be approximately ignored in comparison to the polarization introduced by the triboelectric surface charges. For simplicity, we ignore the frequency dependence of the dielectric permittivity for quasi-electrostatic cases. The vector magnetic potential  $\mathbf{A}$  is introduced:

$$\mathbf{B} = \nabla \times \mathbf{A} \quad (76)$$

and the scalar electric potential  $\varphi$  is defined:

$$\mathbf{E} = -\nabla\varphi - \frac{\partial\mathbf{A}}{\partial t}. \quad (77)$$

Substituting equations (76) and (77) into equations (22)–(24) and making use of the Lorentz gauge,  $\nabla \cdot \mathbf{A} + \mu\epsilon\frac{\partial\varphi}{\partial t} = 0$ , we have

$$\nabla^2\mathbf{A} - \mu\epsilon\frac{\partial^2\mathbf{A}}{\partial t^2} = -\mu\mathbf{J}'. \quad (78)$$

A corresponding wave equation for the scalar potential  $\varphi$  can be obtained:

$$\nabla^2\varphi - \mu\epsilon\frac{\partial^2\varphi}{\partial t^2} = -\frac{\rho'}{\epsilon}. \quad (79)$$

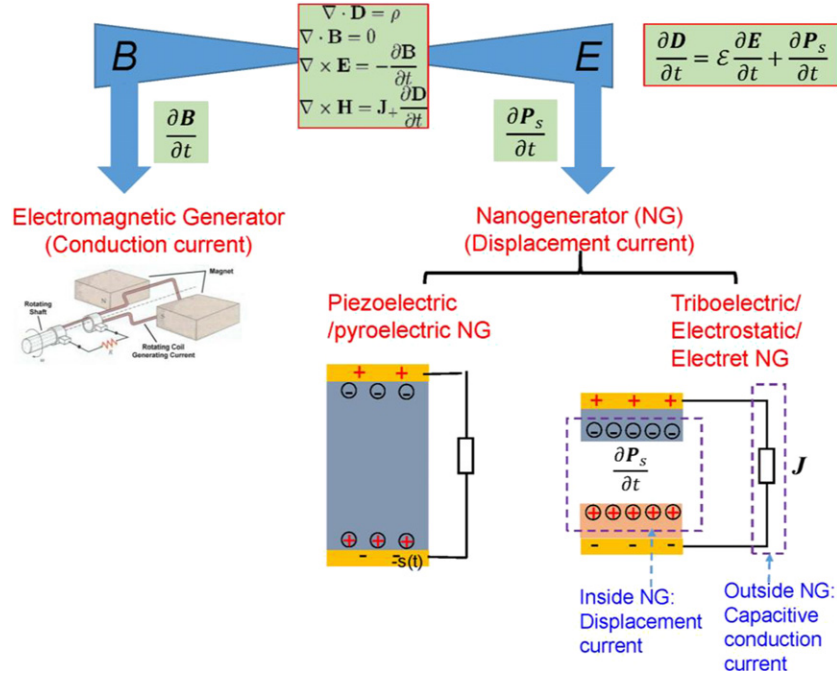


**Figure 26.** Schematic showing the conduction current-dominated EM generator and displacement current-dominated NGs based on piezoelectric/pyroelectric, triboelectric/electrostatic/electret effects. The difference and relationship between the two are illustrated.

which is a nonhomogeneous wave equation for scalar potential  $\varphi$ . Once the solution of  $\mathbf{A}$  and  $\varphi$  can be found, the total electric field  $\mathbf{E}$  and magnetic field  $\mathbf{B}$  can be calculated.

The solution of equations (78) and (79) has two components: a homogenous solution and a special solution; the total solution has to satisfy the boundary conditions. The special solution can be derived as follows. Follow the standard procedures as presented in Jackson's text book on electrodynamics [see chapter 6 in Jackson, 1999] [88], using the definition of Green function and delta function, the integral form of the potential due to a charge distribution over a volume is given by:

$$\varphi(\mathbf{r}, t) = \frac{1}{4\pi\epsilon_0} \int \frac{\rho'(\mathbf{r}', t - |\mathbf{r} - \mathbf{r}'|/c)}{|\mathbf{r} - \mathbf{r}'|} d\mathbf{r}' \quad (80)$$

$$\mathbf{A}(\mathbf{r}, t) = \frac{\mu_0}{4\pi} \int \frac{\mathbf{J}'(\mathbf{r}', t - |\mathbf{r} - \mathbf{r}'|/c)}{|\mathbf{r} - \mathbf{r}'|} d\mathbf{r}', \quad (81)$$

where the retarded time  $t'$  is given by:

$$t' = t - |\mathbf{r} - \mathbf{r}'|/c. \quad (82)$$

**3.4.1. Solutions for potential fields.** By including the contributions from the free charges and free conduction current, the total electric potential in space is [28]:

$$\varphi(\mathbf{r}, t) = \frac{1}{4\pi\epsilon_0} \int \frac{\rho(\mathbf{r}', t')}{|\mathbf{r} - \mathbf{r}'|} d\mathbf{r}' + \frac{1}{4\pi\epsilon_0} \int \frac{\sigma_s(\mathbf{r}', t')}{|\mathbf{r} - \mathbf{r}'|} ds'. \quad (83)$$

The vector potential is:

$$\begin{aligned} \mathbf{A}(\mathbf{r}, t) &= \frac{\mu_0}{4\pi} \int \frac{\mathbf{J}(\mathbf{r}', t')}{|\mathbf{r} - \mathbf{r}'|} d\mathbf{r}' + \frac{1}{4\pi\epsilon_0} \frac{\mu_0}{4\pi} \frac{\partial}{\partial t} \int \int \frac{\partial \sigma_s(\mathbf{r}'', t'')}{\partial t} \\ &\times \frac{1}{|\mathbf{r} - \mathbf{r}'|} \frac{\mathbf{r}' - \mathbf{r}''}{|\mathbf{r}' - \mathbf{r}''|^3} ds'' d\mathbf{r}', \end{aligned} \quad (84)$$

where  $t'' = t - |\mathbf{r} - \mathbf{r}''|/c$ . These are the potentials to be used for calculating  $\mathbf{E}$  and  $\mathbf{B}$  in space using equations (76) and (77).

**3.4.2. The current transport equation for NGs.** We now derive the current transport in a loop hooking an NG with an external load  $R$  (figure 25). In the external circuit of the NG from the  $A$  electrode to the  $B$  electrode, the current transport equation is:

$$\varphi_{AB} = \int_A^B \mathbf{E} \cdot d\mathbf{L} = \frac{\partial Q}{\partial t} R. \quad (85)$$

If the full solution is received from the differential equation considering the boundary conditions, the potential between the two points does not depend on the choice of path for the integral  $\mathbf{L}$ . However, since equation (83) was obtained by ignoring the volume occupied by the dielectric media, it can be adopted for calculating the potential distribution in each of the media, from which the local electric field is derived  $\mathbf{E} = -\nabla\varphi$ . Then the potential drop between the two electrodes is obtained by a path integral  $\varphi_{AB} = \int_A^B \mathbf{E} \cdot d\mathbf{L}$ . This approximated result should fit the experimental data well. We now use the following two examples to illustrate this approach.

**3.4.3. The output of piezoelectric NGs.** Figure 27(a) shows a thin film-based PENG, which is an insulator piezoelectric material covered by two flat electrodes on its two surfaces. Once the NG is compressed by a vertical force, piezoelectric polarization charges are generated at the two ends of the material. The polarization charge density  $\sigma_p$  can be increased by increasing the applied force, and the electrostatic potential created by the polarization charges is balanced by the flow of electrons between two electrodes through a load. If the induced charge density on the electrode is  $\sigma(t)$ , the corresponding

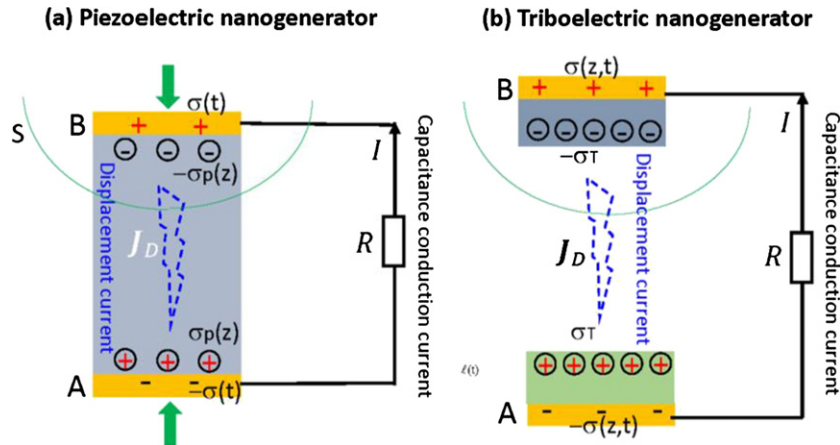


**Figure 27.** (a) Thin film-based PENGs and (b) CS mode TENGs.

electric field in the media is:

$$E = \sigma - \sigma_p / \varepsilon. \quad (86)$$

Substituting equation (86) into equation (85), the transport equation is:

$$RA \frac{d\sigma}{dt} + z \frac{\sigma - \sigma_p}{\varepsilon} = 0, \quad (87)$$

where  $A$  is the area of the electrode, and  $z$  is the thickness of the piezoelectric film. If the thickness variation of the piezoelectric film is ignored and the edge effect is ignored, equation (87) has a general solution:

$$\sigma = \sigma_p \left[ 1 - \exp \left( -\frac{z}{RA\varepsilon} t \right) \right]. \quad (88)$$

Therefore, the output power on the load is:

$$p = \left[ \frac{z\sigma_p}{RA\varepsilon} \exp \left( -\frac{z}{RA\varepsilon} t \right) \right]^2 R. \quad (89)$$

**3.4.4. The output of triboelectric NGs.** To illustrate the applications of the theory presented above for TENG, we choose the CS mode as a simple case (figure 27(b)). The TENG is made of two dielectric layers separated by a gap, with electrodes on the top and bottom surfaces of the two dielectric layers, respectively. For the TENG, electrostatic charges with opposite signs are generated on the surfaces of two dielectrics after the physical contact. If the two dielectrics have permittivity of  $\varepsilon_1$  and  $\varepsilon_2$  and thicknesses of  $d_1$  and  $d_2$ , respectively, the triboelectricity introduced surface charge density is  $\sigma_T(t)$ , and the density of free electrons on surfaces of the electrode is  $\sigma(z, t)$ . By assuming the planar size of the dielectric film is much larger than the gap distance, and ignoring the field leakage effect at the edge, the electric fields in the two media and in the gap are respectively:

$$E_{z1} = -\sigma(z, t) / \varepsilon_1, \quad (90a)$$

$$E_{z2} = -\sigma(z, t) / \varepsilon_2, \quad (90b)$$

$$E_{z3} = -(\sigma(z, t) - \sigma_T) / \varepsilon_0. \quad (90c)$$

The potential drop between the  $A$  and  $B$  electrodes is:

$$\varphi_{AB} = -\sigma(z, t)[d_1/\varepsilon_1 + d_2/\varepsilon_2] - H(t)[\sigma(z, t) - \sigma_T]/\varepsilon_0. \quad (91)$$

The transport equation across an external load  $R$  is thus:

$$\frac{\partial \sigma(z, t)}{\partial t} = -\sigma(z, t) \frac{d_1/\varepsilon_1 + d_2/\varepsilon_2 + H(t)/\varepsilon_0}{RA} + \frac{H(t)\sigma_T}{RA\varepsilon_0}. \quad (92)$$

$H$  is a function of time and it is determined by the rate at which the two dielectrics are contacted. This is a general transport equation that can be solved analytically and numerically.

#### 3.4.5. Electric potential for contact-separation mode TENG.

The CS mode TENG is based on a physical contact between two dielectric films with distinct electron affinity (at least one is an insulator) (figure 28(a)) [91]. The contact of the two creates opposite triboelectric charges at their surfaces, respectively. Once the two surfaces are separated by a gap, a potential drop is created between electrodes deposited on the top and the bottom surfaces of the two dielectric films. If the two electrodes are electrically connected through a load, free electrons in one electrode would flow to the other electrode in order to balance the electrostatic field. Once the gap is closed, the potential drop created by the triboelectric charges disappears, and the induced electrons will flow back. A periodic contact and separation between the two materials drives the induced electrons to flow back and forth between the two electrodes, resulting in an AC output in the external circuit. We now use equation (83) to calculate the potential distribution in space for the CS mode TENG. By assuming that the electrode is a thin film and the charges are distributed on the surface [28]:

$$\varphi(\mathbf{r}, t) = \frac{1}{4\pi\varepsilon} \int \frac{\sigma(\mathbf{r}', t) + \sigma_T(\mathbf{r}', t')}{|\mathbf{r} - \mathbf{r}'|} d\mathbf{s}'. \quad (93)$$

We can easily write down the current density for a plate with width  $W$  and length  $L$  in the CS mode TENG (figure 28(a)):

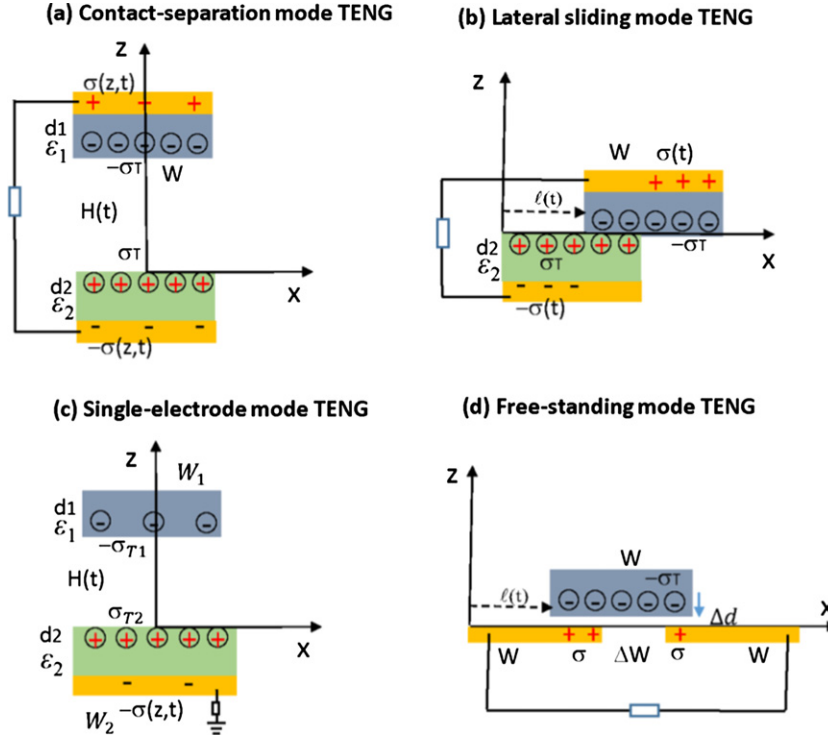


**Figure 28.** Coordination system and mathematical parameters defined for describing (a) CS, (b) lateral-sliding mode, (c) single-electrode mode and (d) free-standing mode TENGs, respectively.

$$\sigma(\mathbf{r}, t) \approx \begin{cases} -\sigma\delta(z + d_2) & \text{if } -\frac{W}{2} \leq x \leq \frac{W}{2} \text{ and } -\frac{L}{2} \leq y \leq \frac{L}{2}; \\ \sigma\delta(z - H(t) - d_1) - \frac{W}{2} & \leq x \leq \frac{W}{2} \text{ and } -\frac{L}{2} \leq y \leq \frac{L}{2}; \\ 0, & \text{otherwise.} \end{cases} \quad (94a)$$

$$\sigma_T(\mathbf{r}, t) = \begin{cases} \sigma_T\delta(z), & \text{if } -\frac{W}{2} \leq x \leq \frac{W}{2} \text{ and } -\frac{L}{2} \leq y \leq \frac{L}{2}; \\ -\sigma_T\delta(z - H(t)), & \text{if } -\frac{W}{2} \leq x \leq \frac{W}{2} \text{ and } -\frac{L}{2} \leq y \leq \frac{L}{2}; \\ 0, & \text{otherwise.} \end{cases} \quad (94b)$$

**3.4.6. Electric potential for lateral-sliding mode TENG.** The lateral-sliding mode TENG is based on contacted sliding between two dielectric surfaces (figure 28(b)). When two materials with opposite triboelectric polarities are brought into contact, surface charge transfer occurs owing to the CE effect [92]. When the two surfaces are fully matched there is no current flow, because the positive charges at one side are fully compensated by the negative ones. Once a relative displacement is introduced by an externally applied force in the direction parallel to the interface, triboelectric charges are not fully compensated at the displaced/mismatched areas, resulting in the creation of an effective dipole polarization in parallel to the direction of the displacement. Therefore, a potential difference across the two electrodes is generated. For the lateral-sliding mode TENG, we can easily write down the current density for

a plate with width  $W$  (sliding direction) and length  $L$ , with a sliding distance of  $\ell(t)$  ( $\ell(t) \leq W$ ) (figure 28(b)):

$$\sigma(\mathbf{r}, t) = \begin{cases} -\sigma\delta(z + d_2), & \text{if } 0 \leq x \leq \ell(t) \text{ and } -\frac{L}{2} \leq y \leq \frac{L}{2}; \\ \sigma\delta(z - d_1), & \text{if } w \leq x \leq \ell(t) + w, \text{ and } -\frac{L}{2} \leq y \leq \frac{L}{2}; \\ 0, & \text{otherwise.} \end{cases} \quad (95a)$$

$$\sigma_T(\mathbf{r}, t) = \begin{cases} \sigma_T\delta(z), & \text{if } 0 \leq x \leq \ell(t) \text{ and } -\frac{L}{2} \leq y \leq \frac{L}{2}; \\ -\sigma_T\delta(z), & \text{if } w \leq x \leq \ell(t) + w, \text{ and } -\frac{L}{2} \leq y \leq \frac{L}{2}; \\ 0, & \text{otherwise.} \end{cases} \quad (95b)$$

**3.4.7. Electric potential for single-electrode mode TENG.** The single-electrode mode TENG is most useful for detecting the motion of a freely unattached object. For a dielectric and metal plate, as shown in figure 28(c) [93], an induction current is created in the metal plate if the charged dielectric approaches it to balance the field. Once the dielectric moves away from the metal plate, the current flows back to the ground. This mode is most useful for utilizing the energy from a moving object without attaching a wire, such as human walking, moving car, finger typing and more. If we ignore the edge effect and assume the gap distance is much smaller than the size of the dielectric layer, the distribution of charges on the surfaces are:

$$\sigma(\mathbf{r}, t) \approx \begin{cases} -\sigma\delta(z + d_2) & \text{if } -\frac{W_2}{2} \leq x \leq \frac{W_2}{2} \text{ and } -\frac{L}{2} \leq y \leq \frac{L}{2}; \\ 0, & \text{otherwise.} \end{cases} \quad (96a)$$

$$\sigma_T(\mathbf{r}, t) = \begin{cases} \sigma_{T2}\delta(z), & \text{if } -\frac{W_2}{2} \leq x \leq \frac{W_2}{2} \text{ and } -\frac{L}{2} \leq y \leq \frac{L}{2}; \\ -\sigma_{T1}\delta(z - H(t)), & \text{if } -\frac{W_1}{2} \leq x \leq \frac{W_1}{2} \text{ and } -\frac{L}{2} \leq y \leq \frac{L}{2}; \\ 0, & \text{otherwise.} \end{cases} \quad (96b)$$

**3.4.8. Electric potential for free-standing mode TENG.** The free-standing mode TENG is introduced to minimize the friction between the two dielectrics. If we make a pair of symmetric electrodes underneath a dielectric layer and the sizes of the electrodes are of the same order as the size of the moving object, and there is a small gap between the object and the electrode, the object approaching and/or departing from the electrodes creates an asymmetric charge distribution via induction in the media, provided the object was prior-charged by a triboelectric process, which causes the electrons to flow between the two electrodes to balance the local potential distribution (figure 28(d)) [94]. The oscillation of the electrons between the paired electrodes in responding to the back and forth motion of the object produces an AC current output. This mode carries the advantages of harvesting energy from a moving object but with the entire system mobile without grounding. If the gap between the top dielectric and the bottom electrodes is  $\Delta d$  and assuming the gap is rather small so that we can ignore the edge effect, the charge distribution is:

$$\sigma(\mathbf{r}, t) = \begin{cases} \sigma\delta(z), & \text{if } \ell(t) \leq x \leq w \text{ and } -\frac{L}{2} \leq y \leq \frac{L}{2}; \\ \sigma\delta(z), & \text{if } w + \Delta w \leq x \leq \ell(t) + w, \text{ and } -\frac{L}{2} \leq y \leq \frac{L}{2}; \\ 0, & \text{otherwise.} \end{cases} \quad (97a)$$

$$\sigma_T(\mathbf{r}, t) = \begin{cases} -\sigma_T\delta(z - \Delta d), & \text{if } \ell(t) \leq x \leq \ell(t) + w \text{ and } -\frac{L}{2} \leq y \leq \frac{L}{2}; \\ 0, & \text{otherwise.} \end{cases} \quad (97b)$$

The transport behavior of the TENG is seen by calculating the potential drop between the two electrodes using equation (93) and then substituting it into equation (85) and solving it numerically.

### 3.5. Extension of Maxwell's displacement current for magnetic materials

If the electrode materials or dielectric media are magnetic, the magnetic induction and magnetic field are related by:

$$\mathbf{B} = \mu_0(\mathbf{H} + \mathbf{M}), \quad (98)$$

where  $\varepsilon_0$ ,  $\varepsilon$ ,  $\mu_0$  and  $\mu$  is the vacuum dielectric constant, dielectric constant, vacuum permeability and ferromagnetic permeability, respectively. We have:

$$\nabla \times \mathbf{B} = \mu_0(\nabla \times \mathbf{H} + \nabla \times \mathbf{M}). \quad (99)$$

Starting from the Ampere's law in the Maxwell's equations, equation (25),

$$\nabla \times \mathbf{B} = \mu_0 \left( \mathbf{J} + \frac{\partial \mathbf{D}'}{\partial t} + \frac{\partial \mathbf{P}_s}{\partial t} \right) + \mu_0 \nabla \times \mathbf{M} \quad (100a)$$

$$\nabla \times \mathbf{B} = \mu_0 \mathbf{J} + \mu_0 \frac{\partial \mathbf{D}'}{\partial t} + \mu_0 \left( \frac{\partial \mathbf{P}_s}{\partial t} + \nabla \times \mathbf{M} \right), \quad (100b)$$

where the terms related to the output of TENG can be expressed as:

$$\mathbf{J}_D = \frac{\partial \mathbf{D}'}{\partial t} + \frac{\partial \mathbf{P}_s}{\partial t} + \nabla \times \mathbf{M}. \quad (101)$$

This is a generalized displacement current by including the space variation of magnetization in theoretical calculation. Therefore, the displacement has three types: the current due to time variation of electric field rather than charge flow, which is responsible for the transmission of electromagnetic wave, first proposed by Maxwell; the ‘passing-by’ flow of the charged medium boundaries due to external mechanical agitation, first proposed by Wang; and the curl of the magnetization. Such definition in equation (101) expands the scope of the Maxwell's displacement current.

### 3.6. Technology perspectives from the expanded Maxwell's displacement current

From the expanded Maxwell's displacement current in equation (28), the first component of displacement current  $\varepsilon \partial \mathbf{E} / \partial t$  originally proposed by Maxwell gives the birth of EM wave, and the EM induction causes the emergence of antenna, radio, telegram, TV, radar, microwave, wireless communication, and space technology from 1886 (left-hand side in figure 29). The most important applications of Maxwell's equations in the last century are about waves, such as light and EM wave. It was Maxwell who inspired Einstein to start the work of unifying the four forces in nature: electromagnetism, weak interaction, strong interaction and gravity, and the original idea of gravitation waves. Therefore, the first component of the displacement current has driven the development of the world in communication and laser technology in the last century.

In parallel, the second term  $\partial \mathbf{P}_s / \partial t$  in equation (27), which is referred to as the Wang term by including polarization arising from a change in medium shape and distribution as triggered by external force in the displacement current, sets the foundation for the NGs. NGs are referred to as the energy for the new era—the era of the internet of things and sensor networks [29, 85, 95]. Adding the term of  $\partial \mathbf{P}_s / \partial t$  in the displacement current and thus in Maxwell's equations extends their applications to energy (right-hand side in figure 29). The  $\partial \mathbf{P}_s / \partial t$  term is the driving force inside the NG, while the term  $\mathbf{J}$  is the conduction current density observed across the external load. NGs for energy could have extensive applications in the internet of things, sensor networks and blue energy, which will impact the world for the future. The NGs could be regarded

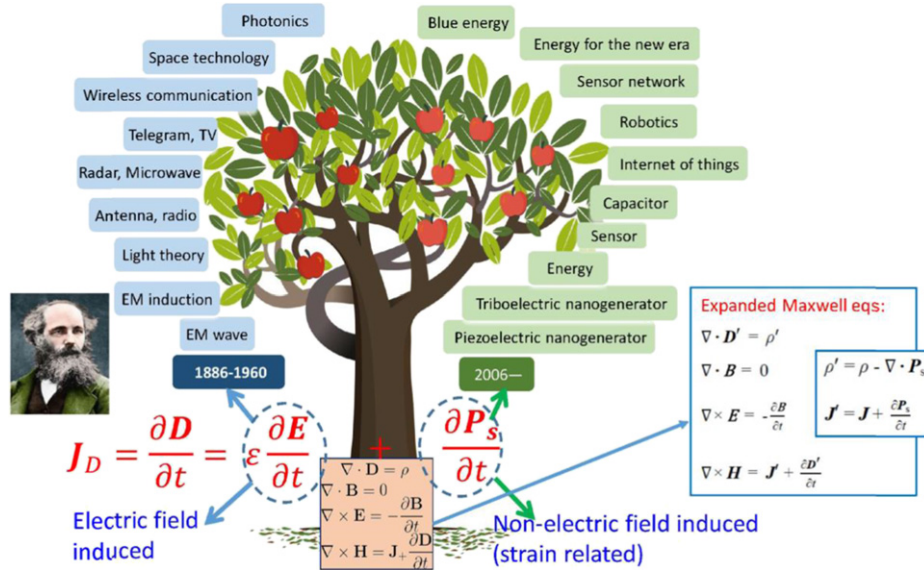


**Figure 29.** A tree idea to illustrate the newly expanded Maxwell's displacement current: the first term  $\varepsilon \partial \mathbf{E} / \partial t$  is responsible for the EM waves theory, and the newly added term due to  $\partial \mathbf{P}_s / \partial t$  is the applications of Maxwell's equations in energy and sensors, which are the NGs.

as another important application of Maxwell's equations in energy and sensors after the EM wave theory and technology. For the foreseeable future, the ‘tree’ idea presented in figure 29 is expected to grow stronger, taller and larger, which possibly leads to technological breakthroughs that are expected to impact human society at large.

A question here is why Maxwell missed the term  $\partial \mathbf{P}_s / \partial t$  in the original equation? A possible reason is that he was entirely focused on the theory of electromagnetic waves of fixed medium boundaries without considering the impact of external factor such as applied force. Traditionally, electromagnetic wave related communication and theory of light rarely have the case of moving/varying boundary. However, such case is changed for mechanical energy conversion, which gives us an opportunity for adding this term in the Maxwell's equations.

It is known that the waves associated with Maxwell's displacement current ( $\varepsilon \partial \mathbf{E} / \partial t$ ) are at high frequency in the range of GHz and above, while the NGs governed by  $\partial \mathbf{P}_s / \partial t$  usually work in the low-frequency range, so that the two have little coupling in a general sense. However, with the increase of mechanical triggering frequency possibly in the future, the two terms of  $\varepsilon \partial \mathbf{E} / \partial t$  and  $\partial \mathbf{P}_s / \partial t$  could be coupled. The expanded Maxwell's equations include such effects in general.

#### 4. Fundamentals of triboelectric NGs

##### 4.1. Theoretical modeling

As for TENG, equation (74) has been applied to calculate the power output for CS mode, [96] lateral-sliding mode [97–99], single-electrode mode [99] and free standing mode [100, 101]. A general review on such calculations has been given by Niu and Wang [102]. Recently, using the distance-dependent model and starting from the displacement current, Shao *et al* have calculated the structure figure-of-merits (FOMs) for TENG [103]. Furthermore, numerical calculations

have been done for single-electrode mode for 3D configuration [104]. Dharmasena *et al* [105] have simulated more complex geometry and results have been compared with experiments. We now use some examples to illustrate some progress made in numerical calculations for TENG.

**4.1.1. Current transport dynamics in TENGs.** The finite-sized charged planes (FSCP) model, also called the three-dimensional (3D) mathematical model, is a unified and versatile theoretical model for TENG [102, 104]. Different from the capacitance (CA) model built through the circuit theory, the 3D mathematical model was developed based on the theory of electrodynamics [106, 107]. This model can be used not only to describe the basic working principles of TENGs, but also to explain the physical mechanisms, such as the change of displacement current and the energy in dielectric systems, which may provide insights that could be utilized in the design and construction of more efficient TENG devices toward future applications. As shown in figure 30(a), we assume that there is a set of charged finite-sized planes, with the same geometric dimensions  $a$  and  $b$  along the  $x$  and  $y$  directions, respectively. These planes are all centered at  $(x, y) = (0, 0)$  and located at positions  $z_1, \dots, z_N$  with surface charges  $\sigma_1, \dots, \sigma_N$ , respectively. The electric potential at an arbitrary point  $\mathbf{r} = (x, y, z)$  can be evaluated analytically [104]:

$$\varphi(x, y, z) = \sum_{i=1}^N \frac{\sigma_i}{4\pi\varepsilon(r)} \int_{-a/2}^{a/2} \int_{-b/2}^{b/2} \times \frac{dx' dy'}{\sqrt{(x - x')^2 + (y - y')^2 + (z - z_i)^2}}. \quad (102)$$

From equation (102), the relevant electric field at specific locations can be calculated by:

$$\mathbf{E}(x, y, z) = -\nabla \varphi = \sum_{i=1}^N \frac{\sigma_i}{4\pi\varepsilon(r)} \int_{-a/2}^{a/2} \int_{-b/2}^{b/2} \times \frac{dx' dy'}{(x-x')^2 + (y-y')^2 + (z-z_i)^2} \times \frac{(x-x', y-y', z-z_i)}{\sqrt{(x-x')^2 + (y-y')^2 + (z-z_i)^2}}. \quad (103)$$

To properly account for the effect of boundary conditions in the calculation, the local electric potential can be calculated using a path integral of the electric field given by equation (103) following equation (85) and the discussion presented in section 3.3.2. Considering a CS mode TENG shown in figure 30(b), where the integral path is chosen along the  $z$  axis, the electric potentials at  $z = z_4$  and  $z = z_1$  are given respectively by:

$$\varphi_1(0, 0, z_4) = -\frac{\sigma}{\pi\varepsilon_2} \int_{z_4-z_1}^{\infty} f(z') dz' + \frac{\sigma}{\pi\varepsilon_2} \int_0^{\infty} f(z') dz' + \frac{\sigma_T}{\pi\varepsilon_2} \int_{z_4-z_2}^{\infty} f(z') dz' - \frac{\sigma_T}{\pi\varepsilon_2} \int_{z_4-z_3}^{\infty} f(z') dz' \quad (104a)$$

$$\varphi_2(0, 0, z_1) = -\frac{\sigma}{\pi\varepsilon_1} \int_0^{\infty} f(z') dz' + \frac{\sigma}{\pi\varepsilon_1} \int_{z_1-z_4}^{\infty} f(z') dz' + \frac{\sigma_T}{\pi\varepsilon_1} \int_{z_1-z_2}^{\infty} f(z') dz' - \frac{\sigma_T}{\pi\varepsilon_1} \int_{z_1-z_3}^{\infty} f(z') dz' \quad (104b)$$

$$f(z) = \arctan \left\{ ab / \left[ 4z \sqrt{\left(\frac{a}{2}\right)^2 + \left(\frac{b}{2}\right)^2 + (z)^2} \right] \right\}, \quad (105)$$

where  $a$  and  $b$  represent the geometric dimensions of the electrode, respectively, and  $z$  is the contact separation distance along the  $z$  direction. When a resistance  $R$  is connected between the two electrodes, according to equation (85), the potential drop over  $R$  is:

$$-RA \frac{d\sigma}{dt} = \varphi_1(0, 0, z_4) - \varphi_2(0, 0, z_1) = \frac{\sigma}{\pi\varepsilon_2} \int_0^{z_4-z_1} f(z') dz' + \frac{\sigma_T}{\pi\varepsilon_2} \int_{z_4-z_2}^{z_4-z_3} f(z') dz' + \frac{\sigma}{\pi\varepsilon_1} \int_0^{z_1-z_4} f(z') dz' + \frac{\sigma_T}{\pi\varepsilon_1} \int_{z_1-z_3}^{z_1-z_2} f(z') dz', \quad (106)$$

where  $A$  is the electrode area, and  $\sigma(t)$  stands for the charge density on the electrode. This is a time-dependent differential equation, from which  $\sigma_u(t)$  can be fully specified. At OC conditions, no charges are transferred between the two electrodes, and the OC voltage ( $V_{OC}$ ) becomes:

$$-V_{OC} = \varphi_{AB}(0, 0, z_4) - \varphi_{AB}(0, 0, z_1) = \frac{\sigma_T}{\pi\varepsilon_2} \int_{z_4-z_2}^{z_4-z_3} f(z') dz' + \frac{\sigma_T}{\pi\varepsilon_1} \int_{z_1-z_3}^{z_1-z_2} f(z') dz'. \quad (107)$$

If  $V_{OC}$  is equal to zero, or at SC conditions, the current is given by:

$$I_{SC} = A \frac{d\sigma^{SC}}{dt}, \quad (108)$$

where  $\sigma^{SC}$  is the electrode charge density at SC. The latter is found from equation (106) by setting the electrical resistance  $R$  equal to zero (zero voltage):

$$\sigma^{SC} = \frac{\sigma_T \left[ \frac{1}{\varepsilon_2} \int_{z_4-z_3}^{z_4-z_2} f(z') dz' + \frac{1}{\varepsilon_1} \int_{z_1-z_2}^{z_1-z_3} f(z') dz' \right]}{\frac{1}{\varepsilon_1} \int_{z_1-z_4}^{z_1-z_2} f(z') dz' + \frac{1}{\varepsilon_2} \int_0^{z_4-z_1} f(z') dz'}. \quad (109)$$

From equation (109), the SC transferred charges  $Q_{SC}$  can be obtained by  $A\sigma^{SC}$ .

Numerical calculations of the above equations are depicted in figures 30(d)–(g). In figure 30(d), the temporal values of  $V_{OC}$  are plotted using the present finite-sized charged plane model vs the results of the distance dependent electric field model and CA model. As shown in figure 30(e), the peak values of the OC voltage are plotted vs the maximum air-gap thickness for the three models. It can be found that the 3D model and the distance-dependent electric field model are in exact agreement with the simpler CA model [105, 108]. The  $V_{OC}$  values as a functions of time are considerably larger for the CA model when compared to the two other models. In particular, we can see the same phenomenon from the  $Q_{SC}$  and  $I_{SC}$  shown in figures 30(f) and (g). The reason for this is because the edge effects of TENGs have not been considered in the CA model.

In a TENG's charging system, in which a capacitor acts as the energy storage unit, the magnitude of the  $I_D$  is proportional to the rate at which the voltage ( $V^C$ ) across the loaded capacitor varies in time, that is [104]:

$$I_D = I = C_L \frac{dV^C}{dt}, \quad (110)$$

where the  $C_L$  represents a connected capacitor. Figure 31 demonstrates the displacement current–time relationship for the four basic modes of TENGs with different  $C_L$ . We further note that a current peak exists for all the external  $C_L$ , and a larger  $C_L$  leads to a bigger maximum  $I_D$  for all the modes of TENGs.

**4.1.2. Maxwell's displacement current.** The Maxwell's displacement current ( $I_D$ ) is the driving force for a TENG, through which the mechanical energy can be effectively converted into electric power/signal. Based on the schematic of the LS mode TENG, the displacement current–time relationship at SC conditions is demonstrated in figure 32(a). Figure 32(b) illustrates a comparison of the SC current ( $I_{SC}$ ) from the calculations of the 3D model and CA model [104]. It is apparent that the variation of  $I_{D,SC}$  is identical to that of the  $I_{SC}$ . More importantly, the magnitude of  $I_D$  at OC conditions ( $I_{D,OC}$ ) is

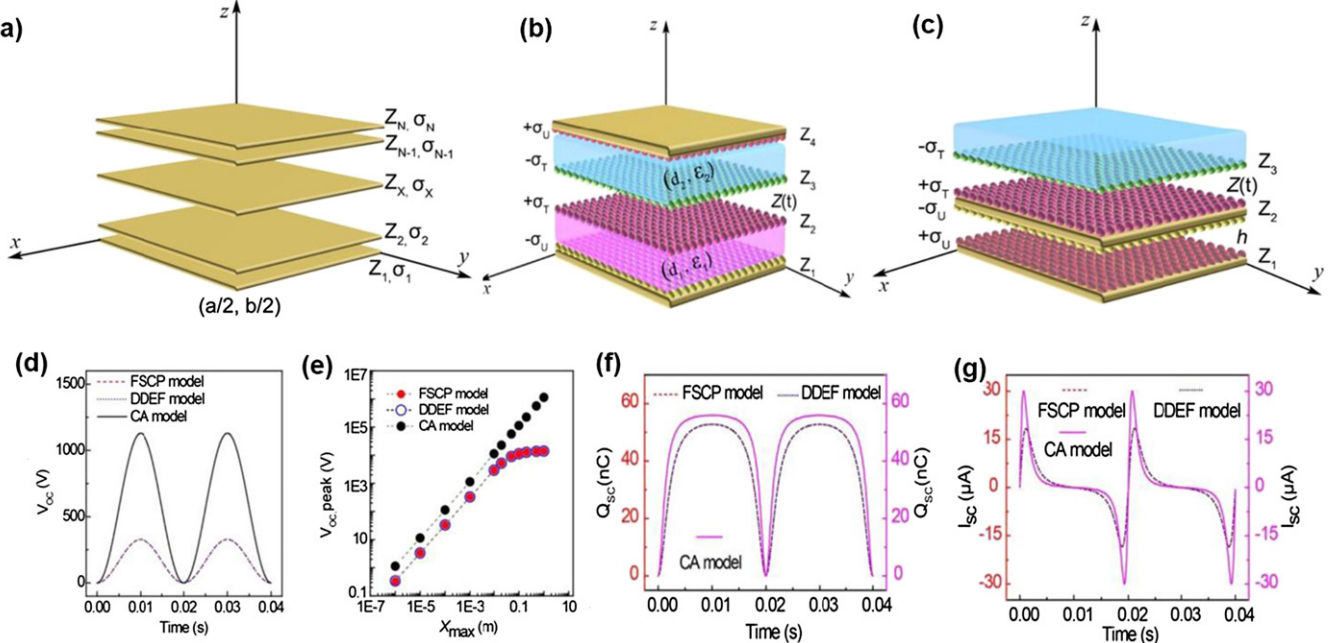


**Figure 30.** 3D mathematical model and the basic outputs of the CS mode TENG. (a) Schematic model of the  $N$  finite sized planes located at positions  $z_1, \dots, z_N$  with surface charge densities  $\sigma_1, \dots, \sigma_N$ , constructed in the Cartesian coordinate system. (b) and (c) Schematic of a typical CS mode TENG and a single electrode (SEC) mode TENG in the Cartesian coordinate system. (d) Comparison of the potential difference at OC conditions from the FSCP model, the distance-dependent electric field model and the CA model [106]. (e) Comparison of the peak  $V_{OC}$  for different  $x_{\max}$  from the three different models. (f) Comparison of the transferred charges ( $Q_{SC}$ ) and (g) SC current ( $I_{SC}$ ) from the three different models at SC conditions. Reprinted from [104], Copyright (2019), with permission from Elsevier.

equal to  $I_{D,SC}$ , but it displays a phase change. The electric field at the  $z_1$  position (fixed electrode) and the relevant  $I_D$  vs time at  $Z_{\text{opt}}$  are demonstrated in figures 32(d) and (e), respectively. We notice that both signals are always parallel but change with opposite phase. This is because the generation of the  $I_D$  is due to the change rate of the electric field. A comparison between the electric field at the  $z_1$  and  $z_2$  positions is illustrated in figure 32(f). It can be found that the variation of the electric fields displays the same phase both for the relaxation state and steady state, but clearly with different magnitudes. The reason is that the electric field contribution from charges at the top electrode is screened by the distribution of free charges at the bottom dielectric–electrode interface, then leading to a different magnitude of the electric field. Simulations using the displacement current theory have provided an optimization about the geometrical choices and spatial layout of TENG for achieving the maximized output power density [109]. A recent review about the details of the numerical calculation has been given by Shao *et al* [110].

#### 4.2. Figure of merits

FOMs are the standard to compare the performance of a specific type of technology. A solar cell is measured by its efficiency measured under one full Sun radiation disregarding the cost and lifetime for scientific purposes. Thermal electric materials are characterized by the ZT factor that is a constrained result among the thermal conductivity, electric conductivity and Seebeck coefficient. To better compare the output performance of TENGs in terms of various structures/modes,

establishing a universal standard method is of prime importance to quantitatively evaluate the performance of the TENG. Triggered by a periodic mechanical motion, the output electrical signals of TENG are periodically time-dependent. Thus, the output energy per cycle can be represented by the plot of built-up voltage vs transferred charges ( $V-Q$ ). Since the total cycling charges  $Q_c$  is always smaller than the maximum transferred charges  $Q_{SC,\max}$ , Zi *et al* [112] introduces a switch parallel connecting with an external load to enable  $Q_c = Q_{SC,\max}$  at instantaneous SC conditions to achieve cycles for maximized energy output (CMEO). As shown in figure 33(a), the maximized output energy is delivered at infinite load resistance (OC condition) forming a trapezoid shape. As proven, the operation of any kinds of TENGs are limited inside these four edges; therefore, the largest possible output energy ( $E_m$ ) per cycle can be calculated from the four edges of this trapezoid by the following equation:

$$E_m = \frac{1}{2} Q_{SC,\max} (V_{OC,\max} + V'_{\max}). \quad (111)$$

As noticed,  $Q_{SC,\max}$ ,  $V_{OC,\max}$ , and  $V'_{\max}$  (maximum achievable absolute voltage at  $Q_{SC,\max}$ ) are all in proportion to the surface charge density. Thus, the material FOM is  $\sigma^2$ , and a dimensionless structural FOM of TENG is defined as:

$$\text{FOM}_S = \frac{2\varepsilon_0}{\sigma^2} \frac{E_m}{A x_{\max}}, \quad (112)$$

where  $\sigma$  is the tribo-charge density, and  $E_m$  stands for the largest possible output energy. Accordingly, from the structure design's point of view, different working modes of TENGs,

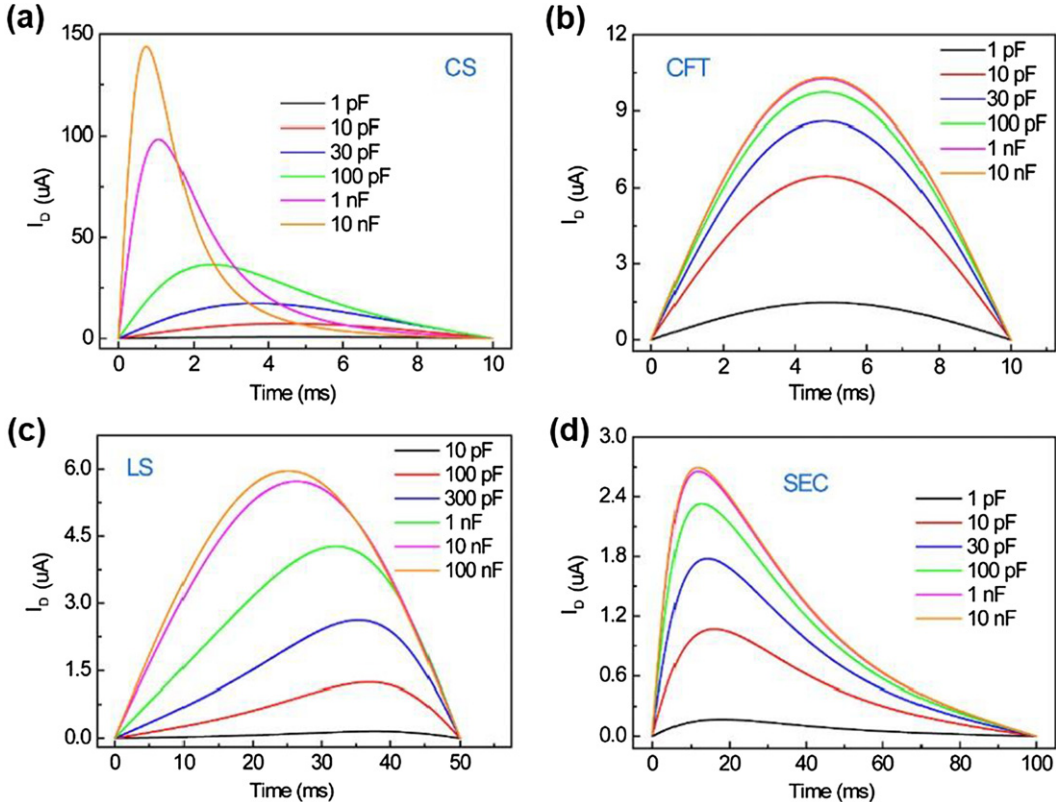


**Figure 31.** Numerical calculations of the displacement current ( $I_D$ ) in the TENG charging system.  $I_D$ -time relationships at different load CAs for (a) CS mode, (b) contact freestanding triboelectric-layer (CFT) mode, (c) lateral sliding (LS) mode and (d) single-electrode contact (SEC) mode TENGs. Note that one side edge effect of the TENGs has been considered when calculating the  $I_D$ . Reprinted from [104], Copyright (2019), with permission from Elsevier.

including CS, LS, SEC, sliding FT (SFT), and contact FT (CFT) can be calculated and simulated by FEM. Figure 33(b) shows a comparison of maximum structural FOM ( $FOM_{s, max}$ ) of different structures derived from FEM simulations, where it follows the order of CFT (6.81) > CS(0.98) > SFT(0.45) > LS(0.15) > SEC(0.022) [112]. The  $FOM_{s, max}$  can be regarded as a standard criterion to evaluate the structures of TENGs.

To sustainably power electronics using TENG, it is essential to develop an effective energy storage approach, whereas the traditional direct connection of two components is realized by a rectifier, which suffers from low energy-storage efficiency. Thus, a rational designed charging cycle is theoretically and experimentally developed by Zi *et al* [113] through introducing a motion-triggered switch in parallel connection with TENG (figure 33(c), inset is the circuit). Consequently, the charge flow in the system can be controlled through the switch so that the charging rate and improved maximum energy-storage efficiency can be enhanced up to 50%, and the saturation voltage increased by at least two-fold. As two powerful ambient mechanical energy harvesting technologies, TENGs and electromagnetic generators (EMGs) are always put forward for comparison. A systematic study was conducted by Zi *et al* [114] regarding their output performance under low-frequency motion (<5 Hz) (figure 33(d)). They pointed out that the output performance of TENG is proportional to the triggering frequency, while EMG is in proportion to the square of the frequency. Therefore, TENG is far superior to EMG at

a low frequency (0.1–3 Hz), which enables killer applications of TENGs at low frequency.

The existence of the air breakdown effect largely affects the retained charge density on the triboelectric surfaces during CS motions; thus, as the most critical limitation for output characteristics of TENGs, it is highly significant to study the air breakdown in TENGs to calculate their maximized effective energy output. Zi *et al* [115] firstly revealed a breakdown area of CS mode in the  $V$ – $Q$  plot as indicated in the negative (‘−’ region (figure 34(a)), and then experimentally verified the threshold surface charge density to be around  $40\text{--}50 \mu\text{C m}^{-2}$  for TENG under high-impedance-load working conditions. Furthermore, besides CS mode, they studied the air breakdown in CFT and SEC modes of TENG, and the  $E_m$  of each mode vs charge density taking into the of breakdown effect was plotted for comparison (figure 34(b)). Based on this fundamental study, Xia *et al* [116] proposed a universal standardized method to evaluate the real output capabilities of NGs. A circuit (inset in figure 34(c)) was developed for the measurement of breakdown limits through  $Q$ – $V$  plots (figure 34(c)), where the green arrows show the breakdown points. Through this method, the CMEO of CS mode TENG with the threshold breakdown area can be measured and the result is consistent with the theoretical calculation by Paschen’s law, as shown in figure 34(d). In addition, a CFT mode TENG and a PVDF-based PENG are also demonstrated using this approach, indicating its universal applicability for NGs. Consequently, the

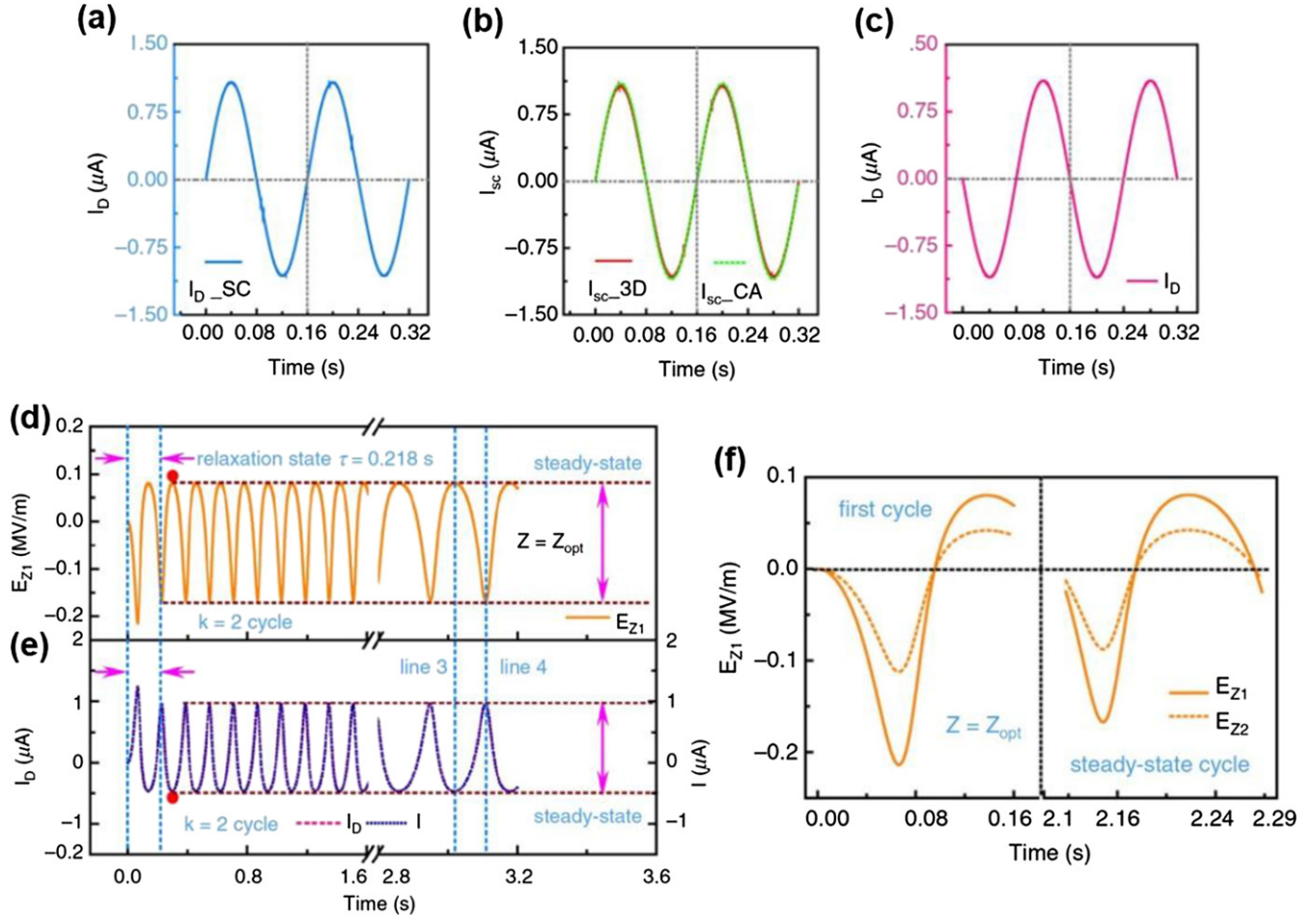


**Figure 32.** Relationship between the electric field and displacement current for the LS mode TENG. (a) Variation of the displacement current ( $I_D$ ) at SC condition. (b) Comparison of the short circuit current using the 3D model and the CA model [104, 106]. (c) Variation of the  $I_D$  at OC condition. (d) Variation of electric field at the  $z_1$  position (bottom electrode) and the corresponding (e) displacement current vs time under the optimum resistance. (g) Comparison of the electric field at the  $z_1$  and  $z_2$  positions from the first cycle to a steady state cycle at the optimum resistance. Reprinted from [111], with the permission of AIP Publishing.

structural FOM of these three modes are redefined based on the recalculated  $E_m$ , as summarized in figure 34(e). This proposed method offers a crucial standardized evaluation for the effective output capability of NGs. Furthermore, Fu *et al* [117] extended the research to the impact of breakdown effects on SFT mode TENG through theoretical simulations and experimental methods to optimize the maximal output energy density of TENG. A comparison of various modes of TENGs with other energy harvesting devices is listed in figure 34(f), where the highest output energy density is achieved by SFT mode TENG due to the suppressed breakdown effect. This study introduces an evaluation standard for the output performance of NGs and validates the killer applications of TENG for harvesting low-frequency mechanical energy.

#### 4.3. Enhancing surface charge density

**4.3.1. Choice of materials.** Choices of materials are critically important for the performance of the TENG. From our theoretical analysis, the displacement current is related to material permittivity, TECD and surface morphology (figure 35). Materials with high stability and robustness are important for

extending the lifetime of TENG for their anti-abrasion properties. The choice of permittivity is related to electrostatic induction. We anticipated that a huge amount of materials optimization remains to be carried out to enhance the performance of the TENG. This research will open a new direction for materials scientists and chemists. For example, Kwak *et al* [118] used butylated melamine formaldehyde as a promising triboelectric material for improving the mechanical durability and the triboelectric property of the friction layer. A great effort has been made to develop methodologies for enhancing the charge density on surfaces, including surface texturation [119], charge injection [120], oblique nanostructure construction [121], and charge transportation and storage along dielectric material [122].

**4.3.2. Enhancing vacuum.** Due to the existence of air breakdown, there is an upper limit for the surface charge density. The surface charge density can be effectively enhanced by operating a TENG in a higher vacuum in order to preserve the surface charge density [26]. Once operated in a pressure of  $10^{-6}$  torr, the surface charge density is enhanced up to  $1003 \mu\text{C m}^{-2}$ ,

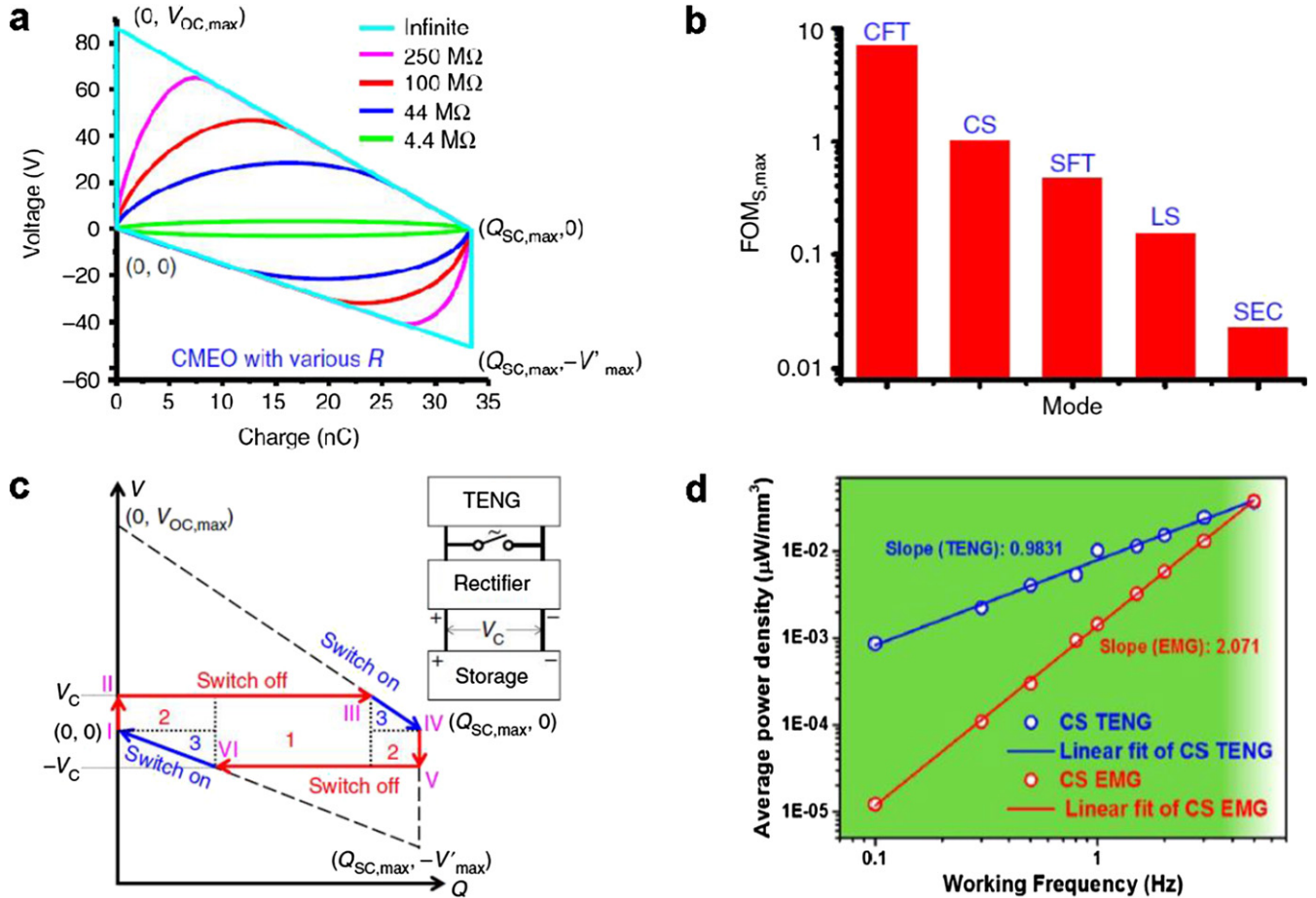


**Figure 33.** FOMs, effective energy storage, and ‘killer applications’ of the TENG. (a) Cycles of the maximized energy output (CMEO). (b) The structural FOM for various modes of TENGs. (c) The effective energy storage strategy for TENG. Reproduced from [112]. CC BY 4.0. (d) The high output of TENG compared with EM generator, demonstrating low-frequency energy harvesting as a ‘killer application’ of TENGs. [113] John Wiley & Sons. © 2016 WILEY-VCH Verlag GmbH & Co. KGaA, Weinheim.

which is about a factor of four higher than that at ambient conditions. However, maintaining a high vacuum is not practical in many cases, so this approach is not general.

**4.3.3. Charge pumps.** Since the FOM for a material is  $\sigma^2$ , enhancing the surface charge density is required for a high-performance TENG. However, the surface charge density is normally limited by the breakdown voltage of a surface, so that it is normally of the order of  $\sim 250 \mu\text{C m}^{-2}$ . Recently, a new strategy by binding charges in floating conductive layers has been developed, and the bound charges are generated using a charge pump design that can be a normal TENG, as shown in figure 36 [123, 124]. In such devices, charges are injected into the floating layer of a main TENG by the pumping TENG. The injected charges are constrained in the floating layer, which functions like static charges of normal TENGs to induce transferring of mobile charges between electrodes. The bound charges in the floating layer can be gradually accumulated until the dielectric strength of the insulation layer is reached. Thus, the pumping TENG does not need to be rubbed (or pressed) too hard owing to the time-compensation on its low output, providing a solution to the problems of abrasion and heat generation. In such a way, the effective charge density

can be greatly boosted to  $1.02 \text{ mC m}^{-2}$  in ambient conditions. The mechanism is then extended to rotary and sliding mode TENGs. Based on a synchronous rotation structure, boosted average power can be achieved in low-frequency agitations with a rotary charge-pumping TENG [125]. Improved design of the pumping idea has further increased the charge density up to  $2.38 \text{ mC m}^{-2}$  based on optimization of contact status [126] and reducing the voltage drop across rectification diodes [127]. The method should have similar importance for the development of TENGs as the electromagnets used in EM generators, which use the supplied current to generate a strong magnetic field instead of using a permanent magnet. The charge pumping mechanism provides a great possibility to surpass the limit of TENGs.

#### 4.4. Enhancing durability

**4.4.1. Auto-switching in operation modes.** As for TENGs, the most serious concern is about the robustness of the surface due to direct friction, which not only causes heat but also surface damage. In fact, different operation modes of the TENG have different degree of surface rubbing. The least rubbing is the CS mode, while the lateral-sliding mode generates serious

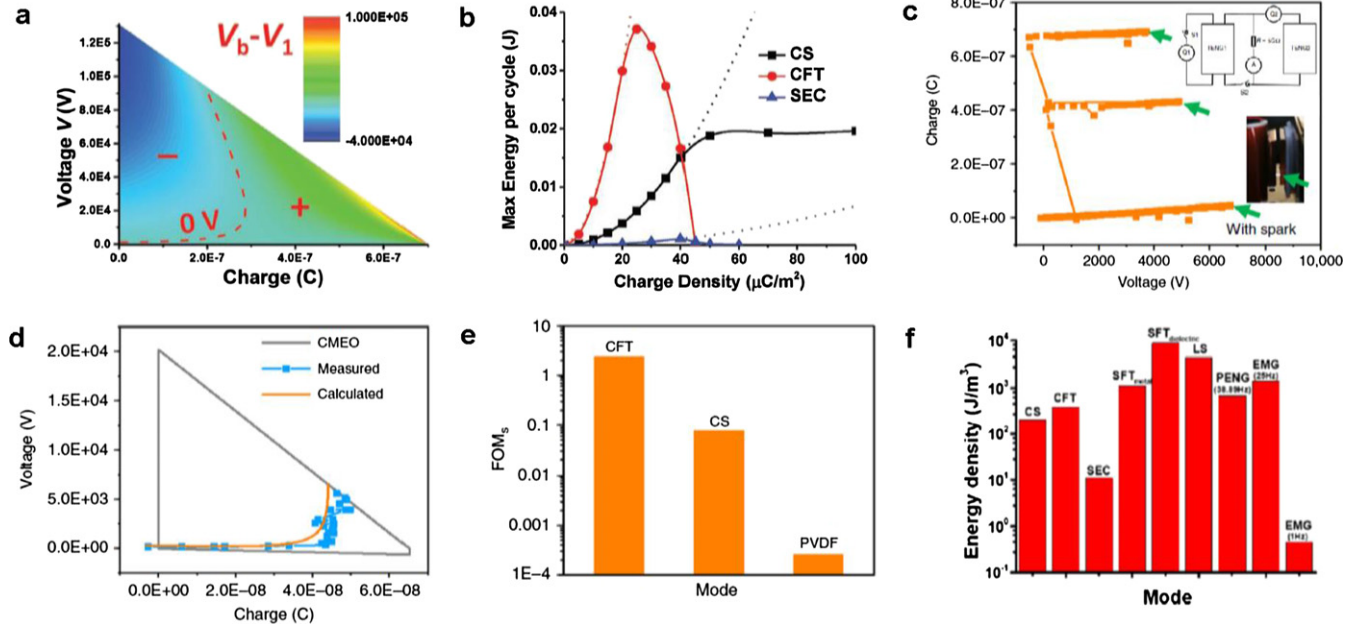


**Figure 34.** The electrical breakdown effect and the standardized evaluation of TENGs. (a) The  $V-Q$  plot of the CS TENG showing breakdown area ('-') and non-breakdown area ('+'). (b) The effective maximized energy output per cycle for CS, CFT, and SEC modes TENGs. (a) and (b) [115] John Wiley & Sons. © 2017 WILEY-VCH Verlag GmbH & Co. KGaA, Weinheim. (c) The breakdown points by simultaneously measuring voltage and charges. Insets show the measurement circuit and the picture capturing a breakdown spark. (d) The  $V-Q$  plot showing the measured and calculated breakdown points. (e) The corrected structural FOM for CFT and CS TENGs and a PVDF film PENG after considering the breakdown effect. (c)–(e) Reproduced from [116, 117]. CC BY 4.0. (f) The output energy density of various TENGs, PENG, and EMG. Reprinted with permission from [117]. Copyright (2019) American Chemical Society.

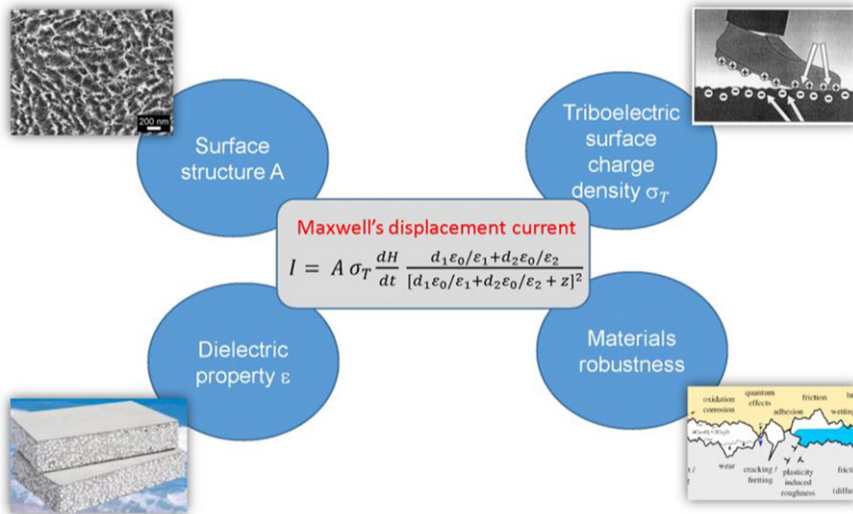


**Figure 35.** Using the theoretical result of displacement for CS mode TENG, we show here the requirements and research directions for materials in order to maximize the output of the TENG.

heat and abrasion. Considering the fact that the tribo-charges would remain on the insulator surfaces for hours in conventional conditions, a continuous rubbing between the two surfaces is unnecessary. Therefore, by a mechanical designing that allows the TENG to automatically switch between two modes depending on the rotation speed/frequency, the durability can be extensively extended. Such studies have been demonstrated by Li *et al* [128] and Lin *et al* [129]. By conjunction of the centrifugal force and the elastic of a spring, a

design has been made for auto-switching the operation mode of the TENG for achieving robust operation [129].

**4.4.2. Amplification of operation frequency.** TENGs are most effective for harvesting irregular and low-frequency energy, such as water waves. But due to the nature of the energy, the overall conversion efficiency is low due to the low frequency. We have taken two steps for enhancing the energy conversion efficiency. First, with the use of springs in the design,

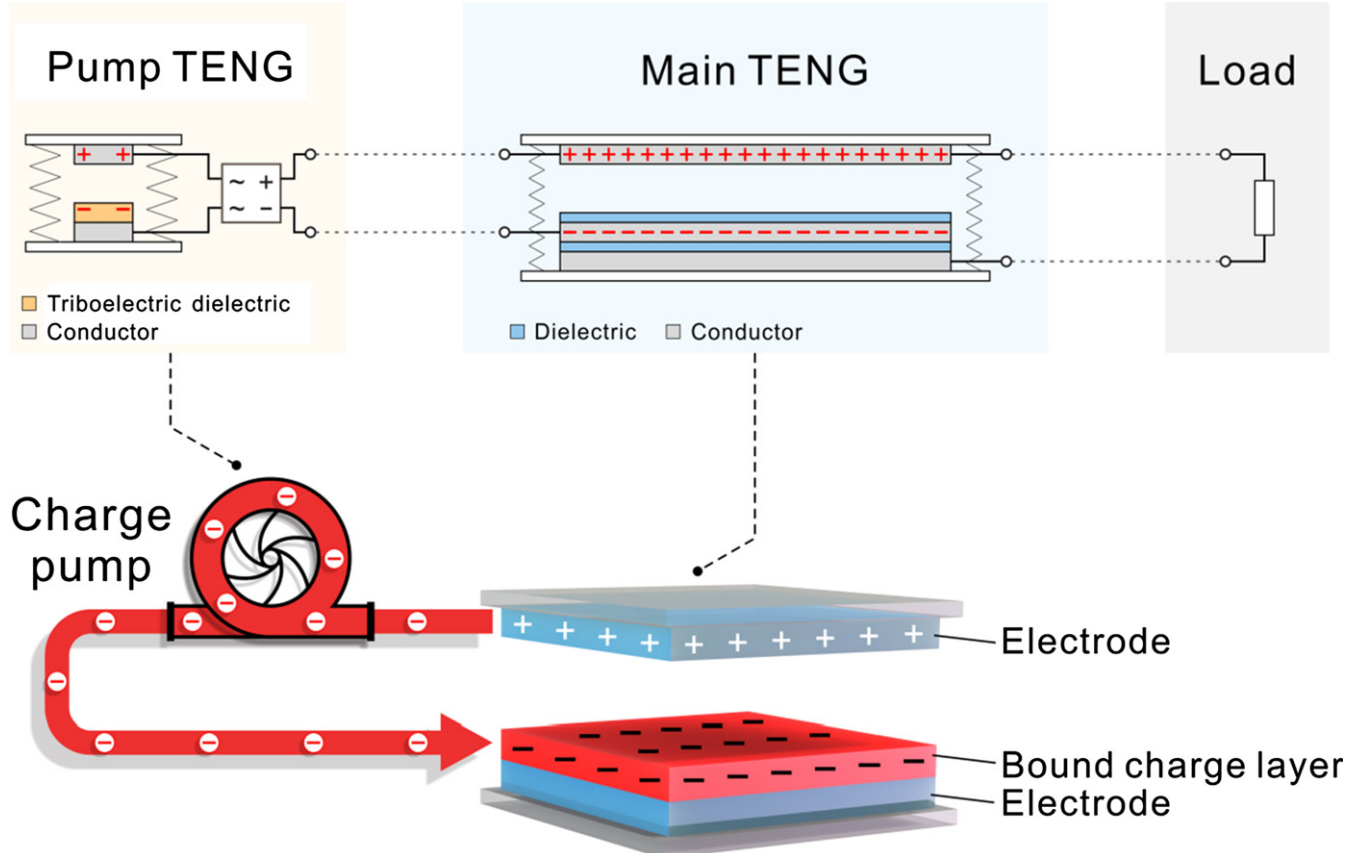


**Figure 36.** Concept of the charge-pumping TENG and the detailed structure of the device. Reprinted from [123], Copyright (2018), with permission from Elsevier.

the mechanical triggering can effectively trigger the system at mechanical resonance among the springs, so that the subsequent energy conversion at spring controlled frequency can be more effective [130]. Second, the triggering energy from the water wave can be stored as potential energy using a pendulum structure, so that an extended oscillation at a high frequency can largely enhance the energy conversion efficiency [131]. Such a design has been extended for harvesting water wave energy, and an energy conversion efficiency of over 28% has been achieved [132].

**4.4.3. Using liquid lubricant layer.** It is known that liquid lubrication is the most effective approach for reducing friction and abrasion, but coating a thin layer of oil on the solid surface could largely reduce the TE effect. Recently, by choosing an oil that has the smallest dielectric permittivity, such as squalene and paraffin oil, the performance of the lateral-sliding mode TENG is largely preserved and even improved. It is surprising to find out that proper liquid lubrication not only provides a super wear-resistant TENG, but also increases the electric output. In comparison to a slide-mode TENG with solid–solid contact, the service lifetime of the TENG can be greatly improved through liquid lubrication. Importantly, the lubricated TENG is able to give an output power that is 10 times that of the unlubricated TENG [133]. This study opens a new approach for extending the lifetime and stability of TENGs.

#### 4.5. Power management

The output of the TENG is a pulse mode where its frequency and amplitude depend on the external triggering. It also has a characteristic of high output voltage and low output current. For practical applications, it is necessary to reduce the output voltage and increase the output current, which is called the power management. Also, to make this pulsed energy useful, an energy storage unit is required for storing the harvested energy so that it can be output in a controlled and regulated manner for practical applications. Numerous approaches have been developed for effective power management at a high energy preservation efficiency [107, 134, 135].

In general, the first step is to transfer the maximum energy from the TENG to the back-end circuit based on the  $U-Q$  theory (figure 37(a)) [136–138]. When the output voltage  $U$  of the TENG reaches its peak, the switch is closed. When the energy is fully released, the switch is disconnected for the next cycle of energy storage. The maximum energy extraction efficiency of this method is 84.6% (figure 37(b)). The second step is to integrate a classic DC–DC BUCK converter to convert the TENG pulse voltage into a DC low-voltage signal (figure 37(c)). When the switch is closed, the TENG supplies power to the load and the inductance; thus, that electrical energy is stored energy. When the switch is disconnected, the current flows through the freewheel diode, and the inductor and capacitor provide energy to the load. Based on this strategy,

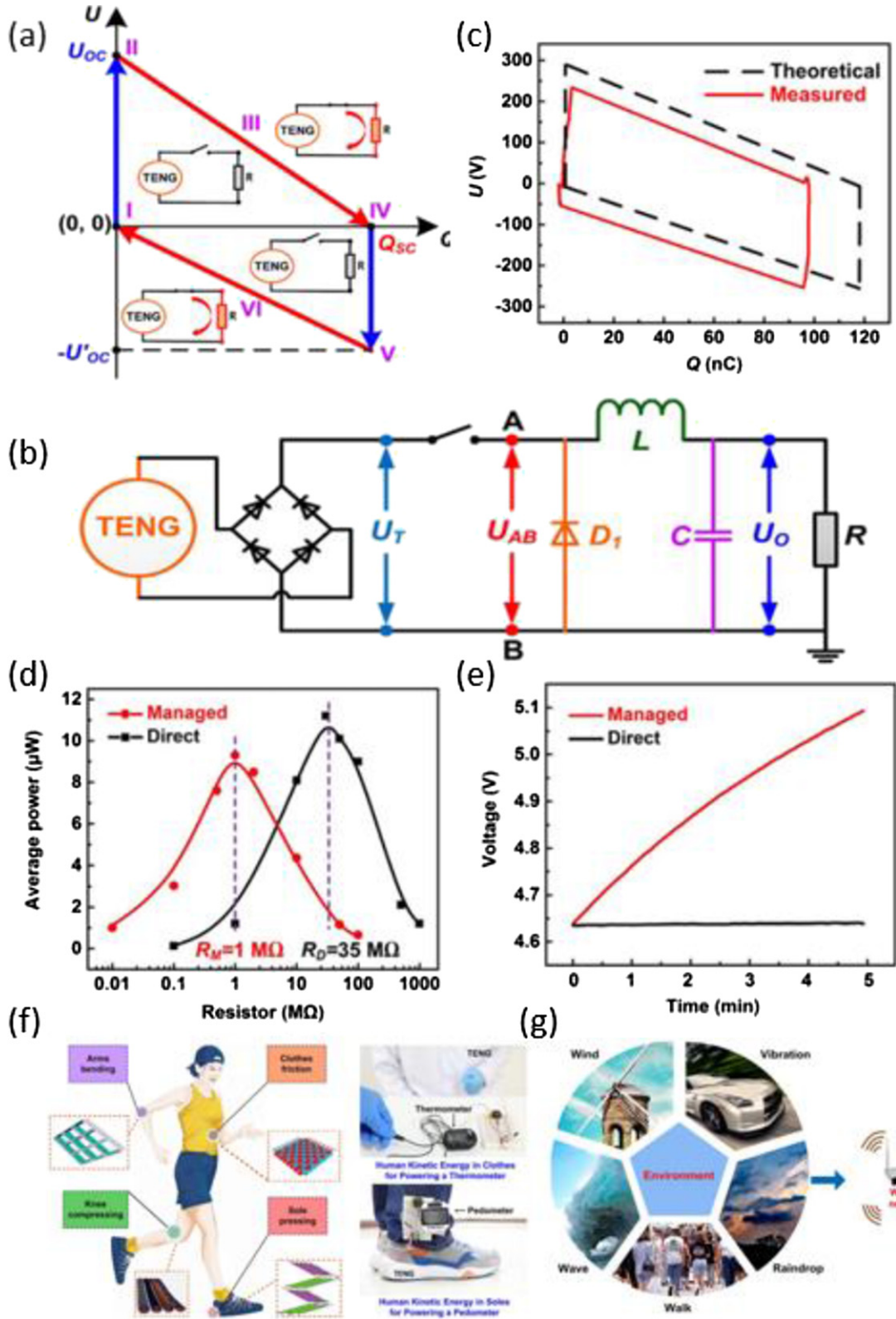


**Figure 37.** Power management strategy for TENG. (a) The voltage–charge ( $U$ – $Q$ ) plot of the TENG in the maximized energy transfer cycle. (b) The schematic circuit diagram of AC–DC buck conversion by coupling TENG, rectifier and classical DC–DC buck converter. (c) The  $U$ – $Q$  plot of the TENG with 84.6% energy transfer efficiency. (d) Comparison of the direct and managed average power on external resistors. (e) Comparison of direct and managed charging for a 1 mF CA. (f) Human kinetic energy harvesting at low frequency ( $\sim 1$  Hz) by various wearable TENGs with power management. (g) Environmental mechanical energy harvesting by various TENGs with power management.

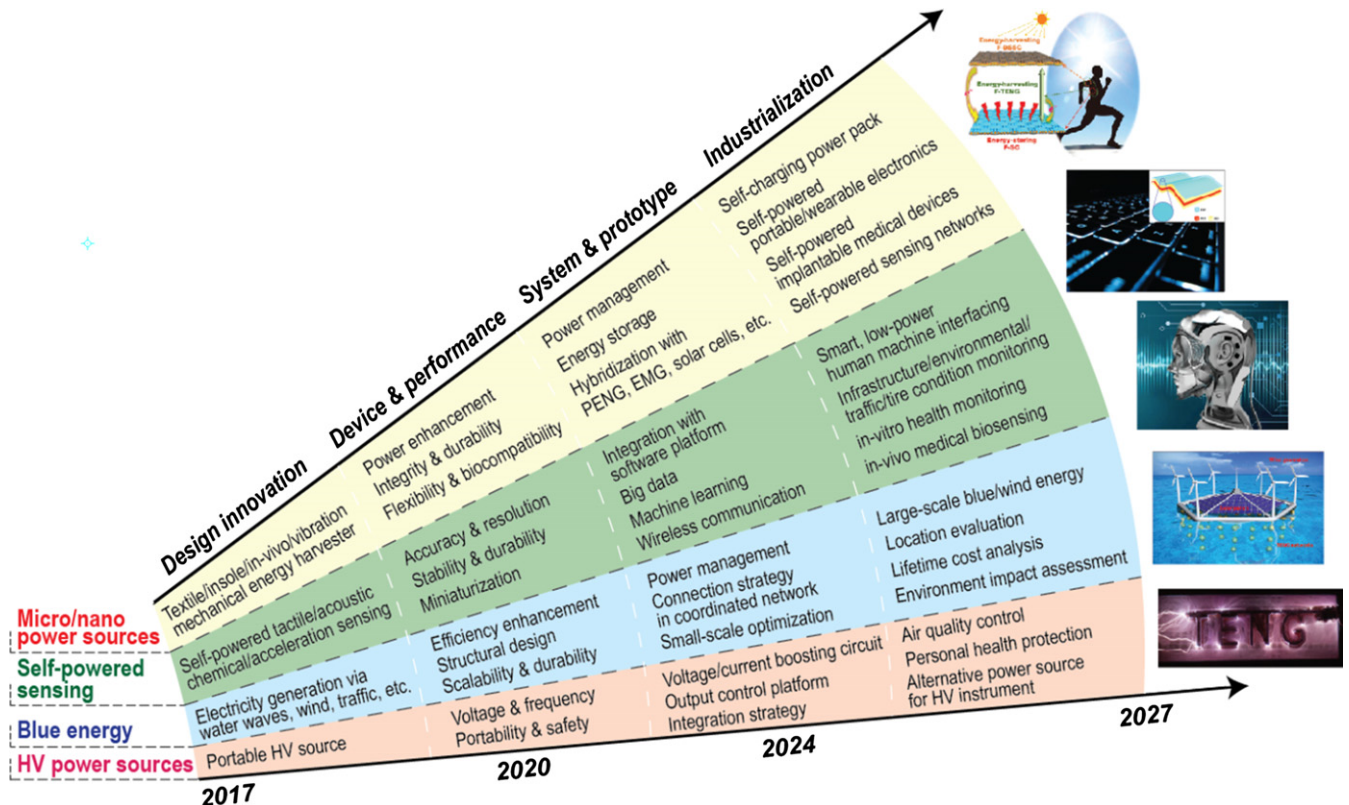


**Figure 38.** Four application fields of TENGs and a road map defined for the development of TENG technologies. [95] John Wiley & Sons. © 2019 WILEY-VCH Verlag GmbH & Co. KGaA, Weinheim.

under the stimulus of 1 Hz, the TENG matching impedance from  $35\text{ M}\Omega$  fell to  $1\text{ M}\Omega$  (figure 37(d)). It shows that the output impedance is greatly reduced, and the efficiency is 80.4%. When the capacitor of  $1\text{ mF}$  is charged for 5 min (figure 37(e)), the managed energy storage is increased by 128 times.

By breaking the technical bottleneck for practical applications, the power management module (PMM) is developed for TENGs. The PMM is integrated into a  $2 \times 2 \times 1\text{ cm}^3$  package, which facilitates the integration in the human body and the environment, such as self-powered wearable electronic devices (figure 37(f)) and wireless sensor networks (figure 37(g)).

## 5. Applications of triboelectric NGs

Internet is one of the most important drives for today's economy. It is not only for people-to-people, but also for people-to-object and object-to-object. Billions of moving objects around the world would be interconnected via wireless signals, and each need to be powered. This is the concept of distributed energy for sensor networks. Different from the traditional energy technology for concentrated power supply via cables, the newly distributed energy would involve energy being harvested from the local area and used locally without long-distance transmission. Considering the limited lifetime of batteries, building a self-powered system would be vitally important [84, 139]. TENGs were invented for harvesting mechanical energy from our living environment [91].

TENGs have a broad range of applications, which can be classified into four major areas: micro- and nano-power sources, self-powered sensors, blue energy, high-voltage sources (figure 38), and scanning probes for charge density measurements. We now use various examples to illustrate the broad applications of TENGs and their future impacts.

### 5.1. As micro- and nano-power sources

**5.1.1. Implantable medical devices.** Implantable medical devices (IMDs) are designed to perform the functions of organs by using monitoring-measuring-processing units and actuation control. Conventional IMDs are powered primarily by batteries that need painful surgeries for battery replacement. Thus, IMDs require a reliable and safe new energy solution to avoid the need for periodic surgeries. A critical requirement for IMDs is its power supply. Considering the high output voltage of TENGs and their excellent response at low frequency, they are ideally suited for converting muscle motion into electric power. The first demonstration of TENGs for biomedical application was by Zheng *et al* in 2014 [140]. A CS mode TENG was fabricated using biocompatible materials so that it can function well *in vivo* (figure 39(a)). The device was fully packaged so that no biofluid can infiltrate into the device. Large animal tests were first carried out by Ma *et al* [141] and Zheng *et al* [142] (figures 39(b) and (c)) to use TENG for powering a pacemaker. The output of the TENG is sufficiently high (figures 39(d) and (e)) that it can be used for effectively charging a capacitor. The first successful driving of a commercial

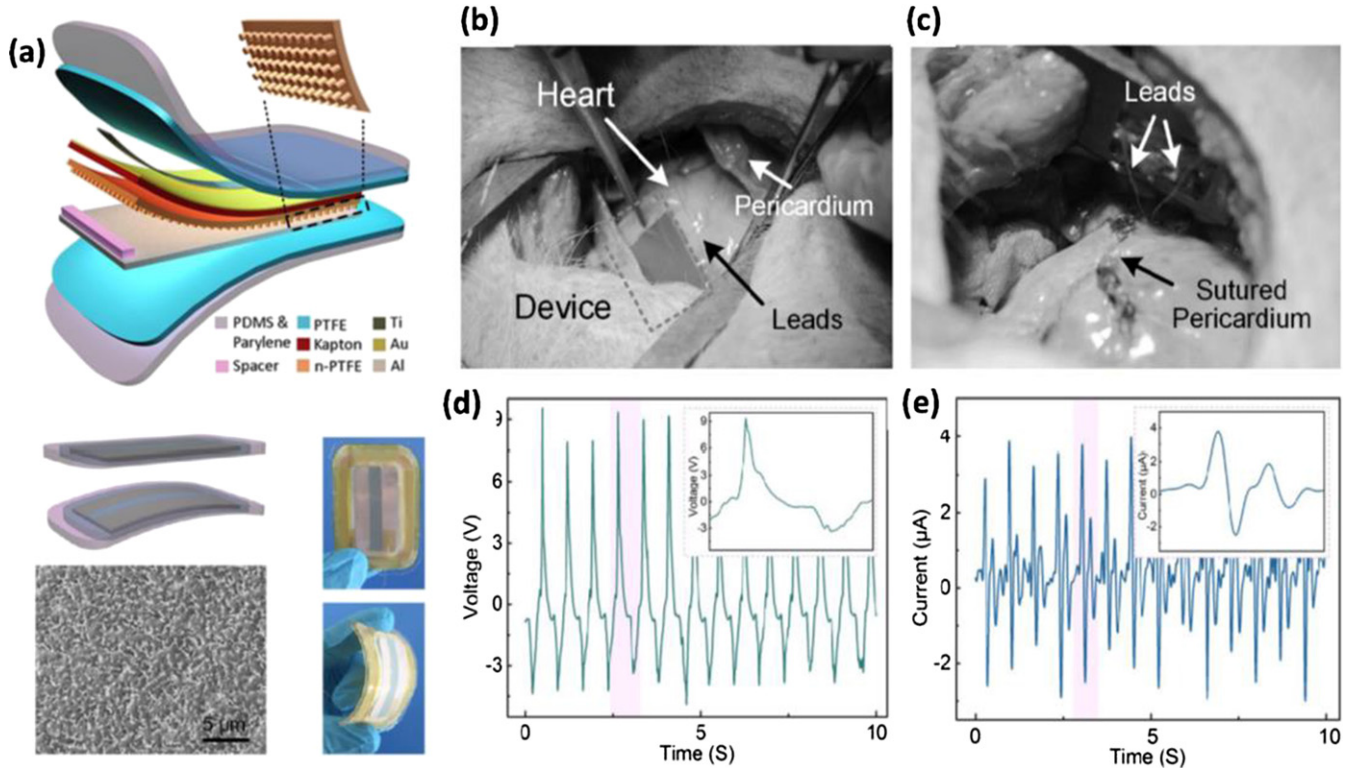


**Figure 39.** Pacemakers driven by implanted TENGs. (a) The structure and fabrication of the TENG. (b) and (c) The *in vivo* implantation process of the TENG in animal experiments. Reproduced from [143]. CC BY 4.0. (d) and (e) The output voltage and current of the TENG in responding to the cardiac motion. (a), (d) and (e) Reprinted with permission from [141]. Copyright (2016) American Chemical Society [143]

pacemaker by the cardiac motion of a large animal was demonstrated by Ouyang *et al* [143], who unambiguously showed the feasibility of using TENGs for driving implanted medical devices. Cardiac motion can generate an output voltage of a few volts, which is much larger than that from piezoelectric sensors, so that TENG can be an excellent biomedical sensor whose output is so high that the measurement circuit can be relatively simple and cheap. Since the materials used for fabricating TENGs can be diverse, any materials that are good for biomedical science can be a choice, making it possible to fabricate biodegradable TENGs [144]. This is rather unique for medical science because of the unrestricted choice of materials for TENG.

Recently, Hinchet *et al* [145] presented an ultrasound energy-harvesting technology based on TENGs for IMDs. Ultrasound has been approved by the FDA as a treatment method in various medical applications. Sound waves can travel through biological tissue (e.g. transcutaneous skin) to cause specific regions to oscillate. They applied 20kHz frequency and  $1 \text{ W cm}^{-2}$  input power ultrasound to generate electricity for powering IMDs inside the body by using an ultrasound-driven TENG (US-TENG) [145] (figure 40(a)). The US-TENG operates in single-electrode mode using a Cu/Au electrode as the primary electrode, a small backside Cu electrode as the reference electrode, and the perfluoroalkoxy (PFA) membrane as a triboelectric layer. When vibrating, the PFA membrane contacts the electrode and the triboelectric phenomenon generates negative charges on the inner surface of the membrane. These charges decrease the electrical potential

of the electrode compared to the reference, and thus generate a current pulse in the circuit. When separating, the electrode's potential increases, releasing holes in the circuit and generating a reverse pulse. Because the aim of the study was to develop an external charging system for electronic transcutaneous implants, they characterized the US-TENG under porcine tissue, which is comparatively similar to human skin in terms of anatomy and composition, and *ex vivo* characterizations were performed. At 0.5 cm, the VI-TEG generated output signals of more than 2.4 V and  $156 \mu\text{A}$  (figure 40(c)). They inserted US-TENG under porcine tissue, showing that it fully charged a rechargeable Li-ion battery to a capacity of 0.7 mAh.

**5.1.2. Flexible and fiberbased electronics.** Considering the triboelectricity among fibers for textiles, it is possible to integrate fiber-based TENGs with advanced materials for achieving smart textiles [146–149]. On one hand, TENGs can be easily designed as or integrated into textile structures, such as fiber, yarn and fabric, endowing them with mechanical energy harvesting and self-powered sensing capabilities. On the other hand, textiles provide versatile flexible design carriers and extensive wearable application platforms for the development of TENGs, because they are wearable, breathable, comfortable, structurally flexible, mechanically robust, and fit for low-cost implementation and large-scale production [150]. Since the human body is an inexhaustible and cost-free power source, and clothes are an indispensable necessity in people's lives, textile-based TENGs will become a highly attractive platform for unobtrusively harvesting human motion energy

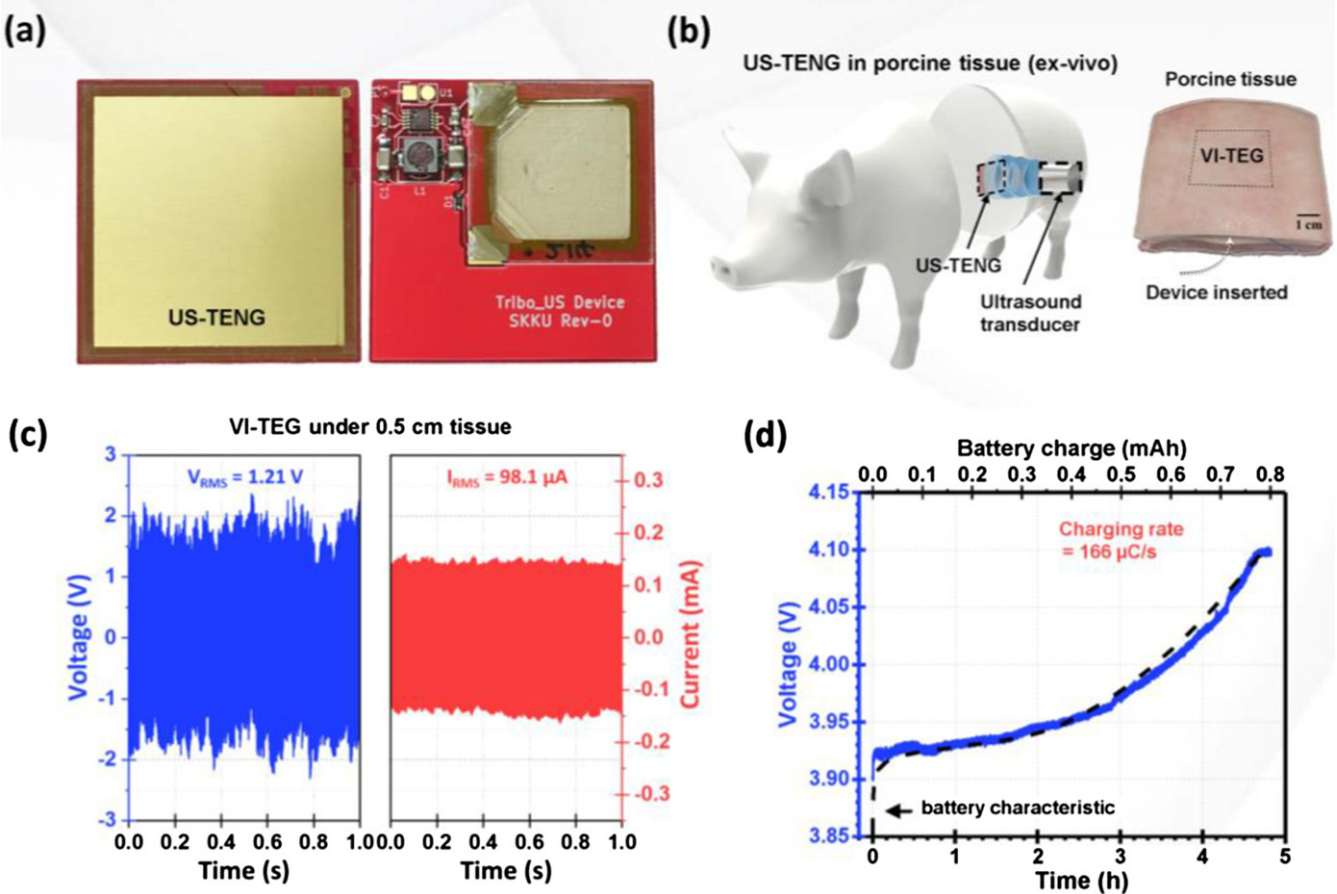


**Figure 40.** Ultrasound wave-driven TENG to power IMDs. (a) Front and back photo of the ultrasound TENG (US-TENG). (b) Schematic of the porcine *ex vivo* and the tissue. (c) US-TENG characterization *ex vivo* and inside porcine tissue which was triggered with an applied 20 kHz US at  $1 \text{ W cm}^{-2}$  reaching 1.21 V and  $98.1 \mu\text{A}$ . Voltage at  $40 \text{ M}\Omega$  impedance, and current at  $1 \text{ M}\Omega$  impedance generated by the US-TENG implanted at 0.5 cm. (d) Charging behavior of a rechargeable Li-ion battery having a capacity of 0.7 mAh. From [145]. Reprinted with permission from AAAS.

[151–153]. Without additional energy supplies and deliberate external working conditions, the self-powered systems can operate normally and continuously without interruption.

A TENG can be made into a textile. Nearly all fibrous materials (cotton, silk, nylon, polyester, etc) used for a common textile are good candidates for TE, which, together with conductive fibers or coatings as the electrodes to extract the inductive charges, are enough to produce a textile TENG. Unlike other energy devices requiring complicated materials and synthesis, a textile TENG can be possibly prepared by traditionally scalable waving/knitting processes with no sacrifice of the comfort, softness, aesthetic appearance, and even washing ability of fabrics. A number of textile-based TENGs have been reported with a two-electrode mode [154, 155], single-electrode mode [156], or interdigitated-electrode mode [157] for harvesting multi-types of human motion energies, such as tapping, rubbing, bending, etc. Figure 41(a) shows a schematic illustration of a textile TENG working in a two-electrode CS mode. The outer shell layers of the two fibers are different in the triboelectric series table, leading to the generation of static charges once being brought into contact (figure 41(b)). Then, an inductive AC current will be generated through the external circuit flowing back and forth to maintain the local charge

equilibrium when the two fibers are approaching or separating. For one approaching–separating cycle, the typical SC current and OC voltage is shown in figure 41(c).

2D textile-forming structures are relatively simple, easy to prepare, and compatible with existing textile-processing technology, making them popular in the design of smart textiles. However, due to the limitations of structural dimensions in the thickness direction, the power output of 2D textile structures is still low. In order to further improve the output performance of textile-based NGs, 3D textile structures have been used. Instead of increasing the transverse contact area or applying additional functional processes, the 3D textile structure increases the number of layers in the thickness direction, which can provide more contact and separation spaces. With a 3D orthogonal woven (3DOW) structure, a new kind of TENG is developed by using the silver-plated polyester yarns as the warp yarns, polydimethylsiloxane (PDMS)-coated energy harvesting yarns as the weft yarns, and non-conductive cotton yarns as the binding Z-yarns in the thickness direction (figure 42(a)). Z-yarns combine the warp and weft yarns by interlacing up and down along the warp direction over the weft yarns. Under an applied frequency of 3 Hz and a striking force of 20 N, a 3DOW-TENG with a size of  $15 \times 15 \text{ mm}^2$  can

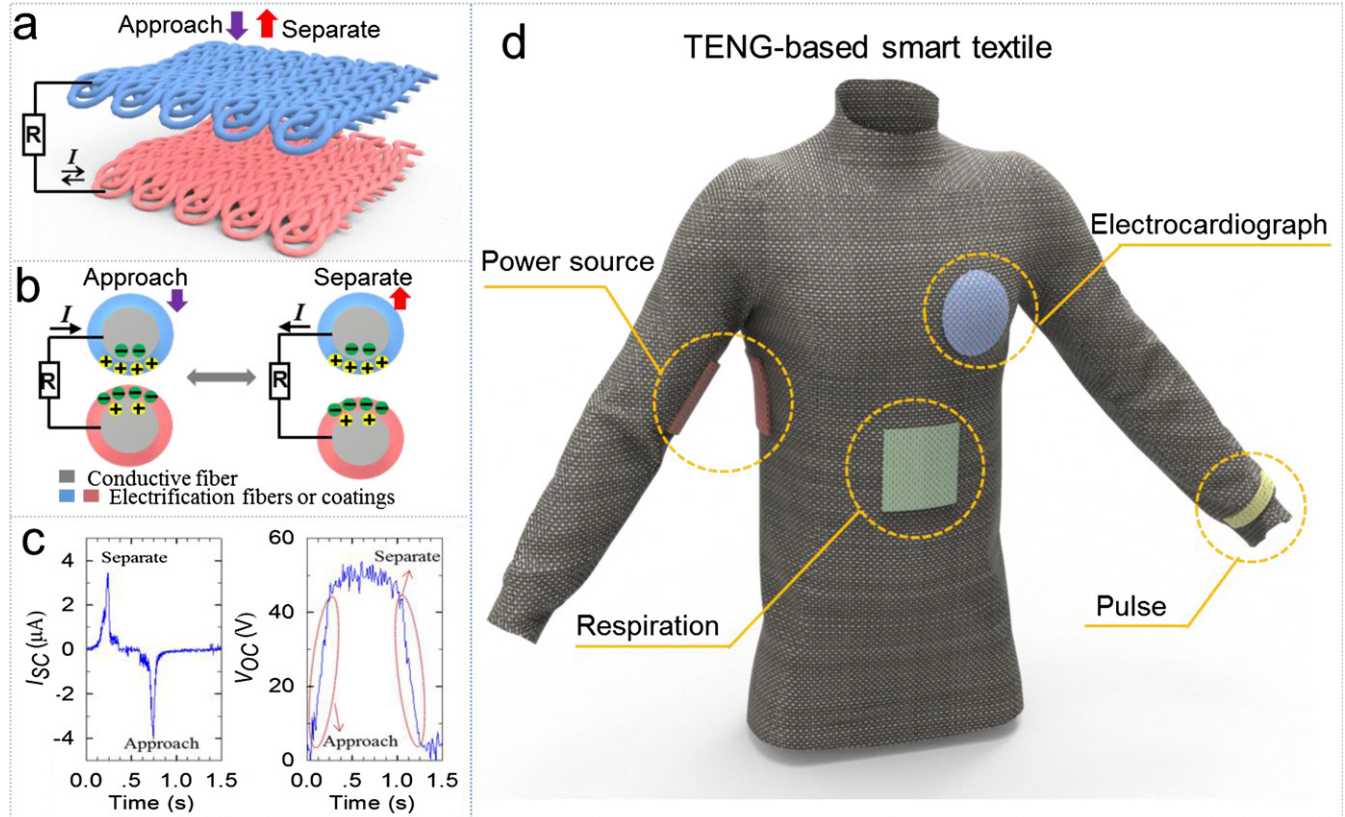


**Figure 41.** TENG-based smart textiles. (a) A scheme of a CS mode TENG textile, (b) the mechanism of how a fiber-based TENG works in response to the relative motion of fibers, and (d) corresponding typical output SC current and OC voltage. (d) The potential applications of TENG-based smart textiles. [154] John Wiley & Sons. © 2015 WILEY-VCH Verlag GmbH & Co. KGaA, Weinheim.

reach  $260 \text{ mW m}^{-2}$  at an external load resistance of  $130 \text{ M}\Omega$  (figure 42(b)).

The textile TENG has great potential in smart electronic textiles. The current trend is to transform a textile into a multi-functional platform, which collects all physiological information, provides certain therapy, and interacts with portable smart terminals or cloud terminals [158]. The textile TENG can play a vital role in many ways. First, it can serve as a power source. Textile-based self-charging power textiles have been proposed, which integrate energy-harvesting TENG textiles and energy-storing supercapacitor/battery textiles [159]. Irregular human motion energy is then transformed into a stable electricity output for powering wearable electronics. Some other types of textile-based energy devices can also be combined for hybrid power sources, such as fiber/textile-based solar cells [160, 161]. Second, the mechanical-to-electrical signal conversion of the TENG can be applied as sensors for monitoring multiple types of physiological information about the human body, such as pulse, electrocardiograph, respiration, or other human activities [162–164]. Finally, textile TENGs can function as human-machine interfaces. For example, a single-electrode TENG textile was prepared with different coding designs for remote control of vehicles or virtual reality games [165, 166].

**5.1.3. Internet of things.** As the world marches into the era of the internet of things, billions of objects around the world

need inter-communication and tracking. Power is inevitably needed for the sustainable operation of each unit. This is the era of the self-powered system. Water quality control and mapping [167], environmental protection [168], wild fire prevention, monitoring of infrastructures such as pipes and bridges, and monitoring of land motion [169] are typical examples of the internet of things. TENGs are ideally suited for such purposes. Figures 43(a) and (b) show an example of using TENGs as distributed units for monitoring water quality, such as pH. The unit is driven by a TENG using the energy supplied from a water wave. The system consists of a TENG, energy storage unit, sensor, and data processing and transmission system. The integrated unit sends out a signal periodically to a central data-receiving platform. The system can be expanded to land by using wind energy for environmental protection by detecting a variety of relevant parameters, such as a landslide (figure 43(d)).

Technology for harvesting wind energy is very mature, but such a generator is rather huge. For small electronics, we can use a wind tunnel built by inserting a flexible vibrating ‘tong’ inside (figure 44(a)), which oscillates once the wind flows through the tunnel [170]. The contact and separation of the film with and from the upper and lower walls of the rectangular tunnel is a working TENG, which gives an electrical output (figures 44(e) and (f)). By integrating several units together,

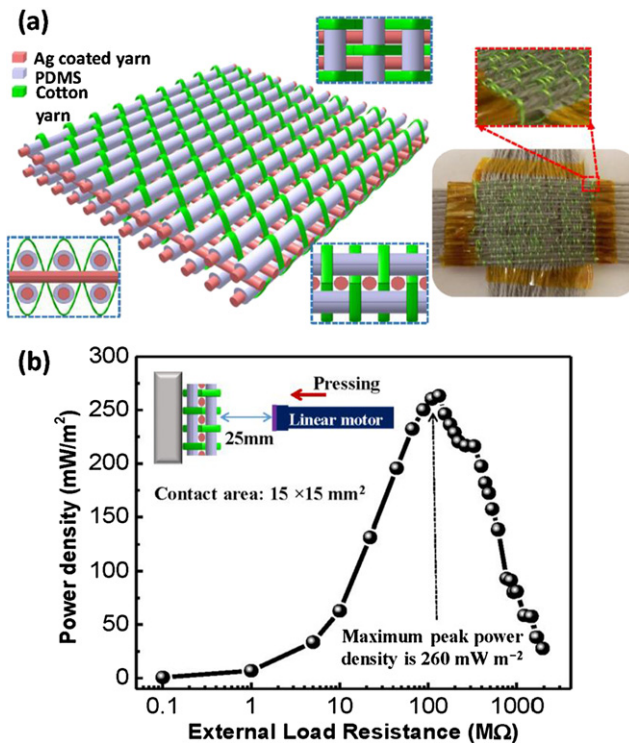


**Figure 42.** Fiber/textile-based TENG. (a) Schematic illustration and photograph of the 3D orthogonal woven TENG (3DOW-TENG). (b) Measuring conditions and maximum peak power density of the 3DOW-TENG. [148] John Wiley & Sons. © 2020 WILEY-VCH Verlag GmbH & Co. KGaA, Weinheim.

the output power is sufficient to drive an environmental monitoring unit [171]. The self-powered system can detect CO sustainably and send out a wireless signal from 1.5 km away once every 18 min at a radio transmission frequency of 433 MHz. At a wind speed of  $4.5 \text{ m s}^{-1}$ , a humidity hybrid sensor can send out the monitoring data once every 9 min through bluetooth (2.4 GHz) in a range of 50 m. This clearly demonstrates the self-powered sensor network.

## 5.2. As self-powered sensors

Under external mechanical triggering, a TENG gives out current and voltage signals, and can also be used as a self-powered sensor for characterizing mechanical triggers, such as vibration, sound, and impact. The output voltage gives the magnitude of the trigger, while the output current gives the rate at which the trigger is applied, so that it can derive information related to velocity and acceleration. We now use the following examples to illustrate the applications of self-powered sensors in a variety of fields.

**5.2.1. Health care.** The pulse wave originates from the heart and propagates to peripheral arteries along the blood vessels, and the vital pathological information about cardiovascular events can be revealed by the pulse wave characteristics containing the rhythm, shape, wave velocity and so on. Therefore, the pulse diagnosis can offer remarkable insights into the cardiovascular health of individuals. Wearable sensors especially in flexible pulse wave sensors show potential applications in

the next generation of personalized health-monitoring devices for cardiovascular disease (CAD) assessment. Although the existing pulse wave sensors have made advancements in materials and fabrication processes, their practical applications still face many systematic challenges, such as being highly sensitive, stable and skin-conforming. Benefiting from excellent sensitivity and a wide selection of materials, TENGs offer a novel opportunity to develop flexible pulse wave sensors for mobile and remote medical diagnosis [173, 174].

As one of the stronger pulse wave signals in the whole body, the carotid artery pulse carries rich physiological information, as shown in figure 45(a). Inspired by the eardrum structure, the first TENG-based bionic membrane sensor (BMS) was developed, which has a multilayered structure mainly composed of the two electrification layers, namely, nanowire microstructure PTFE and nylon-coated indium tin oxide (ITO) [173], as shown in figure 45(b). Mimicking a human eardrum, the layer of PTFE tympanic membrane is tented outwards at the level of the tip of an umbo, enabling the BMS to capture the external dynamic pressure with high sensitivity and wide frequency range. The BMS exhibits great features including high sensitivity ( $51 \text{ mV Pa}^{-1}$ ), fast response time (less than 6 ms), low pressure detection limit (2.5 Pa) and stability (40 000 cycles). Compared to the previous wearable pressure sensors, the BMS showed the ability not only to monitor slowly-changing pressures such as the human arterial pulse, but also to acquire rapidly-changing pressures such as human throat vibration in a self-powered and non-invasive manner. Moreover, the simultaneously acquired voltage and current signals of the BMS independently but complementarily give a comprehensive picture of the human cardiovascular system by measuring its representative parameters (figure 45(c)), including radial artery augmentation index (AIx), reflection index (RI) and pulse pressure velocity (PWV), for assessing the status of the cardiovascular system.

For precise measurement of pulse waves from various body positions, the miniaturization and flexibility of wearable sensors are further required, as shown in figure 45(d). Therefore, a WCSPS has been fabricated, which is composed of polyethylene (PE) terephthalate and weaving constructed PTFE with microstructure [175] (figure 45(e)). The weaving structure not only ensures the high resilience of the electrification layer, but also maintains the high sensitivity ( $45.7 \text{ mV Pa}^{-1}$ ) even with a small scale of  $10 \times 10 \times 1 \text{ mm}^3$ . The WCSPS enables the capacity to monitor the human pulse wave at different positions including fingertips, wrist, ear, and ankle (figure 45(d)), and is capable of capturing the critical characterization points of the pulse waveform, which provides a guarantee for enabling continuous diagnosis of CAD and measurement of cuffless blood pressure (BP). A series of practical measurements of the cardiovascular parameters from 100 people with ages from 24 to 82 years old with different health statuses was carried out. There is a slight discrepancy, about 0.87%–3.65%, between the measured BP results by our sensor and that provided by the commercial cuff-based device, as shown in (figure 45(f)). It can be proved that the sensor would be a competitive alternative to current complex and expensive healthcare facilities such as hospitals or nursing homes.

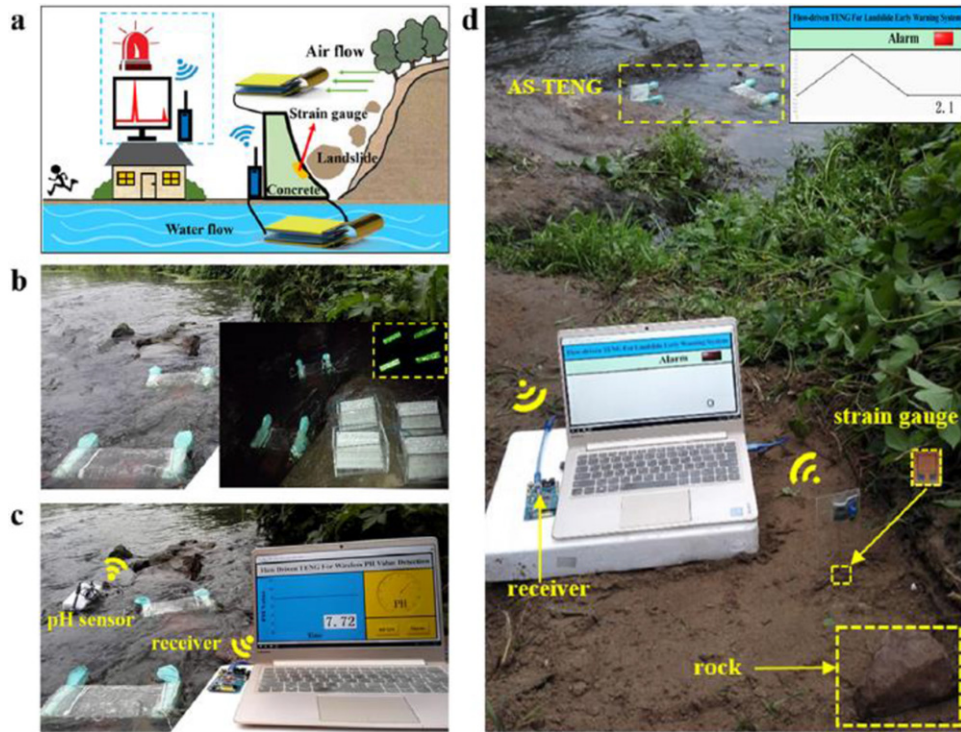


**Figure 43.** Demonstration of the TENG as a practical power source for driving a system used for environmental protection. (a) Schematic diagram of the wireless landslide early warning system powered by the AS-TENG array. (b) The AS-TENG array harvested the flow water energy in a river and 480 LEDs were lit up. (c) Photograph of a wireless water quality monitoring system powered by a TENG array in the river. (d) Photograph of the system functioning in the natural environment, producing a landslide monitoring alarm once the rock was released and had impacted with the strain gauge. Reprinted from [168], Copyright (2018), with permission from Elsevier.

In addition to wearable sensors, endowing ordinary objects with the ability to perceive physiological signals through physical finger-touching will be a new trend for health monitoring, as shown in figure 45(g) [176–178]. Therefore, the nanohemispherical fingertip-contact pressure sensor (FPS) was fabricated using nanohemisphere-arrayed PE and PDMS coated with gold [179] (figure 45(h)). The FPS can be attached to a mobile phone, a keyboard with protective film, human skin, and even a soft pillow due to its remarkable flexibility and bendability. Once the finger touches the FPS, the fingertip-pulse signals can be captured by the FPS and displayed through the smart mobile terminal application (APP). From the obtained fingertip-pulse wave, more valuable information about the cardiovascular system can be calculated, such as K value (which is determined only by the shape of the pulse wave), AIx, artery compliance (AC) and cardiac cycle ( $\Delta T$ ) (figure 45(i)). The FPS makes the surfaces of ordinary objects capable of perceiving dynamic epidermal pulse signals, which is an important supplement to traditional wearable devices for accurately assessing health conditions without restrictions on time and location.

Textile sensors offer excellent comfort, but they typically have low sensitivity and a single monitoring parameter, and cannot be manufactured on a large scale. This will remain a major obstacle to their future applications. Therefore, a smart textile with both comfort and excellent sensing performance is required to address these limitations (figure 45(j)). The textile-based sensor is composed of a silver-coated polyester fabric

and an embossed flower-shaped textile [180], which can be woven into clothing as a logo. It exhibits a superior pressure sensitivity of  $3.88 \text{ V kPa}^{-1}$  under a range of  $0.1\text{--}4.3 \text{ kPa}$ , which is adequate to perform tiny and weak human pulse wave monitoring. In addition, a TATSA that is knitted with conductive and nylon yarns in a full cardigan stitch has been developed (figure 45(k)) [181]. It exhibits superiority in sensing performance (high pressure sensitivity of  $7.84 \text{ mV Pa}^{-1}$ ) and wearability (seamlessly stitched into the clothes). It can be completely self-contained or stitched seamlessly into the lace, wristband, fingerstall, and sock and even stitched directly into different parts of clothes to transform ordinary clothes into smart clothes. Comparison experiments indicate that the TATSA can acquire pulse signals and respiration as accurately as a standard medical instrument (MHM-6000B) in contours and details (figure 45(l)). A personalized intelligent health monitoring system integrated with the TATSA has been developed for long-term and non-invasive assessment of CAD and the assessment of sleep apnea syndrome.

Studying the human body, especially the skin, is vitally important for health care. The electrical properties of the body are unique due to its biological structure. The tissue under the skin has a low resistance of  $300 \Omega$  [182], while the epidermis layer on the surface of the skin has a high impedance of up to  $10 \text{ M}\Omega$  [183] depending on the skin conditions. Such a unique high impedance surface and low resistance tissue are very similar to a typical component of TENGs (figures 46(a) and (b)). Therefore, we can take advantage of the electrical

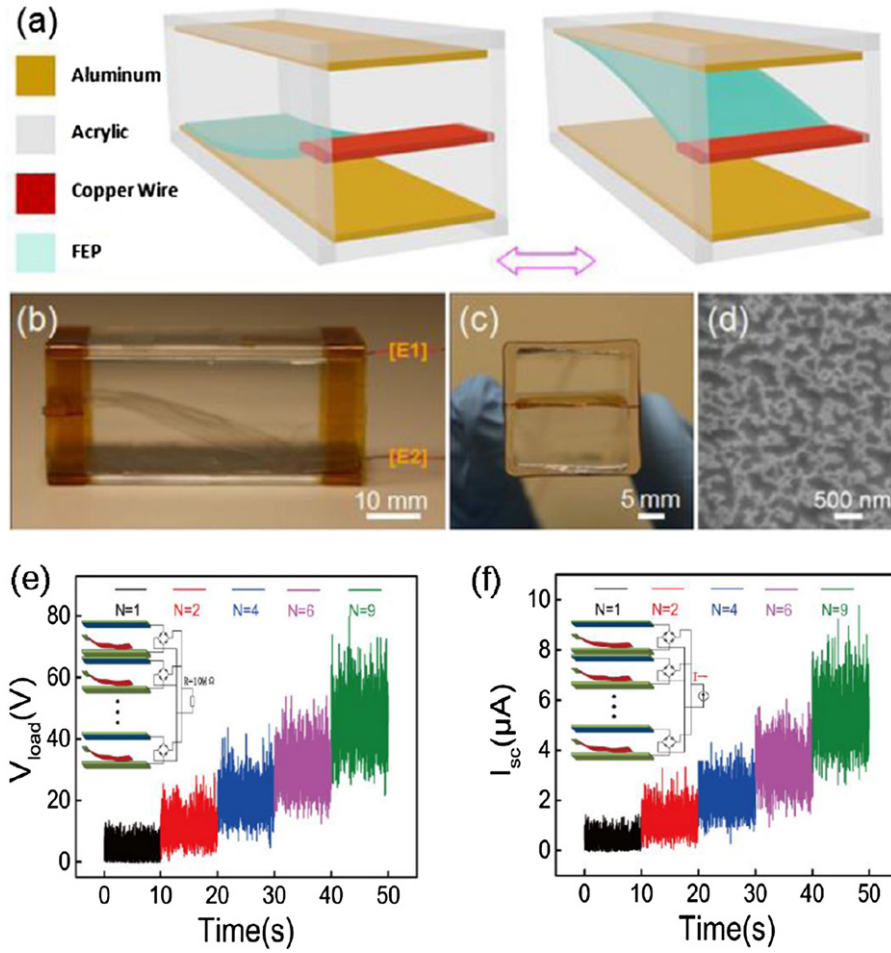


**Figure 44.** Harvesting energy from wind by TENG. (a) Schematic diagram of the TENG. (b) and (c) Photographs of the TENG. Reprinted with permission from [172]. Copyright (2013) American Chemical Society. (d) SEM image of the etched FEP film surface. (e) and (f) Rectified OC voltage and SC current of several units in serial and parallel connection, respectively. Reprinted from [171], Copyright (2020), with permission from Elsevier.

properties of the human body and construct human body-based TENGs (H-TENG). Zhang *et al* [184] and Zhang *et al* [185] have reported H-TENGs to convert the mechanical energy of human body motions into electricity. Their study indicates that the output power density from a human body can reach  $30 \text{ W m}^{-2}$  when patting a PTFE film by hand.

Mechanisms of how a human body behaves in the H-TENGs have been studied experimentally for the following two hypotheses. The hypothesis is based on the DC resistance breakdown voltage of the human skin that is 500 V [186]. In hypothesis I (figure 46(c)), the voltage on the skin after TE with the PTFE is higher than the resistance breakdown voltage, and the charges flow directly across the skin and through the body, then across the skin and flow to the electrode. In this hypothesis, the human body acts as a conductor. To verify the hypothesis, experiments are designed and the results are given in figures 46(d)–(g). The current shown in figure 46(d) indicates the flow of charges across the skin, while the voltage shown in figure 46(e) shows that the voltage can go above the resistance breakdown voltage.

In hypothesis II (figure 46(h)), the voltage on the skin after TE with the PTFE is lower than the resistance breakdown

voltage. In this case, the role played by the human body is a network of many capacitors and resistors. Therefore, the charges generated need to pass through these capacitors and resistors, resulting in decayed charge flow. The hypothesis was verified by two simple experiments (figures 46(i)–(l)), where the charges on the human body were released several times. Results proved that the human body acts as a capacitor [187], but not a typical capacitor, since the charges are not continuously released as shown by the four peak currents in figure 46(j). The reason behind this could be that the charges are first stored in the body and then flow to the tapping finger due to the potential gradient. The charges accumulated at the tapping finger build up the potential and will break the resistance of the skin when it is above 500 V [186]. Results in figure 46(l) show how the potential builds up after each charge releasing procedure.

In practice, both hypotheses I and II occur because the potential is unevenly distributed, since the skin is not a flat surface. Some parts of the skin have an electric potential higher than 500 V, while some parts do not. Therefore, the roles played by a human body in an H-TENG are as a triboelectric layer, a conductor and a capacitor. Taking advantage of the

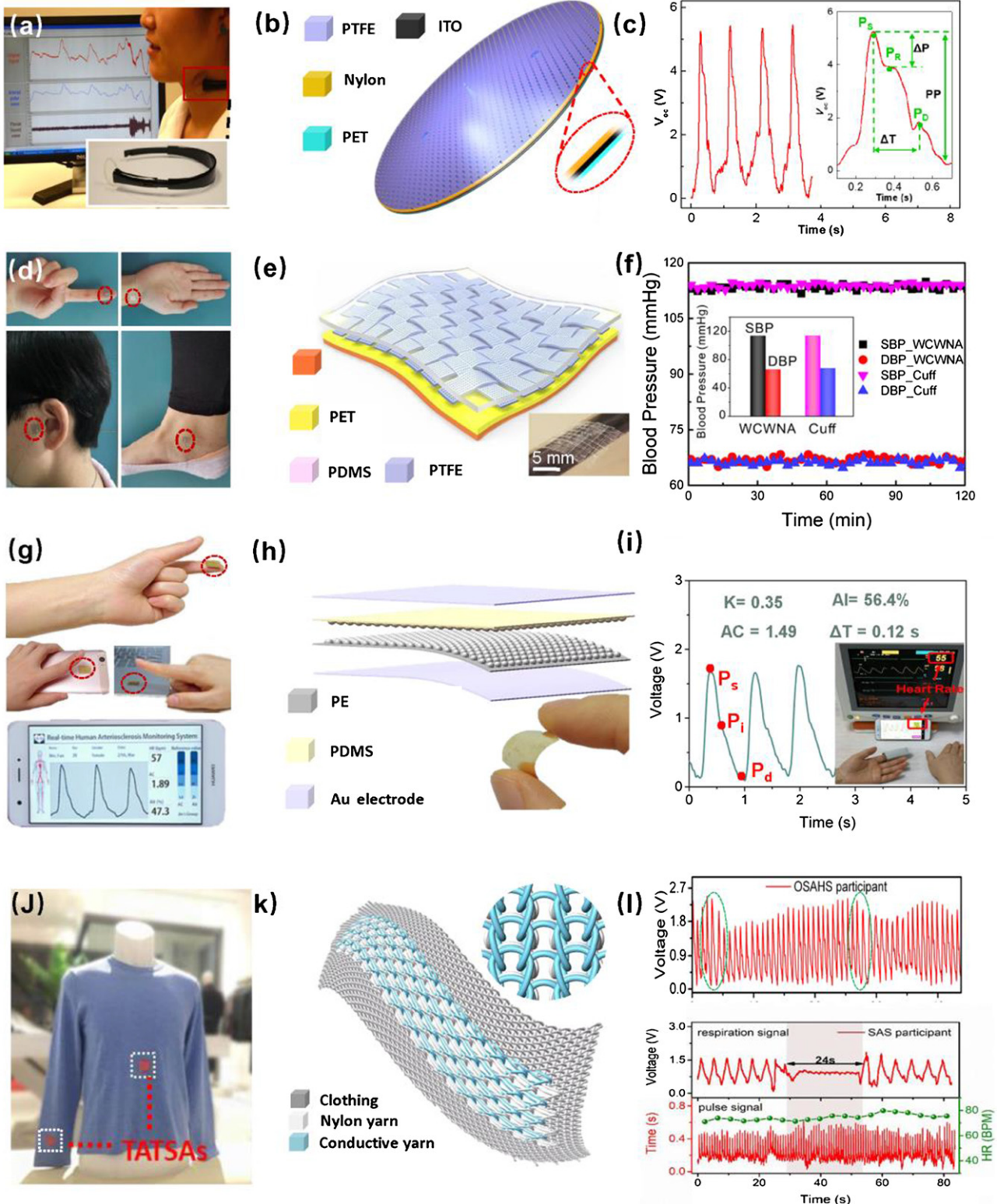


**Figure 45.** TENG-based flexible sensors for monitoring physiological signals. (a) A BMS was worn against the participant's neck for monitoring carotid artery pulse. (b) Structure of the BMS. The enlarged view shows the details of the structure. (c) The real-time voltage outputs when the sensor was placed over the carotid arteries of a 30 year-old man. The radial artery AIx and RI can be obtained from the measured signals. (d) Photographs showing that the weaving constructed self-powered pressure sensor (WCSPS) was directly worn at the fingertip, wrist, ear, and ankle, respectively. (e) Structure of the WCSPS. A photograph showing an as-fabricated WCSPS, which is flexible, lightweight, and can be easily wrapped onto a curved surface. (f) The measured BP results by WCSPS. (g) Illustration and acquired pulse wave signals when the fingertip-contact pressure sensor (FPS) is attached to skin, a mobile phone and a computer keyboard. (h) Structure of the FPS. The inset shows that the FPS is ultrathin. (i) Fingertip-pulse waveform of a 65 year-old participant. The inset shows simultaneous fingertip-pulse wave monitoring using the FPS and a commercial medical monitor. (j) Photograph of two triboelectric all-textile sensor-arrays (TATSAs) completely and seamlessly stitched into a sweater. (k) Structure of TATSA. (l) The measured respiratory and pulse signals of a participant.

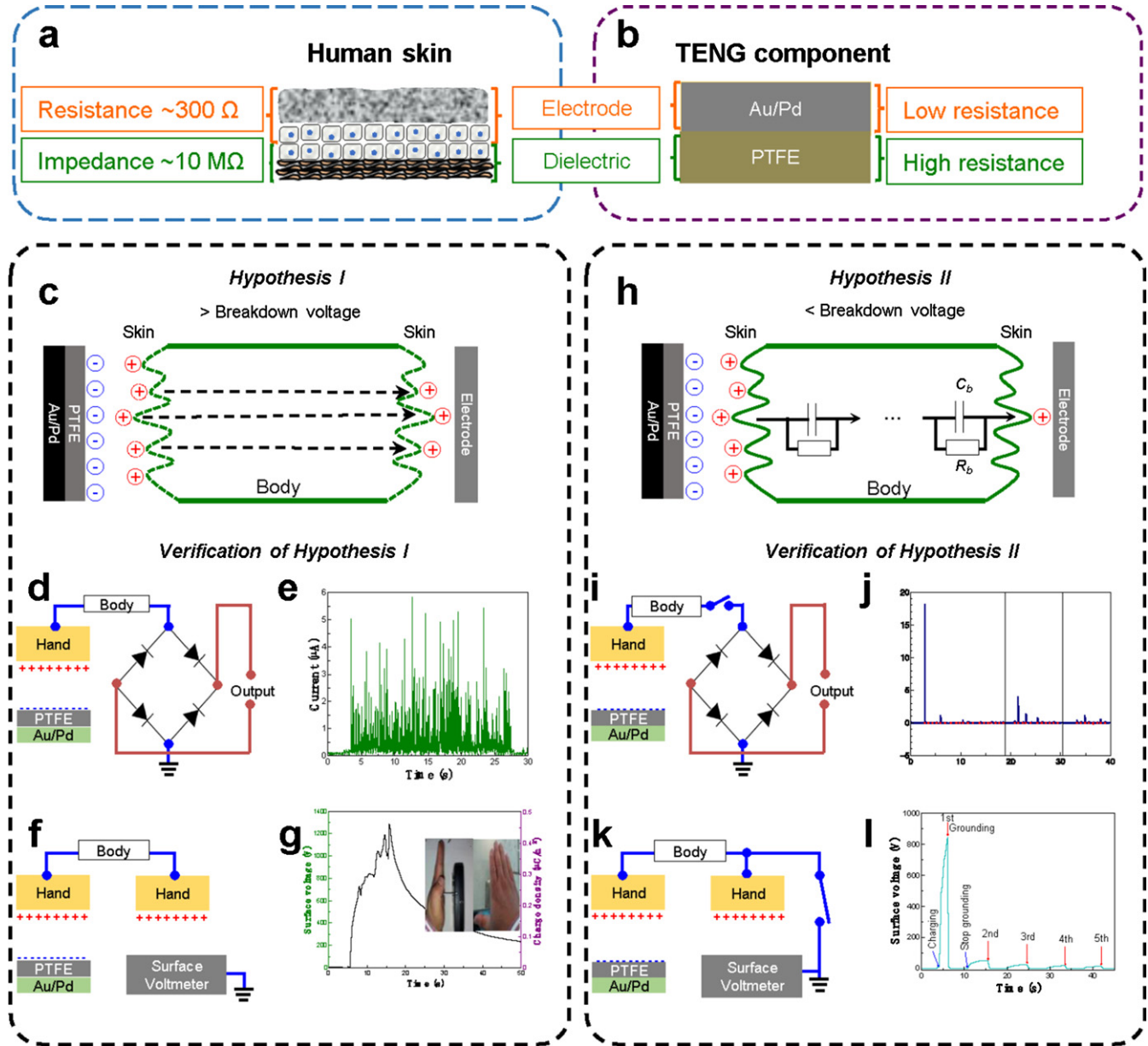


**Figure 46.** Hypothesis and verifications of the function of a human body in an H-TENG. (a) and (b) Structure of human skin and a typical TENG component. The epidermis of the skin and PTFE are dielectric materials with a high impedance or resistance, while the dermis and the electrode deposited on PTFE have low resistances. (c) Hypothesis I: a surface voltage above the skin's breakdown voltage drives charges through the body. (d) Circuit to measure the current passing through the human body. (e) Current measured based on the circuit of (d). (f) Circuit to measure the surface voltage of the hand. (g) Measured surface voltage of the hand and the corresponding surface charge density. (h) Hypothesis II: the body acts as a network of capacitors and resistors when the surface voltage is lower than the skin's breakdown voltage. (i) Circuit to measure the charge flow from the human body when the body was pre-charged and connected to the circuit by tapping a finger on a metal wire. (j) Current measured for finger tapping based on the circuit of (i). (k) Circuit to measure the surface voltage of the hand before and after grounding. (l) Measured surface voltage of the hand during five cycles of grounding. Reprinted from [184], Copyright (2018), with permission from Elsevier.

unique electrical behaviors of the human body in the H-TENG, a universal body motion sensor (UBS) is developed [188]. The UBS is a self-powered sensor, where the electricity generated in the human body supplies the power, and the changes of electrical signals represent different body motions. Different body motions can be identified by analyzing the electrical signals. Proof-of-concept experiments have shown the potential of the UBS in healthcare applications, especially in

monitoring of abnormal body motions caused by Parkinson's disease and injuries.

**5.2.2. Security.** A touching sensor is one of the most important security sensors for medical, smart home, safety and sports applications. A single-electrode TENG was fabricated by He *et al* [189] by using ultrathin materials (figure 47(a)), which is so thin and flexible that it can be attached to the surface of

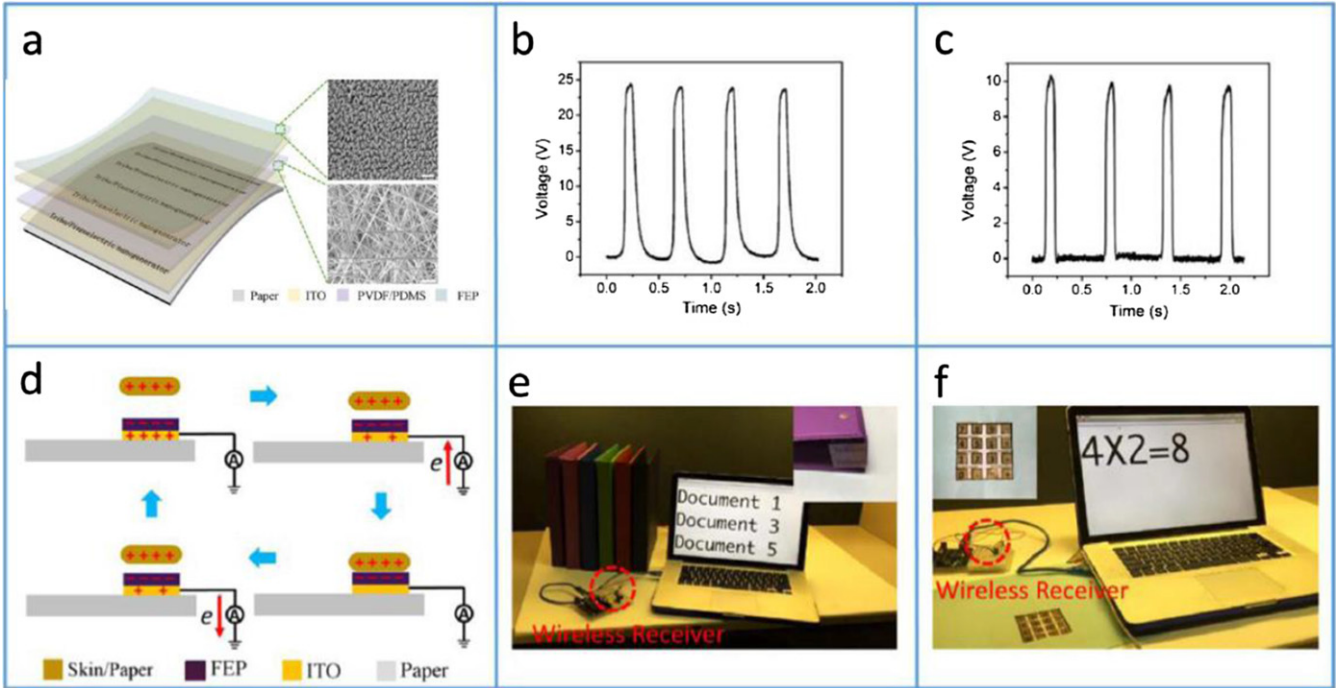


**Figure 47.** Touch sensor warning system. (a) Fabrication process and schematic of the TENG. (b)  $V_{oc}$  output of the single-electrode TENG when it repeatedly lifts up and lays down between the TENG and paper. (c)  $V_{oc}$  output of the single-electrode TENG when it repeatedly touches with and separates from a finger. (d) The work mechanism of the single electrode TENG triggered by finger/paper touch motions. (e) Photograph of the book management system. (f) Photograph of the paper-based calculator functionally triggered by finger touch motions. Insert image shows the photograph of the paper-based finger touch calculator. Reprinted from [189], Copyright (2017), with permission from Elsevier.

any object. Once the sensor is touched by a finger or a paper, owing to the different dielectric properties and surface TECD, the output of the sensor is distinctly different (figures 47(b) and (c)), based on which the sensor can distinguish what it has touched. The working mechanism of the sensor is illustrated in figure 47(d). By attaching the sensor at the bottom of a book, a signal is given once it is moved, and such a signal can be transmitted wirelessly to a receiver, allowing an automatic detection of which book was moved and when was it moved (figure 47(e)). A similar idea can be used for detecting which lines were touched by the one who moved the book (figure 47(f)). Such a self-powered system is not only a document management system, but also a security system. The touching sensor is one of the unique applications of TENGs, simply due to the universal TE effect of all materials/objects.

Sensing of impacts, triggering and touching is important for security and motion control. A TENG is ideal for detecting any tiny mechanical triggering with a high output signal. Monitoring and identification of eye-blinking has great advantages in mechnosensational communication systems, especially for patients suffering from amyotrophic lateral sclerosis. To date, an electrooculogram (EOG) [190–192] based on the corneal-retinal bio-potential difference is widely used as a good control signal for healthy people and even ‘locked-in’ patients who can still blink their eyes [193]. The potential difference is determined at least on two exposed electrodes (usually a ‘wet electrode’ as Ag/AgCl electrode) pasted around the sensitive eyes [194], which have discomfort and poor esthetics. In addition, the amplitude of the EOG is very weak, rang-

ing between  $50 \mu\text{V}$  and  $3.5 \text{ mV}$ , and is often buried in noises and difficult to detect unless using sophisticated and expensive instruments [194]. Therefore, a sensitive, usable, stable, comfortable, and esthetic sensor is desired for constructing the eye-blinking based human–machine interface.

Considering the existence of mechanical micro-motion on a human face when blinking eyes, we reported a novel TENG-based eye-blinking sensor (TEBS) by coupling of TE and electrostatic induction. As shown in figure 48(a), utilizing an ITO electrode and two opposite tribo-materials, a TEBS is a flexible, transparent and facile sensor, which can be mounted on a pair of glasses and is much more practical than traditional EOG electrodes. In addition, the TEBS is capable of effectively capturing eye blink motion with a super-high signal level ( $\sim 750 \text{ mV}$ ), nearly three orders of magnitude higher compared to the EOG approach ( $\sim 1 \text{ mV}$ ) (figure 48(b)). For demonstration, without using a complexed signal filtering circuit, an eye-blinking controlled wireless typing system with ultra-high accuracy and stability were successfully built up based on a TEBS as presented in figures 48(c)–(e). With these capabilities, TENG technology would provide a solid base for the future development of mechnosensational human–machine interfacing.

**5.2.3. Personal authentication.** Due to rapid development in this information age, network information security has become a hidden danger. A variety of keyboards, touch pads, as the most common, accessible, and effective devices used for human–machine interfacing and information exchange,

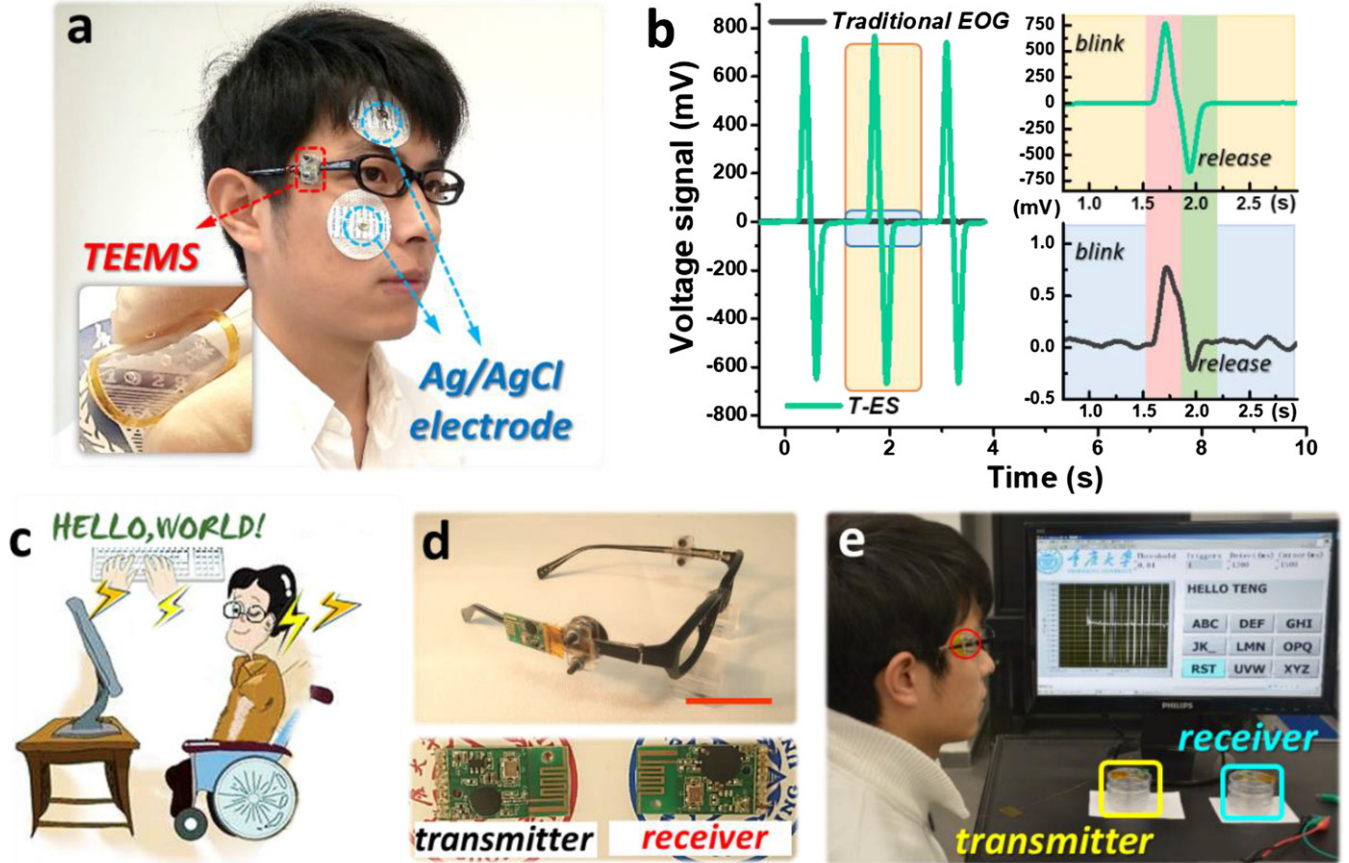


**Figure 48.** Highly sensitive triboelectric eye-blinking sensor (TEBS). (a) Practical wear comparison between biological gel electrode and tribo-sensor. Inset: a transparent and flexible TEBS device. (b) Output voltage signal of bio-electrode and TEBS when blinking. (c) Sketch of the eye-blinking interface to help people suffering from ‘locked-in syndrome’. (d) photograph of a pair of TEBS-based wireless eye-blinking glasses. (e) Demonstration of the TEBS-based hands-free wireless typing system. The words on the screen are typed with eye blinking. Reproduced from [195]. CC BY-NC 4.0.

are the key information input methods. As a mechanical-to-electrical conversion device, the TENG has been successfully used to build intelligent keyboards for information security applications without adding additional sensing devices. An exciting function of the TENG-based intelligent keyboard (TIK) is that the output signals reflect the behavioral biometric based on people’s typing attributes, i.e. the keystroke dynamics. Figure 49(a) is a typical authentication/identification application based on the TIK, which is proposed by Wu *et al* [196] and contains two processes, the training process and the authentication/identification process. During the training process, users will use the TIK to repeatedly input a string of characters, such as a password. After acquiring the corresponding electrical signals, some pre-defined features related to the biometric will be extracted from them and used to compose a profile database. Then, via machine learning with the help of SVM and principle component analysis, a trained classifier can be built to implement the authentication and identification. When a testing input is generated from the TIK, a test profile will be follow the same procedures. Then, under the role of the trained classifier, it can be used to either determine whether the test subject is an authorized user (authentication) or identify who the test subject is (identification). The

TENG can not only be easily integrated with commercial keyboards (figure 49(b)), but also build a keyboard independently (figure 49(c)). When the smallest key is gently touched, due to the CE between the finger and friction layer or two friction layers, the typical output voltage is described in figure 49(d), and can be adjusted by the participation of fingers. When typing a string of characters, the corresponding waveforms with normalized voltage are plotted in figure 49(e), in which the hold time ( $H$ ), typing latency ( $L$ ) and signal magnitude ( $M$ ) are specified as the keystroke features. The  $M$  is directly proportional to the typing force and all the keystroke features can reflect the personal input habit. This is the essence of the technology to realize authentication and identification. For an exemplary number sequence with six digits, a total of 17 features can be obtained accordingly. After five users typed the number sequence 150 times each, a radar plot of their normalized mean values were obtained to show distinctive typing behaviors among them (figure 49(f)). The 150 sets of data from each user are randomly split into two parts, one for training and the other for testing. Through tuning the decision threshold value and comparing the resulting false acceptance rate (FAR) and false rejection rate (FRR), the best performance of the

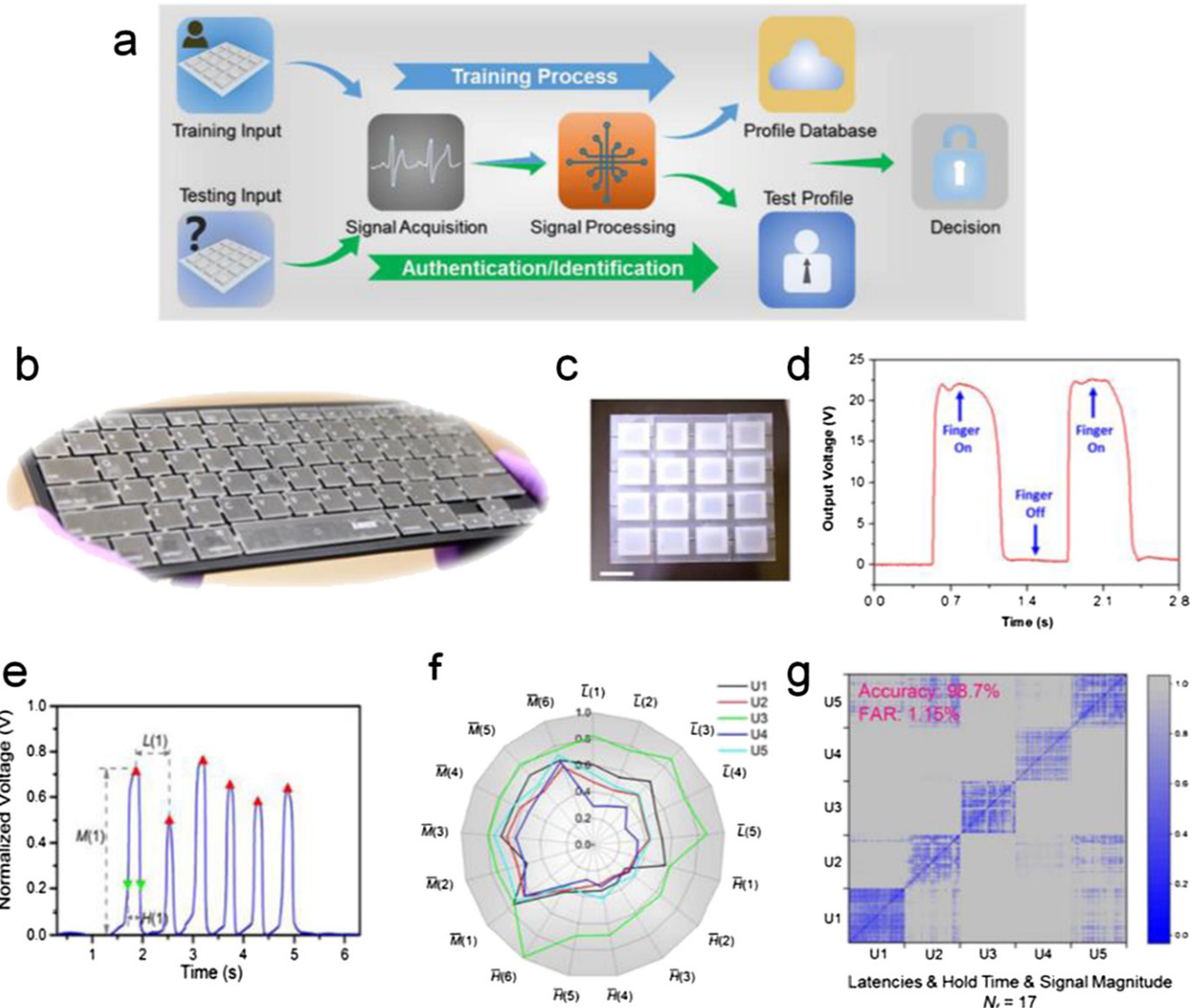


**Figure 49.** TENG-based keyboards for information security and authentication. (a) The system outline consisting of the training process and the authentication/identification process. (b) and (c) Typical TENG-based keyboards. (d) The typical output voltage when the smallest key is gently touched. (b) and (d) Reprinted with permission from [197]. Copyright (2015) American Chemical Society. (e) The keystroke features defined to construct user profile models. Typing latencies, hold time, and signal magnitudes are denoted as  $L$ ,  $H$  and  $M$ , respectively. (f) The radar plot of the normalized mean feature values of five users after they typed the number sequence '8-0-7-3-4-5' 150 times each. (g) The difference score matrices across user inputs with 17 feature types (a), (c) and (e)–(g) Reprinted from [196], Copyright (2018), with permission from Elsevier.

classifier can be achieved. With the optimal decision threshold of 0.75, the tradeoff between a low FAR and a low FRR can be well satisfied so that an equal error rate can be as low as 1.15%. To quantify the difference of users' typing patterns with varying combinations of feature types, a difference score between two typing inputs is introduced based on the normalized interval distance. As shown in figure 49(g), the scores across the diagonal should be much lower (more blue) compared to the rest, which indicates that the difference of inputs from the same user is much lower than that of inputs among users. Through introducing more features, a more ideal score matrix can be produced, which corresponds to a higher system accuracy and a lower FAR rate. Moreover, the keystroke dynamics will be affected by the users' emotional state, so that

the users have to remain calm in the information security applications. Inspired by this, through monitoring the users' emotional state, the TIK can also contribute to some applications of mental health administration and even information security.

Microphone-based voice recognition is an important technology. A paper-based TENG can be a cheap, high-quality and versatile voice recorder. Shown in figures 50(a)–(c) is a design of a holey paper that faces onto another paper separated by a small gap [198]. Once a sonic wave strikes on the holey paper, it vibrates at its resonance frequencies, and the touching and separating between the two paper layers give an output electric signal based on the principle of TENG (figure 50(e)). The frequency range of the TENG can be fairly broad based on the design of the holey paper (figure 50(e)). Thus, the TENG is not

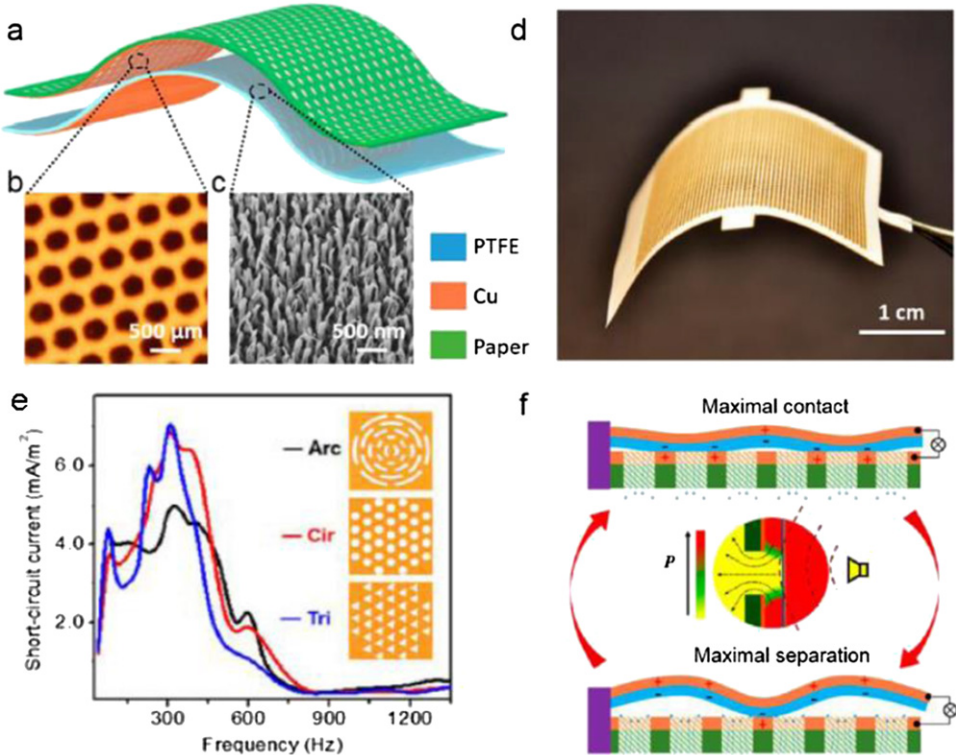


**Figure 50.** Structural design and operating principle of the ultrathin paper-based TENG for sonic wave detection. (a) Schematic illustrations of the paper-based TENG. (b) Photograph of the multihole paper electrode. (c) SEM image of the PTFE polymer nanowires. (d) Photograph of an as-fabricated paper-based TENG. (e) Influence of the hole shapes on the multihole electrode and the corresponding frequency response spectrum with constant void-to-surface ratio. (f) Illustration to interpret the sound wave-induced PTFE membrane vibration and electricity generation. Reprinted with permission from [198]. Copyright (2015) American Chemical Society.

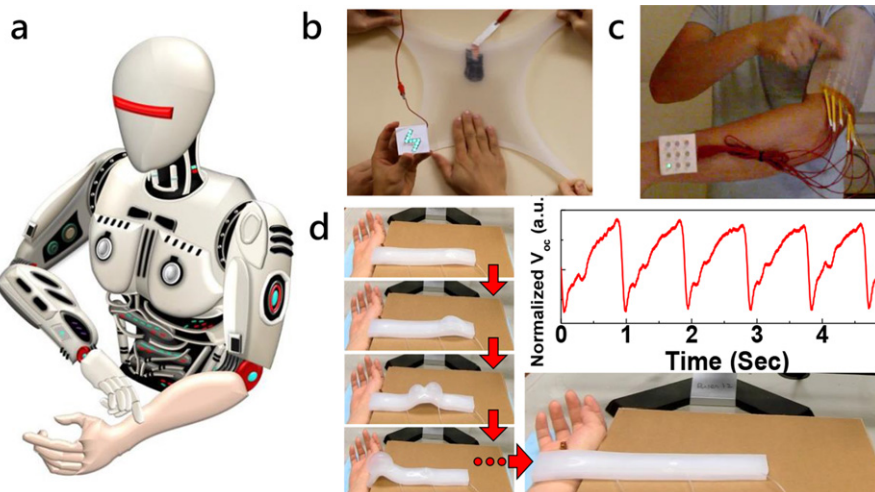


**Figure 51.** (a) Illustration of self-powered smart skin for robotics. (b) Demonstration of a superstretchable TENG-based self-powered smart skin at extremely omnidirectional stretching. (c) Demonstration of a large-area conformal self-powered smart skin system that can locate touch via visible signals. (d) Demonstration of a perceivable caterpillar-like soft robot crawling to a human wrist and feeling slight human pulses. [211] John Wiley & Sons. © 2018 WILEY-VCH Verlag GmbH & Co. KGaA, Weinheim.

only a device that converts sound waves into electric power, but also a self-powered sensor for security and smart homes [195, 199].

**5.2.4. Robotics.** Robotics will extensively change our life in many ways. To fully realize the potential of robotics, future

robots will require comprehensive sensory systems including vision, hearing, proprioceptive, and haptic sensing. However, the development of a skin-like sensory system for robots (i.e. robotic skin) is extremely challenging (figure 51(a)) [200]. The challenges mostly come from two aspects. First, there is a lack of deformable and stretchable sensors that can be conformably

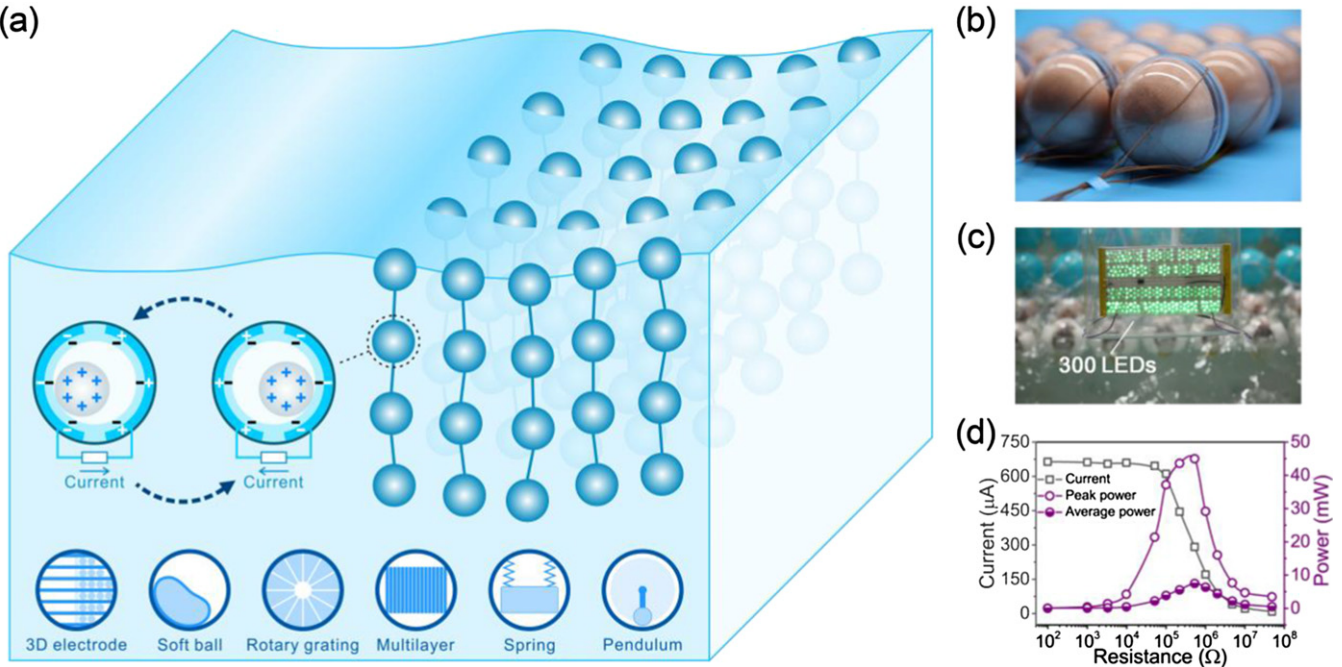


**Figure 52.** TENG network for harvesting blue energy. (a) Schematics of the TENG network for harvesting wave energy. The working mechanism of the ball-shell-structured device and schematics of TENG units based on 3D electrode structure, rotary grating disk structure, soft ball structure, multilayer structure, spring structure, and pendulum structure are also illustrated. Reprinted by permission from Springer Nature Customer Service Centre GmbH: *Nature*. [214] © 2017. Reprinted with permission from [216]. Copyright (2018) American Chemical Society. (b) Photograph of spherical TENG units [123]. (c) Directly powering light-emitting diodes (LEDs) by a TENG network in water waves. Reprinted from [217], Copyright (2019), with permission from Elsevier. (d) The output power of a rotary-grating-disk-structured TENG driven by water waves. Reprinted from [167], Copyright (2019), with permission from Elsevier.

and widely deployed on the robotic body. Second, the large amount of energy dissipation endlessly demanded by the passive sensing array severely hinders the applicability of conventional physical sensing technologies. Transducers based on conventional mechanisms (such as resistive/capacitive/optical ones) are passive devices, meaning that the operation of them requires additional and continuous electrical power. For a flexible passive sensor-like resistive/capacitive-type one, the device typically needs 1–10 V to function [201–204]. Correspondingly, for a large-area multiplexing passive sensing array, the driving voltage for each sensor and the huge amount of energy consumption will cause severe issues for it to serve as an independent system.

In recent years, a series of efforts have been made to develop TENG-based self-powered smart skins with various attributes and capabilities such as transparency [9, 205, 206], luminescence response [207], flexibility [208], stretchability [209], and self-healability [210]. Figure 51(b) shows a typical deformable and superstretchable TENG-based self-powered smart skin consisting of rubber as the triboelectric layer and embedded conducting nanowires as extensible electrodes. This TENG-based smart skin working in the single-electrode mode can produce electric signals in response to human touch. The working principle comes from the change in the electric field created by the triboelectric charges on the device surface during the contact/separation with human skin. This fact results in the flow of free electrons between the embedded electrode and the ground.

Figure 51(c) depicts a shape-adaptive and fully-autonomous  $3 \times 3$  multiplexing self-powered sensor array [170]. The smart skin system can locate a touch via visible light signal from the corresponding light-emitting diode (LED) without an external power source, and it can be conformably deployed on the surfaces of a desired object or human body. To realize the sensory skins for the soft robots that can provide safer and compliant interaction with humans is much more challenging, because of their continuously deforming actuators. The need for rigid and heavy power sources in passive sensing networks is a critical issue for soft robots. The exceptional merits of TENG self-powered smart skins enables soft robots to perceive external stimuli through a natural TE effect. Figure 51(d) presents a perceivable caterpillar-like soft robot with a TENG self-powered smart skin on its abdomen. The robot can move to a human hand and compliantly touch the wrist to feel weak human physiological signals, showing its potential for *in situ* palpation and healthcare.

Responding to external mechanical contact via the natural TE effect is intriguing. Competing passive physical sensing mechanisms require pre-provided continuous electric or optical signals. TENG-based smart skins can actively respond to mechanism stimuli via generating electricity from themselves. The self-generating electric signals cannot only be used for sensing and monitoring, but also directly power up optoelectronics for visible communication and be processed for diverse

sophisticated uses by a computing module. With these exceptional merits and extraordinary sensitivity, TENG-based smart skins are able to circumvent the problems in conventional tactile sensors and open a door for emerging technology ranging from human–machine interfaces and artificial intelligence to future robotics.

A self-powered angle sensor based on TENG has been developed as an angular sensor for robotics, due to its light weight, small size and high integrability. The sensor exhibits the highest resolution (2.03 nano-radian) and sensitivity (5.16 V/0.01°) as well as a great signal-to-noise ratio (98.68 dB) [212]. Such sensors will find important applications for joints and control systems in robotics.

### 5.3. Blue energy harvesting

Exploiting the tremendous energy from the ocean, such as wave energy, is an area for the TENG to play a vital role in contributing to the world's energy at large. The ocean covers more than 70% of the Earth's surface. Just the energy offered by the coastline worldwide would reach 75 TW. However, harvesting energy from such a vast area is hardly possible using traditional technologies. Owing to the physics limitations of EM generators, their efficiency is very low at low frequency. Together with their heavy weight and expensive materials for manufacturing, they are hardly useful for harvesting water wave energy over a large area. The TENG and its network can provide a revolutionary approach to effectively harvest the low-frequency ocean blue energy for electricity, which was first proposed by Wang [213]. By forming a networks of TENGs that float on the surface of water, an effective energy harvest from the ocean can be constructed [214], as shown in figure 52. Each unit is a highly efficient TENG that works to harvest low-frequency and random direction mechanical energy. The most typical design is adopting an enclosed ball-shell structure rolling in water waves [215, 216]. The static charges on the rolling inner ball can induce charge transfer between the two hemispherical electrodes through an external circuit and output electricity. For boosting the output of a single device, a 3D electrode structure with small intercalated pellets [217], rotary grating disk structure [167], soft ball with improved contact [218], and multilayer structure [219] can be applied. Elastic spring [220] and pendulum [131] structures can also be adopted for improving the dynamic response to water waves. An average power density of  $7.3 \text{ W m}^{-3}$  is achieved for water waves [167]. Although the output from each unit is an AC output, a rectification using diodes would allow them to add up constructively. Considering that the materials used for fabricating the TENG are mainly organic materials, the networks on the surface can float. Such a design would work regardless of the depth of the water. It is important to mention that the TENG arrays can be built vertically into the water to form a 3D grid, so that the energy in volume can be harvested, which could largely improve the output power.

Energy harvested from water can be used locally for various purposes, such as self-powered electrochemistry for anti-corrosion and antifouling [221, 222], water splitting [223], and water desalination [224]. Such distributed energy will be

important for the future. By relieving the restriction of electrical power supply, the TENG can provide a solid foundation for exploiting the resources of the ocean. The electricity from large-scale harvesting can also be transmitted through cables to islands or power grids on the land, which can serve millions of people as a promising clean energy source.

### 5.4. As highvoltage sources

One of the most typical characteristics of TENGs is their high output voltage, which can be used for a number of purposes such as excitation of plasma, electrospinning of fibers, and particle filtering etc. The traditional plasma is generally produced by precision instruments, which are large and expensive, to supply a high voltage and control the gas pressure, which severely limits its general applications. Recently, Cheng *et al* [225] have proposed the concept of microplasma by using the high voltage of a TENG to discharge the gas. As the electrons accelerated by the electric field collide with the neutral gas molecules, the molecules are ionized to break down the gas under the avalanche effect, producing the microplasma consisting of lots of electrons and ions (figure 53(a)). As shown in figures 53(b)–(g) and to be discussed in detail below, the triboelectric microplasma has been introduced to build up novel sensing systems due to its facile and portable characters, such as the self-powered photon and gas sensors, and the sensing system with *in situ* floating gas ionic gate and *in situ* surface passivation, etc.

The electrical properties of the triboelectric microplasma are sensitive to its working conditions, such as light illumination and gas species (figure 53(b)). For example, as the UV light illumination is applied, the extra electrons and positive ions can be generated, which reduces the threshold voltage for producing the microplasma. Conversely, as the gas with stronger electronegativity, such as  $\text{CO}_2$ , is added into the atmosphere, more negative ions will be generated and will recombine with the positive ions in the microplasma, which increases the threshold voltage for producing the microplasma. The variations of the threshold voltage of microplasma change the output current of the TENG, which can be utilized to fabricate the self-powered sensors. In a self-powered UV photodetector reported by Cheng *et al* [226], a sensitivity of 18.2 is obtained for a UV light with a central wavelength and light intensity of 365 nm and  $26.2 \mu\text{W cm}^{-2}$ . In a self-powered gas sensor for  $\text{CO}_2$ , reported by Zhao *et al* [227], as the added  $\text{CO}_2$  reaches a threshold concentration, the threshold voltage of the microplasma is higher than the OC voltage of the TENG, causing the microplasma to disappear (figure 53(c)). The detectable threshold concentration of  $\text{CO}_2$  ranging from 1000 to 200 000 ppm can be tuned by the tip-plate distance.

In semiconductor sensor devices, the surface properties of the semiconductors play a key role in the performances of the sensors. For *in situ* tuning of the surface of sensors, the triboelectric microplasma has been combined with the sensor to form a sensing system, which provides a powerful technology for developing novel sensors with enhanced performance. First, the floating gas ionic gate technology has been proposed by Yang *et al* [228] and Zhao *et al* [229], in which the  $\text{O}_2^-$

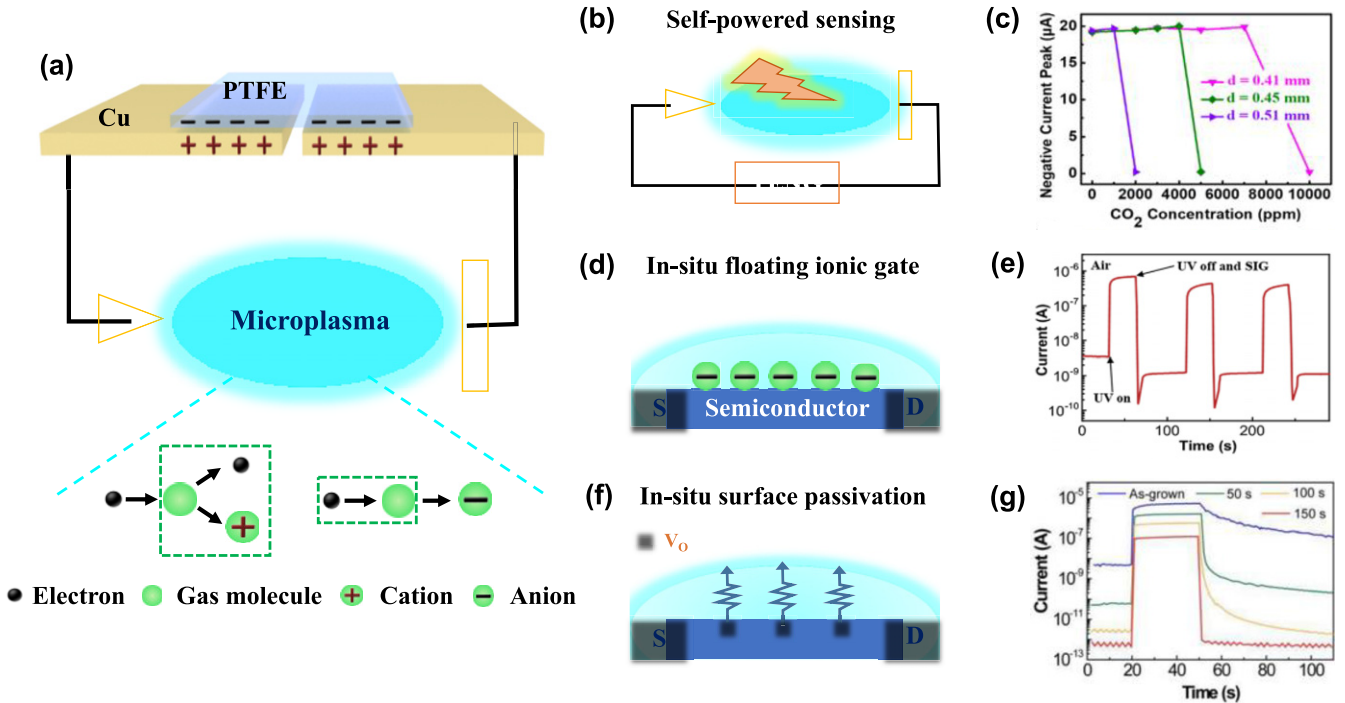


**Figure 53.** (a) Diagram of the triboelectric microplasma powered by a TENG. (b) Diagram of the microplasma-based self-powered sensing system, and (c) the current curves as detecting CO<sub>2</sub> gas. (d) Diagram of the microplasma-based sensing system with *in situ* floating ionic gate, and (e) the UV photo sensing curves of a ZnO nanowire with the floating gate. Reprinted from [228], Copyright (2019), with permission from Elsevier. (f) The diagram of the microplasma-based sensing system with *in situ* surface passivation, and (g) the UV photo sensing curves of a ZnO nanowire as oxygen vacancies ( $V_O$ ) are *in situ* passivated. Reprinted from [239], Copyright (2020), with permission from Elsevier.

ions produced in the microplasma are adsorbed on semiconductor surfaces to act as a floating gate (figure 53(d)). In a ZnO nanowire Schottky diode [228], the floating gate of O<sub>2</sub><sup>-</sup> lowers the Fermi level of the ZnO nanowire, increasing the barrier height and reducing the current. Also, due to the fast adsorption behavior of the O<sub>2</sub><sup>-</sup> ions, the fast UV photodetector of the ZnO nanowire UV photodetector has been achieved, and the photocurrent recovery speed is improved by 290 times (figure 53(e)). In the photodetector of monolayer MoS<sub>2</sub> [229], it is found that the floating ionic gate of O<sub>2</sub><sup>-</sup> changes the surface local electronic state and the dynamic process for capturing photo-generated carriers, which make the photocurrent increased linearly with time.

In addition, the triboelectric microplasma has been utilized by Yang *et al* [230] as an *in situ* surface passivation technology in a ZnO nanowire UV photodetector. It has been reported that the oxygen vacancies on a ZnO nanowire device can be passivated *in situ* by the oxygen ions in the microplasma, and a quantitative tuning can be achieved by controlling the exposure time of the microplasma (figure 53(f)). As the concentration of oxygen vacancies is gradually reduced, the photocurrent is reduced, however, the recovery speed is largely increased (figure 53(g)). As a result, the *GB* product (the product of photocurrent gain and bandwidth), a key index reflecting the comprehensive performance of photodetectors, can be improved by 2500 times. These results indicate that the life of the photo-generated holes is largely

determined by the concentration of oxygen vacancies, which can be tuned *in situ* by the microplasma surface passivation technology.

The triboelectric microplasma can be generated in atmospheric pressure and various gas environments, such as air, O<sub>2</sub>, N<sub>2</sub>, Ar, H<sub>2</sub>, CO<sub>2</sub> etc. In addition, as the parameters of the microplasma, such as distance between electrodes, diameter of electrodes etc, are tuned, various modes of microplasma have been realized, including dielectric barrier discharge, corona discharge, and microspark discharge, etc [225, 226]. The triboelectric microplasma provides a promising supplement to the traditional plasma, especially in the fields where plasma sources with small size and low cost are required. Due to its advantages of safety, simplicity, portability, and no need for an external power source, the triboelectric microplasma has potential applications in constructing novel sensors of the internet of things.

##### 5.5. As scanning probe for measuring interface charges

A single-electrode TENG can be a ‘probe’ for measuring the charge transfer at a liquid–solid interface. Recently, the charge-transfer mechanism at the liquid–solid interface was verified as the hybrid effects of electron transfer and ion adsorption by a simple but valid method [231]. Thus, a model for the charge distribution at the liquid–solid interface is proposed, named Wang’s hybrid layer, which involves the elec-

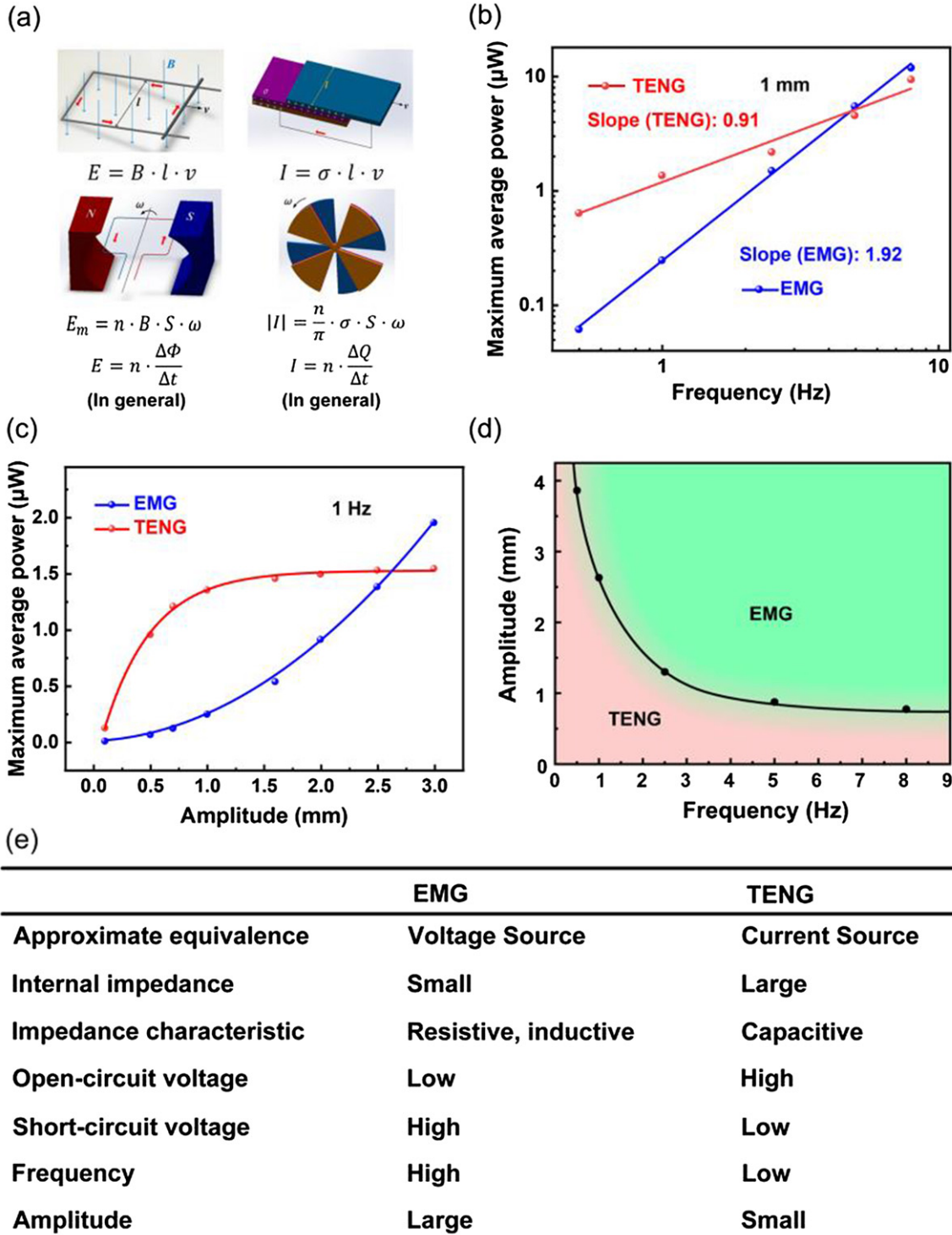


**Figure 54.** A comparison of fundamental principles and mechanical energy harvesting characteristics between EMG and TENG. (a) Governing equations. (b) Working frequency. (c) Motion amplitude. (d) Dominant scopes. (e) Overall comparison summary.

tron transfer, the ionization reaction and the van der Waals force. This work may have great significance to water energy harvesting, and may revolutionize the traditional understanding of the liquid–solid interface used in many fields such as electrochemistry, catalysis, colloidal science and even cell biology.

A new technique for local surface charge density measurement based on atomic force microscopy has also been pro-

posed [232]. It is named scanning TENG, in which a conductive tip tapping above a charged dielectric surface produces an AC current between the tip and the dielectric bottom electrode due to electrostatic induction. The Fourier analysis shows that the amplitude of the first harmonic of the AC current is linearly related to the surface charge density. The results demonstrate that the scanning TENG is a powerful tool for probing nano-scale charge transfer in CE.

## 5.6. Hybridized NGs

As shown in figure 26, there are two fundamental approaches for converting mechanical energy into electric power: one is the EMG that relies on the conduction current; and the other is the TENG that utilizes the displacement current. A comparison of the two was first given by Zhang *et al* [233]. EMG can be considered as a voltage source, while TENG is considered as a current source. Figure 54(b) shows the average power density of two generators vs working frequency, which indicates that TENG has shown a much better performance than that of the EMG at low frequency (typically  $<5$  Hz) [114]. The maximum average power of two generators at 1 Hz with different amplitudes is exhibited in figure 54(c), which demonstrates that, at small amplitude (typically  $<2.5$  mm), the TENG has a much better performance than that of the EMG [234].

Figure 54(d) summarizes the amplitudes in crossover points of both maximum average output power characteristic curves at different frequencies. The fitted line divides the figure into two areas; the dominant scope of TENG is denoted in the light red area, while the EMG is in the light green area. The lower the frequency, the larger the advantage range of TENG is; thus, the dominant scope of TENG over the EMG is at both low-frequency and small amplitude. Furthermore, figure 54(e) summarizes an overall comparison of EMG and TENG. In short, for the theoretical characteristics, the EMG can be regarded as a voltage source with a small impedance in resistive and inductive characteristics, while the TENG is approximately a current source with a large capacitive impedance. So, the EMG shows a low OC voltage but a high SC current, while the TENG has a low SC current but a high OC voltage. For energy-harvesting characteristics, the EMG has a better performance in high frequency and large amplitude, but TENG is more suitable for low frequency and small amplitude. Therefore, TENG and EMG have complementarity; the killer applications of TENG are for low-frequency and small-amplitude mechanical energy harvesting.

EMG and TENG have been hybridized to effectively harvest all kinds of mechanical energy. To scavenge vibration energy, a double-layer structural hybridized NG was designed for harvesting vibrational energy [235]. As illustrated in figure 55(a), a coil and a magnet were respectively attached to two separated acrylic substrates that were supported by four springs. The peak output powers and corresponding power densities of EMG and TENG were  $3.5\text{ mW}/3.6\text{ W m}^{-2}$  and  $4.9\text{ mW}/5.1\text{ W m}^{-2}$ , respectively. By putting the hybrid device into the heel position of a shoe, the biomechanical vibration energy from a human walking can be efficiently harvested for powering 20 red LEDs. Moreover, researchers reported a hybridized NG consisting of a TENG with a single electrode and an EMG (figure 55(b)) [236], which can simultaneously generate triboelectric and EM electricity from one mechanical vibration operation. In the working process, the TENG can produce the output voltage/current/power of about  $600\text{ V}/3.5\text{ }\mu\text{A}/0.25\text{ mW}$ . For EMG, it can produce voltage/current/power of about  $3\text{ V}/1\text{ mA}/0.58\text{ mW}$ . Both the

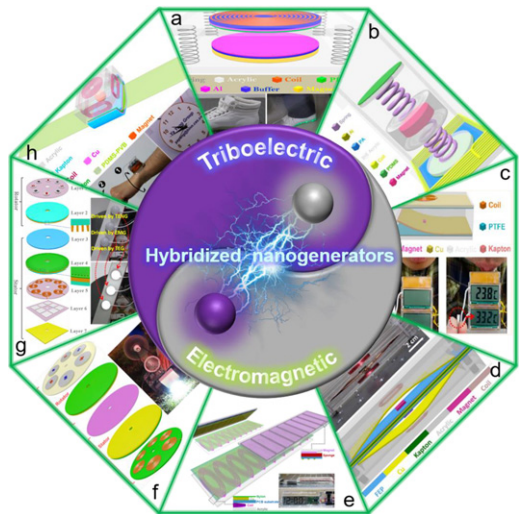


**Figure 55.** Various hybridized NGs for scavenging mechanical energy. (a) Structure diagram of a hybrid NG for powering several LEDs by scavenging vibration energy from human motions. (b) Structure diagram of a hybridized NG. (c) Hybridized NG where one side was fixed for powering temperature sensors by scavenging air-flow energy induced by human breath blowing. (d) Photograph and corresponding structure diagram of a fabricated hybridized NG for wind energy scavenging. (e) Structure diagram of a hybridized NG with a linear-grating structure for powering portable electronics by scavenging sliding energy. (f) Structure diagram of a hybridized NG for harvesting rotational energy to power a globe light. (g) Hybridized NG for rotational energy scavenging, and three globe lights were directly powered by the EMG, TENG and thermoelectric generators (TEG) respectively. (h) A hybrid NG for harvesting biocompatible energy from human wrist motion.

TENG and EMG can directly power dozens of parallel-connected LEDs.

Researchers designed a single-side fixed hybridized NG by using two EMGs and two TENGs [237], as displayed in figure 55(c). By scavenging the vibration energy of Kapton film induced by air flow (speed:  $18\text{ m s}^{-1}$ ), one TENG and one EMG can respectively generate  $3.5$  and  $1.8\text{ mW}$  as the maximum output power. The hybridized device can drive two temperature sensors through harvesting air-flow energy from human breath blowing. Additionally, a hybridized EM-trioelectric NG with two sides fixed was fabricated for scavenging wind energy, as presented in figure 55(d) [238]. The hybrid NG can output the maximum powers of  $1.7/2.5\text{ mW}$  for TENG/EMG by harvesting wind energy with a speed of  $18\text{ m s}^{-1}$ , showing huge application potential in self-powered sensing systems. Figure 55(e) illustrates a hybridized NG with a linear-grating structure [239]. A 66-segment TENG and nine-segment EMG fabricated the hybridized NG that can sustainably drive portable electronics by scavenging mechanical energy with low frequency from sliding motion. At a sliding acceleration of  $20\text{ m s}^{-2}$ ,  $102.8\text{ mW}$  and  $103.3\text{ mW}$  as output powers can be obtained by the TENG and EMG, respectively.

As one kind of mechanical energy, rotational energy is important and widespread in daily life. Researchers fabricated a rotating-disk-structured hybridized NG to scavenge mechanical rotation energy by simultaneously utilizing a TENG and

an EMG [240] as presented in figure 55(f). When the rotating rate was kept at 200 r/min, the generated powers of 8.6 and 8.4 mW can be obtained by the TENG and EMG, respectively. The fabricated hybridized NG exhibits better output power as compared with that of individual devices. As we know, during the rotating-disk working process of rotator and stator, thermal energy will be produced at interfaces of the TENG. To efficiently harvest thermal energy, several TENGs were integrated into the hybridized NG, as exhibited in figure 55(g) [241]. By the coupling effect of TENG, EMG and TENG, the hybridized device can output a constant voltage/pulsed current of 5 V/160 mA with the help of a power management circuit. By installing the device in a bicycle, three globe lights can be powered by scavenging mechanical energy from riding a bicycle. Except scavenging mechanical energy from a single motion mentioned above, researchers further fabricated a watch-like hybridized NG [242], as exhibited in figure 55(h). The device consists of two parts, an acrylic box that contains a magnetic ball and a coil in each side forming the EMG, a nylon film and PVB/PDMS composite forming a TENG. It is worth noting that the PVB/PDMS film acts as the triboelectric material and watch belt. By scavenging biomechanical energy from the random motion of a human wrist, the generated electricity of the hybridized NG was stored in a capacitor ( $100 \mu\text{F}$ ) for 39 s and can sustainably power an electronic watch for more than 7 min, pushing the potential development of portable and self-powered electronics by scavenging biomechanical energy with the help of hybridized EM-TENGs. Hybridization can also be extended to TENGs with a solar cell, and TENGs with a piezoelectric energy harvester [243, 244].

Besides hybridization of EMGs and TENGs, a TENG has been hybridized with solar cells for harvesting energy from both mechanical triggering and light, so that the energy can be collected using whatever is possible and whenever is available to meet the power requirements [161, 245].

## 6. Summary

This review covers the fundamental physics of the CE and the expanded Maxwell equations for the theory of TENGs, and the related technological applications of TENGs. The objectives are intended to not only answer some fundamental science questions about CE, but also present the practical impacts of TENGs:

- (a) The mechanism of CE between solid–solid, liquid–solid and liquid–liquid. The solids cover general polymer materials, ceramics, semiconductors and metals. The liquids cover water and its solution with different pH values. Our general conclusion is that the electron transfer is dominant between solid–solid CE. The CE between liquid–solid has both electron and ion transfers. A two-step model is introduced to revise the traditional mechanism about the formation of electric double layers, which is expected to have a broad impact on electrochemistry and interface science.
- (b) The theory for using the time-dependent field generated by surface electrostatic charges due to CE for convert-

ing mechanical triggering into electric power. By introducing a non-electric field-induced polarization term  $\mathbf{P}_s$  in Maxwell's equations, a systematic theory has been derived for describing the EM dynamics of NGs from the first principle point of view, from which the output of NGs can be quantified. Furthermore, the EM radiation from NG systems can be calculated, which may be observable if the operation frequency is high. This innovative extension of  $\mathbf{P}_s$  in the displacement vector  $\mathbf{D}$  opens the applications of Maxwell's equations in energy and sensors. With the establishment of this general theory, we anticipate that it will serve as the theoretical foundation for advancing the science, technology and even applications of NGs in energy and sensors.

- (c) The fundamentals and standards for quantifying the surface charge density for a general material are established. Various strategies for enhancing the surface charge density are presented, which are important for improve the performance of TENGs.
- (d) The major technological applications of TENGs are reviewed, so that our fundamental studies about CE can inspire new discoveries about unprecedented technologies for energy and sensors. Therefore, CE and TENGs are an ideal system that has not only the most important fundamental science, but also the most advanced technological applications.

A comprehensive review about the contact electrification between liquid and solid has been published [246], which concludes that electron transfer is the dominant process for CE at liquid-solid interfaces. Recent study of the contact electrification between water and oil droplet shows that electrons transfer is most likely to be the dominant charge transfer process [247]. Recent studies have also shown that TENG can be a probe for measuring the charge density on a surface [248].

## Acknowledgments

I like to thank many of my former and current group members and collaborators who have made the key contributions to the fundamentals and technological demonstrations of TENGs. Some of the figures used in the review were provided (in no particular order) by Drs Cheng Xu, Shengming Li, Yusheng Zhou, Shiquan Lin, Xiangyu Chen, Peng Jiang, Chi Zhang, Qing Zhang, Haiyang Zou, Sang-Woo Kim, Jeong-Min Baik, Jiajia Sha, Xiangyu Chen, Gang Chen, Kai Dong, Hengy Guo, Chenguo Hu, Jin Yang, Shiquan Lin, Morten Willatzen, Xiong Pu, Yong Qin, Yunlong Zi, Renyun Zhang, Liang Xu, Ya Yang, Ying-Chih Lai, and Zhiyi Wu, to whom I would like to extend my sincere thanks. Thank you to Ms Mohan Chen and Lin Wang for assistance.

## Data availability statement

The data that support the findings of this study are available upon reasonable request from the authors.

## ORCID iDs

Zhong Lin Wang  <https://orcid.org/0000-0002-5530-0380>

## References

- [1] Shaw P E 1926 The electrical charges from like solids *Nature* **118** 659–60
- [2] Lacks D J and Shinbrot T 2019 Long-standing and unresolved issues in triboelectric charging *Nat. Rev. Chem.* **3** 465–76
- [3] Terris B D, Stern J E, Rugar D and Mamin H J 1989 Contact electrification using force microscopy *Phys. Rev. Lett.* **63** 2669
- [4] Pingali K C, Hammond S V, Muzzio F J and Shinbrot T 2009 Use of a static eliminator to improve powder flow *Int. J. Pharm.* **369** 2–4
- [5] Salama F, Sowinski A, Atieh K and Mehrani P 2013 Investigation of electrostatic charge distribution within the reactor wall fouling and bulk regions of a gas–solid fluidized bed *J. Electrost.* **71** 21–7
- [6] Pu Y, Mazumder M and Cooney C 2009 Effects of electrostatic charging on pharmaceutical powder blending homogeneity *J. Pharm. Sci.* **98** 2412–21
- [7] Burgo T A L, Silva C A, Balestrin L B S and Galembek F 2013 Friction coefficient dependence on electrostatic tribocharging *Sci. Rep.* **3** 2384
- [8] Sayfidinov K, Cezan S D, Baytekin B and Baytekin H T 2018 Minimizing friction, wear, and energy losses by eliminating contact charging *Sci. Adv.* **4** eaau3808
- [9] Fan F-R, Lin L, Zhu G, Wu W, Zhang R and Wang Z L 2012 Transparent triboelectric nanogenerators and self-powered pressure sensors based on micropatterned plastic films *Nano Lett.* **12** 3109–14
- [10] Wang Z L, Lin L, Chen J, Niu S and Zi Y 2016 *Triboelectric Nanogenerators* (Berlin: Springer)
- [11] Wang Z L 2013 Triboelectric nanogenerators as new energy technology for self-powered systems and as active mechanical and chemical sensors *ACS Nano* **7** 9533–57
- [12] Wang Z L, Chen J and Lin L 2015 Progress in triboelectric nanogenerators as a new energy technology and self-powered sensors *Energy Environ. Sci.* **8** 2250–82
- [13] Liu C-y. and Bard A J 2009 Electrons on dielectrics and contact electrification *Chem. Phys. Lett.* **480** 145–56
- [14] Harper W R 1967 *Contact and Frictional Electrification* (Oxford: Clarendon)
- [15] McCarty L S and Whitesides G M 2008 Electrostatic charging due to separation of ions at interfaces: contact electrification of ionic electrets *Angew. Chem., Int. Ed.* **47** 2188–207
- [16] Diaz A F, Wollmann D and Dreblow D 1991 Contact electrification: ion transfer to metals and polymers *Chem. Mater.* **3** 997–9
- [17] Lowell J 1977 The role of material transfer in contact electrification *J. Phys. D: Appl. Phys.* **10** L233
- [18] Knoblauch O 1902 Versuche über die Berührungslektrizität *Z. Phys. Chem.* **39U** 225–44
- [19] Fu R, Shen X and Lacks D J 2017 First-principles study of the charge distributions in water confined between dissimilar surfaces and implications in regard to contact electrification *J. Phys. Chem. C* **121** 12345–9
- [20] McCarty L S, Winkleman A and Whitesides G M 2007 Electrostatic self-assembly of polystyrene microspheres by using chemically directed contact electrification *Angew. Chem., Int. Ed.* **46** 206–9
- [21] Lin S-q and Shao T-m 2017 Bipolar charge transfer induced by water: experimental and first-principles studies *Phys. Chem. Chem. Phys.* **19** 29418–23
- [22] Burgo T A d L, Rezende C A, Bertazzo S, Galembek A and Galembek F 2011 Electric potential decay on polyethylene: role of atmospheric water on electric charge build-up and dissipation *J. Electrost.* **69** 401–9
- [23] Nguyen V and Yang R 2013 Effect of humidity and pressure on the triboelectric nanogenerator *Nano Energy* **2** 604–8
- [24] Baytekin H T, Baytekin B, Soh S and Grzybowski B A 2011 Is water necessary for contact electrification? *Angew. Chem.* **123** 6898–902
- [25] Xu C *et al* 2018 On the electron-transfer mechanism in the contact-electrification effect *Adv. Mater.* **30** 1706790
- [26] Wang J, Wu C, Dai Y, Zhao Z, Wang A, Zhang T and Wang Z L 2017 Achieving ultrahigh triboelectric charge density for efficient energy harvesting *Nat. Commun.* **8** 1–8
- [27] Liu J *et al* 2018 Sustained electron tunneling at unbiased metal–insulator–semiconductor triboelectric contacts *Nano Energy* **48** 320–6
- [28] Wang Z L 2020 Triboelectric nanogenerator (TENG)-Sparking an energy and sensor revolution *Adv. Energy Mater.* **10** 2000137
- [29] Wang Z L and Wang A C 2019 On the origin of contact-electrification *Mater. Today* **30** 34–51
- [30] Zhou Y S, Liu Y, Zhu G, Lin Z-H, Pan C, Jing Q and Wang Z L 2013 *In situ* quantitative study of nanoscale triboelectrification and patterning *Nano Lett.* **13** 2771–6
- [31] Zhou Y S, Wang S, Yang Y, Zhu G, Niu S, Lin Z-H, Liu Y and Wang Z L 2014 Manipulating nanoscale contact electrification by an applied electric field *Nano Lett.* **14** 1567–72
- [32] Lowell J and Akande A R 1988 Contact electrification—why is it variable? *J. Phys. D: Appl. Phys.* **21** 125
- [33] Lee L-H 1994 Dual mechanism for metal–polymer contact electrification *J. Electrost.* **32** 1–29
- [34] Vick F A 1953 Theory of contact electrification *Br. J. Appl. Phys.* **4** S1
- [35] Liu J *et al* 2018 Direct-current triboelectricity generation by a sliding Schottky nanocontact on MoS<sub>2</sub> multilayers *Nat. Nanotechnol.* **13** 112–6
- [36] Huang S M, Atanasoski R T and Oriani R A 1993 Detection of effects of low electric fields with the Kelvin probe *J. Electrochem. Soc.* **140** 1065
- [37] Verdaguer A, Cardellach M, Segura J J, Sacha G M, Moser J, Zdrojek M, Bachtold A and Fraxedas J 2009 Charging and discharging of graphene in ambient conditions studied with scanning probe microscopy *Appl. Phys. Lett.* **94** 233105
- [38] Nguyen M T, Kanazawa K K, Brock P, Diaz A F and Yee S 1994 Surface potential map of charged ionomer–polymer blends studied with a scanning Kelvin probe *Langmuir* **10** 597–601
- [39] Sun H, Chu H, Wang J, Ding L and Li Y 2010 Kelvin probe force microscopy study on nanotriboelectrification *Appl. Phys. Lett.* **96** 083112
- [40] Lin S *et al* 2019 Electron transfer in nanoscale contact electrification: effect of temperature in the metal–dielectric case *Adv. Mater.* **31** 1808197
- [41] Lin S, Xu L, Zhu L, Chen X and Wang Z L 2019 Electron transfer in nanoscale contact electrification: photon excitation effect *Adv. Mater.* **31** 1901418
- [42] Lee J W *et al* 2019 High-output triboelectric nanogenerator based on dual inductive and resonance effects-controlled highly transparent polyimide for self-powered sensor network systems *Adv. Energy Mater.* **9** 1901987
- [43] Lin S, Lu Y, Feng S, Hao Z and Yan Y 2019 A high current density direct-current generator based on a moving van der Waals Schottky diode *Adv. Mater.* **31** 1804398
- [44] Horn R G and Smith D T 1992 Contact electrification and adhesion between dissimilar materials *Science* **256** 362–4

- [45] Zhang Z, Jiang D, Zhao J, Liu G, Bu T, Zhang C and Wang Z L 2020 Tribovoltaic effect on metal–semiconductor interface for direct-current low-impedance triboelectric nanogenerators *Adv. Energy Mater.* **10** 1903713
- [46] Zheng M, Lin S, Tang Z, Feng Y and Wang Z L 2021 Photovoltaic effect and tribovoltaic effect at liquid–semiconductor interface *Nano Energy* **83** 105810
- [47] Zhang Q, Xu R and Cai W 2018 Pumping electrons from chemical potential difference *Nano Energy* **51** 698–703
- [48] Lin S, Chen X and Wang Z L 2020 The tribovoltaic effect and electron transfer at a liquid–semiconductor interface *Nano Energy* **76** 105070
- [49] Xu R, Zhang Q, Wang J Y, Liu D, Wang J and Wang Z L 2019 Direct current triboelectric cell by sliding an n-type semiconductor on a p-type semiconductor *Nano Energy* **66** 104185
- [50] Castle G S P and Schein L B 1995 General model of sphere-sphere insulator contact electrification *J. Electrost.* **36** 165–73
- [51] Schein L B, LaHa M and Novotny D 1992 Theory of insulator charging *Phys. Lett. A* **167** 79–83
- [52] Li S, Zhou Y, Zi Y, Zhang G and Wang Z L 2016 Excluding contact electrification in surface potential measurement using kelvin probe force microscopy *ACS Nano* **10** 2528–35
- [53] Xu C *et al* 2018 Raising the working temperature of a triboelectric nanogenerator by quenching down electron thermionic emission in contact-electrification *Adv. Mater.* **30** 1803968
- [54] Li D, Xu C, Liao Y, Cai W, Zhu Y and Wang Z L Interface inter-atomic electron-transition induced photon emission in contact-electrification *Sci. Adv.* (submitted)
- [55] Stöcker H, Rühl M, Heinrich A, Mehner E and Meyer D C 2013 Generation of hard x-ray radiation using the triboelectric effect by peeling adhesive tape *J. Electrost.* **71** 905–9
- [56] Camara C G, Escobar J V, Hird J R and Putterman S J 2008 Correlation between nanosecond x-ray flashes and stick-slip friction in peeling tape *Nature* **455** 1089–92
- [57] Willatzen M and Wang Z L 2018 Theory of contact electrification: optical transitions in two-level systems *Nano Energy* **52** 517–23
- [58] Willatzen M and Wang Z L 2019 Contact electrification by quantum-mechanical tunneling *Research* **2019** 6528689
- [59] Willatzen M, Lew Yan Voon L C and Wang Z L 2020 Quantum theory of contact electrification for fluids and solids *Adv. Funct. Mater.* **30** 1910461
- [60] Shen X, Wang A E, Sankaran R M and Lacks D J 2016 First-principles calculation of contact electrification and validation by experiment *J. Electrost.* **82** 11–6
- [61] Apodaca M M, Wesson P J, Bishop K J M, Ratner M A and Grzybowski B A 2010 Contact electrification between identical materials *Angew. Chem., Int. Ed.* **49** 946–9
- [62] Zhao H, Castle G S P, Inculet I I and Bailey A G 2003 Bipolar charging of poly-disperse polymer powders in fluidized beds *IEEE Trans. Ind. Appl.* **39** 612–8
- [63] Forward K M, Lacks D J and Sankaran R M 2009 Charge segregation depends on particle size in triboelectrically charged granular materials *Phys. Rev. Lett.* **102** 028001
- [64] Xu C *et al* 2019 Contact-electrification between two identical materials: curvature effect *ACS Nano* **13** 2034–41
- [65] Makov G and Nitzan A 1993 Electronic properties of finite metallic systems *Phys. Rev. B* **47** 2301
- [66] Baytekin H T, Patashinski A Z, Branicki M, Baytekin B, Soh S and Grzybowski B A 2011 The mosaic of surface charge in contact electrification *Science* **333** 308–12
- [67] Mizzi C A, Lin A Y W and Marks L D 2019 Does flexoelectricity drive triboelectricity? *Phys. Rev. Lett.* **123** 116103
- [68] Lin S, Xu L, Wang A C and Wang Z L 2020 Quantifying electron-transfer in liquid–solid contact electrification and the formation of electric double-layer *Nat. Commun.* **11** 1–8
- [69] Nie J, Ren Z, Xu L, Lin S, Zhan F, Chen X and Wang Z L 2020 Probing contact-electrification-induced electron and ion transfers at a liquid–solid interface *Adv. Mater.* **32** 1905696
- [70] Li S, Nie J, Shi Y, Tao X, Wang F, Tian J, Lin S, Chen X and Wang Z L 2020 Contributions of different functional groups to contact electrification of polymers *Adv. Mater.* **32** 2001307
- [71] Loh Z-H *et al* 2020 Observation of the fastest chemical processes in the radiolysis of water *Science* **367** 179–82
- [72] Jiang P, Zhang L, Guo H, Chen C, Wu C, Zhang S and Wang Z L 2019 Signal output of triboelectric nanogenerator at oil–water–solid multiphase interfaces and its application for dual-signal chemical sensing *Adv. Mater.* **31** 1902793
- [73] Dickinson W 1941 The effect of pH upon the electrophoretic mobility of emulsions of certain hydrocarbons and aliphatic halides *Trans. Faraday Soc.* **37** 140–8
- [74] Beattie J K, Djerdjev A M and Warr G G 2009 The surface of neat water is basic *Faraday Discuss.* **141** 31–9
- [75] Marinova K G, Alargova R G, Denkov N D, Velev O D, Petsev D N, Ivanov I B and Borwankar R P 1996 Charging of oil–water interfaces due to spontaneous adsorption of hydroxyl ions *Langmuir* **12** 2045–51
- [76] Nie J, Wang Z, Ren Z, Li S, Chen X and Wang Z L 2019 Power generation from the interaction of a liquid droplet and a liquid membrane *Nat. Commun.* **10** 1–10
- [77] Tang Z, Lin S and Wang Z L Quantifying contact-electrification induced charge transfer on a liquid droplet after contacting with a liquid or solid submitted
- [78] Zhao X, Lu X, Zheng Q, Fang L, Zheng L, Chen X and Wang Z L 2021 Studying of contact electrification and electron transfer at liquid–liquid interface *Nano Energy* **87** 106191
- [79] Crowell C R 1965 The Richardson constant for thermionic emission in Schottky barrier diodes *Solid-State Electron.* **8** 395–9
- [80] Racko J, Grmanová A and Breza J 1996 Extended thermionic emission-diffusion theory of charge transport through a Schottky diode *Solid-State Electron.* **39** 391–7
- [81] Zou H *et al* 2019 Quantifying the triboelectric series *Nat. Commun.* **10** 1–9
- [82] Zou H *et al* 2020 Quantifying and understanding the triboelectric series of inorganic non-metallic materials *Nat. Commun.* **11** 1–7
- [83] Seol M *et al* 2018 Triboelectric series of 2D layered materials *Adv. Mater.* **30** 1801210
- [84] Wang Z L and Song J 2006 Piezoelectric nanogenerators based on zinc oxide nanowire arrays *Science* **312** 242–6
- [85] Wang Z L 2019 Entropy theory of distributed energy for internet of things *Nano Energy* **58** 669–72
- [86] Wang Z L 2017 On Maxwell’s displacement current for energy and sensors: the origin of nanogenerators *Mater. Today* **20** 74–82
- [87] Wang Z L, Jiang T and Xu L 2017 Toward the blue energy dream by triboelectric nanogenerator networks *Nano Energy* **39** 9–23
- [88] Jackson J D 1998 *Classical Electrodynamics* 3rd edn (New York: Wiley)
- [89] Stratton J A 1941 *Electromagnetic Theory* (New York: McGraw-Hill)
- [90] Essex E A 1977 Hertz vector potentials of electromagnetic theory *Am. J. Phys.* **45** 1099–101
- [91] Fan F-R, Tian Z-Q and Lin Wang Z 2012 Flexible triboelectric generator *Nano Energy* **1** 328–34
- [92] Zhu G, Lin Z-H, Jing Q, Bai P, Pan C, Yang Y, Zhou Y and Wang Z L 2013 Toward large-scale energy harvesting by a nanoparticle-enhanced triboelectric nanogenerator *Nano Lett.* **13** 847–53

- [93] Yang Y, Zhang H, Chen J, Jing Q, Zhou Y S, Wen X and Wang Z L 2013 Single-electrode-based sliding triboelectric nanogenerator for self-powered displacement vector sensor system *ACS Nano* **7** 7342–51
- [94] Wang S, Xie Y, Niu S, Lin L and Wang Z L 2014 Freestanding triboelectric-layer-based nanogenerators for harvesting energy from a moving object or human motion in contact and non-contact modes *Adv. Mater.* **26** 2818–24
- [95] Wu C, Wang A C, Ding W, Guo H and Wang Z L 2019 Triboelectric nanogenerator: a foundation of the energy for the new era *Adv. Energy Mater.* **9** 1802906
- [96] Niu S, Wang S, Lin L, Liu Y, Zhou Y S, Hu Y and Wang Z L 2013 Theoretical study of contact-mode triboelectric nanogenerators as an effective power source *Energy Environ. Sci.* **6** 3576–83
- [97] Niu S, Liu Y, Wang S, Lin L, Zhou Y S, Hu Y and Wang Z L 2013 Theory of sliding-mode triboelectric nanogenerators *Adv. Mater.* **25** 6184–93
- [98] Niu S, Wang S, Liu Y, Zhou Y S, Lin L, Hu Y, Pradel K C and Wang Z L 2014 A theoretical study of grating structured triboelectric nanogenerators *Energy Environ. Sci.* **7** 2339–49
- [99] Shao J, Jiang T, Tang W, Chen X, Xu L and Wang Z L 2018 Structural figure-of-merits of triboelectric nanogenerators at powering loads *Nano Energy* **51** 688–97
- [100] Niu S, Liu Y, Zhou Y S, Wang S, Lin L and Wang Z L 2014 Optimization of triboelectric nanogenerator charging systems for efficient energy harvesting and storage *IEEE Trans. Electron Devices* **62** 641–7
- [101] Niu S, Liu Y, Chen X, Wang S, Zhou Y S, Lin L, Xie Y and Wang Z L 2015 Theory of freestanding triboelectric-layer-based nanogenerators *Nano Energy* **12** 760–74
- [102] Niu S and Wang Z L 2015 Theoretical systems of triboelectric nanogenerators *Nano Energy* **14** 161–92
- [103] Shao J, Willatzen M, Jiang T, Tang W, Chen X, Wang J and Wang Z L 2019 Quantifying the power output and structural figure-of-merits of triboelectric nanogenerators in a charging system starting from the Maxwell's displacement current *Nano Energy* **59** 380–9
- [104] Shao J, Willatzen M, Shi Y and Wang Z L 2019 3D mathematical model of contact-separation and single-electrode mode triboelectric nanogenerators *Nano Energy* **60** 630–40
- [105] Dharmasena R D I G, Jayawardena K D G I, Mills C A, Deane J H B, Anguita J V, Dorey R A and Silva S R P 2017 Triboelectric nanogenerators: providing a fundamental framework *Energy Environ. Sci.* **10** 1801–11
- [106] Niu S, Zhou Y S, Wang S, Liu Y, Lin L, Bando Y and Wang Z L 2014 Simulation method for optimizing the performance of an integrated triboelectric nanogenerator energy harvesting system *Nano Energy* **8** 150–6
- [107] Niu S, Wang X, Yi F, Zhou Y S and Wang Z L 2015 A universal self-charging system driven by random biomechanical energy for sustainable operation of mobile electronics *Nat. Commun.* **6** 1–8
- [108] Dharmasena R D I G, Jayawardena K D G I, Mills C A, Dorey R A and Silva S R P 2018 A unified theoretical model for triboelectric nanogenerators *Nano Energy* **48** 391–400
- [109] Shao J, Yang Y, Yang O, Wang J, Willatzen M and Wang Z L 2021 Designing rules and optimization of triboelectric nanogenerator arrays *Adv. Energy Mater.* **11** 2100065
- [110] Shao J, Willatzen M and Wang Z L 2020 Theoretical modeling of triboelectric nanogenerators (TENGs) *J. Appl. Phys.* **128** 111101
- [111] Shao J, Liu D, Willatzen M and Wang Z L 2020 Three-dimensional modeling of alternating current triboelectric nanogenerator in the linear sliding mode *Appl. Phys. Rev.* **7** 011405
- [112] Zi Y, Niu S, Wang J, Wen Z, Tang W and Wang Z L 2015 Standards and figure-of-merits for quantifying the performance of triboelectric nanogenerators *Nat. Commun.* **6** 1–8
- [113] Zi Y, Wang J, Wang S, Li S, Wen Z, Guo H and Wang Z L 2016 Effective energy storage from a triboelectric nanogenerator *Nat. Commun.* **7** 1–8
- [114] Zi Y, Guo H, Wen Z, Yeh M-H, Hu C and Wang Z L 2016 Harvesting low-frequency(<5 Hz) irregular mechanical energy: a possible killer application of triboelectric nanogenerator *ACS Nano* **10** 4797–805
- [115] Zi Y, Wu C, Ding W and Wang Z L 2017 Maximized effective energy output of contact-separation-triggered triboelectric nanogenerators as limited by air breakdown *Adv. Funct. Mater.* **27** 1700049
- [116] Xia X, Fu J and Zi Y 2019 A universal standardized method for output capability assessment of nanogenerators *Nat. Commun.* **10** 1–9
- [117] Fu J, Xia X, Xu G, Li X and Zi Y 2019 On the maximal output energy density of nanogenerators *ACS Nano* **13** 13257–63
- [118] Kwak S S, Kim S M, Ryu H, Kim J, Khan U, Yoon H-J, Jeong Y H and Kim S-W 2019 Butylated melamine formaldehyde as a durable and highly positive friction layer for stable, high output triboelectric nanogenerators *Energy Environ. Sci.* **12** 3156–63
- [119] Zheng Y, Cheng L, Yuan M, Wang Z, Zhang L, Qin Y and Jing T 2014 An electrospun nanowire-based triboelectric nanogenerator and its application in a fully self-powered UV detector *Nanoscale* **6** 7842–6
- [120] Wang Z, Cheng L, Zheng Y, Qin Y and Wang Z L 2014 Enhancing the performance of triboelectric nanogenerator through prior-charge injection and its application on self-powered anticorrosion *Nano Energy* **10** 37–43
- [121] Zhang L, Su C, Cheng L, Cui N, Gu L, Qin Y, Yang R and Zhou F 2019 Enhancing the performance of textile triboelectric nanogenerators with oblique microrod arrays for wearable energy harvesting *ACS Appl. Mater. Interfaces* **11** 26824–9
- [122] Cui N, Liu J, Lei Y, Gu L, Xu Q, Liu S and Qin Y 2018 High-performance triboelectric nanogenerator with a rationally designed friction layer structure *ACS Appl. Energy Mater.* **1** 2891–7
- [123] Xu L, Bu T Z, Yang X D, Zhang C and Wang Z L 2018 Ultra-high charge density realized by charge pumping at ambient conditions for triboelectric nanogenerators *Nano Energy* **49** 625–33
- [124] Cheng L, Xu Q, Zheng Y, Jia X and Qin Y 2018 A self-improving triboelectric nanogenerator with improved charge density and increased charge accumulation speed *Nat. Commun.* **9** 1–8
- [125] Bai Y, Xu L, Lin S, Luo J, Qin H, Han K and Wang Z L 2020 Charge pumping strategy for rotation and sliding type triboelectric nanogenerators *Adv. Energy Mater.* **10** 2000605
- [126] Liu W *et al* 2019 Integrated charge excitation triboelectric nanogenerator *Nat. Commun.* **10** 1–9
- [127] Liu Y, Liu W, Wang Z, He W, Tang Q, Xi Y, Wang X, Guo H and Hu C 2020 Quantifying contact status and the air-breakdown model of charge-excitation triboelectric nanogenerators to maximize charge density *Nat. Commun.* **11** 1–8
- [128] Li S, Wang S, Zi Y, Wen Z, Lin L, Zhang G and Wang Z L 2015 Largely improving the robustness and lifetime of triboelectric nanogenerators through automatic transition between contact and noncontact working states *ACS Nano* **9** 7479–87
- [129] Lin Z, Zhang B, Zou H, Wu Z, Guo H, Zhang Y, Yang J and Wang Z L 2020 Rationally designed rotation triboelectric nanogenerators with much extended lifetime and durability *Nano Energy* **68** 104378

- [130] Wu C, Liu R, Wang J, Zi Y, Lin L and Wang Z L 2017 A spring-based resonance coupling for hugely enhancing the performance of triboelectric nanogenerators for harvesting low-frequency vibration energy *Nano Energy* **32** 287–93
- [131] Lin Z, Zhang B, Guo H, Wu Z, Zou H, Yang J and Wang Z L 2019 Super-robust and frequency-multiplied triboelectric nanogenerator for efficient harvesting water and wind energy *Nano Energy* **64** 103908
- [132] Jiang T, Pang H, An J, Lu P, Feng Y, Liang X, Zhong W and Wang Z L 2020 Robust swing-structured triboelectric nanogenerator for efficient blue energy harvesting *Adv. Energy Mater.* **10** 2000064
- [133] Wu J, Xi Y and Shi Y 2020 Toward wear-resistive, highly durable and high performance triboelectric nanogenerator through interface liquid lubrication *Nano Energy* **72** 104659
- [134] Cheng X, Tang W, Song Y, Chen H, Zhang H and Wang Z L 2019 Power management and effective energy storage of pulsed output from triboelectric nanogenerator *Nano Energy* **61** 517–32
- [135] Harmon W, Bamgboje D, Guo H, Hu T and Wang Z L 2020 Self-driven power management system for triboelectric nanogenerators *Nano Energy* **71** 104642
- [136] Xi F, Pang Y, Li W, Jiang T, Zhang L, Guo T, Liu G, Zhang C and Wang Z L 2017 Universal power management strategy for triboelectric nanogenerator *Nano Energy* **37** 168–76
- [137] Xi F, Pang Y, Liu G, Wang S, Li W, Zhang C and Wang Z L 2019 Self-powered intelligent buoy system by water wave energy for sustainable and autonomous wireless sensing and data transmission *Nano Energy* **61** 1–9
- [138] Liang X, Jiang T, Liu G, Feng Y, Zhang C and Wang Z L 2020 Spherical triboelectric nanogenerator integrated with power management module for harvesting multidirectional water wave energy *Energy Environ. Sci.* **13** 277–85
- [139] Wang Z L 2008 Self-powered nanotech *Sci. Am.* **298** 82–7
- [140] Zheng Q *et al* 2014 *In vivo* powering of pacemaker by breathing-driven implanted triboelectric nanogenerator *Adv. Mater.* **26** 5851–6
- [141] Ma Y *et al* 2016 Self-powered, one-stop, and multifunctional implantable triboelectric active sensor for real-time biomedical monitoring *Nano Lett.* **16** 6042–51
- [142] Zheng Q *et al* 2016 *In vivo* self-powered wireless cardiac monitoring via implantable triboelectric nanogenerator *ACS Nano* **10** 6510–8
- [143] Ouyang H *et al* 2019 Symbiotic cardiac pacemaker *Nat. Commun.* **10** 1–10
- [144] Zheng Q *et al* 2016 Biodegradable triboelectric nanogenerator as a life-time designed implantable power source *Sci. Adv.* **2** e1501478
- [145] Hinchet R, Yoon H-J, Ryu H, Kim M-K, Choi E-K, Kim D-S and Kim S-W 2019 Transcutaneous ultrasound energy harvesting using capacitive triboelectric technology *Science* **365** 491–4
- [146] Dong K *et al* 2017 3D orthogonal woven triboelectric nanogenerator for effective biomechanical energy harvesting and as self-powered active motion sensors *Adv. Mater.* **29** 1702648
- [147] Dong K *et al* 2018 A stretchable yarn embedded triboelectric nanogenerator as electronic skin for biomechanical energy harvesting and multifunctional pressure sensing *Adv. Mater.* **30** 1804944
- [148] Dong K, Peng X and Wang Z L 2020 Fiber/fabric-based piezoelectric and triboelectric nanogenerators for flexible/stretchable and wearable electronics and artificial intelligence *Adv. Mater.* **32** 1902549
- [149] Huang L, Lin S, Xu Z, Zhou H, Duan J, Hu B and Zhou J 2020 Fiber-based energy conversion devices for human-body energy harvesting *Adv. Mater.* **32** 1902034
- [150] Xu X, Xie S, Zhang Y and Peng H 2019 The rise of fiber electronics *Angew. Chem., Int. Ed.* **58** 13643–53
- [151] Kwak S S, Yoon H-J and Kim S-W 2019 Textile-based triboelectric nanogenerators for self-powered wearable electronics *Adv. Funct. Mater.* **29** 1804533
- [152] Kwak S S, Kim H, Seung W, Kim J, Hinchet R and Kim S-W 2017 Fully stretchable textile triboelectric nanogenerator with knitted fabric structures *ACS Nano* **11** 10733–41
- [153] Song Y, Wang H, Cheng X, Li G, Chen X, Chen H, Miao L, Zhang X and Zhang H 2019 High-efficiency self-charging smart bracelet for portable electronics *Nano Energy* **55** 29–36
- [154] Pu X, Li L, Song H, Du C, Zhao Z, Jiang C, Cao G, Hu W and Wang Z L 2015 A self-charging power unit by integration of a textile triboelectric nanogenerator and a flexible lithium-ion battery for wearable electronics *Adv. Mater.* **27** 2472–8
- [155] Seung W *et al* 2015 Nanopatterned textile-based wearable triboelectric nanogenerator *ACS Nano* **9** 3501–9
- [156] Yu A *et al* 2017 Core–shell–yarn-based triboelectric nanogenerator textiles as power cloths *ACS Nano* **11** 12764–71
- [157] Cui N, Liu J, Gu L, Bai S, Chen X and Qin Y 2015 Wearable triboelectric generator for powering the portable electronic devices *ACS Appl. Mater. Interfaces* **7** 18225–30
- [158] Shi J *et al* 2020 Smart textile-integrated microelectronic systems for wearable applications *Adv. Mater.* **32** 1901958
- [159] Pu X, Li L, Liu M, Jiang C, Du C, Zhao Z, Hu W and Wang Z L 2016 Wearable self-charging power textile based on flexible yarn supercapacitors and fabric nanogenerators *Adv. Mater.* **28** 98–105
- [160] Wen Z *et al* 2016 Self-powered textile for wearable electronics by hybridizing fiber-shaped nanogenerators, solar cells, and supercapacitors *Sci. Adv.* **2** e1600097
- [161] Chen J, Huang Y, Zhang N, Zou H, Liu R, Tao C, Fan X and Wang Z L 2016 Micro-cable structured textile for simultaneously harvesting solar and mechanical energy *Nat. Energy* **1** 1–8
- [162] Zhao Z, Yan C, Liu Z, Fu X, Peng L-M, Hu Y and Zheng Z 2016 Machine-washable textile triboelectric nanogenerators for effective human respiratory monitoring through loom weaving of metallic yarns *Adv. Mater.* **28** 10267–74
- [163] He T, Shi Q, Wang H, Wen F, Chen T, Ouyang J and Lee C 2019 Beyond energy harvesting—multi-functional triboelectric nanosensors on a textile *Nano Energy* **57** 338–52
- [164] He T, Wen F, Wang H, Shi Q, Sun Z, Zhang Z, Zhang T and Lee C 2020 Self-powered wireless IoT sensor based on triboelectric textile 2020 IEEE 33rd Int. Conf. on Micro Electro Mechanical Systems (MEMS) (Piscataway, NJ: IEEE) pp 267–70
- [165] Shi Q and Lee C 2019 Self-powered bio-inspired spider-net-coding interface using single-electrode triboelectric nanogenerator *Adv. Sci.* **6** 1900617
- [166] Shi Q, Qiu C, He T, Wu F, Zhu M, Dziuban J A, Walczak R, Yuce M R and Lee C 2019 Triboelectric single-electrode-output control interface using patterned grid electrode *Nano Energy* **60** 545–56
- [167] Bai Y, Xu L, He C, Zhu L, Yang X, Jiang T, Nie J, Zhong W and Wang Z L 2019 High-performance triboelectric nanogenerators for self-powered, *in situ* and real-time water quality mapping *Nano Energy* **66** 104117
- [168] Zhou Z *et al* 2018 Wireless self-powered sensor networks driven by triboelectric nanogenerator for *in situ* real time survey of environmental monitoring *Nano Energy* **53** 501–7
- [169] Lin Z *et al* 2018 Flexible timbo-like triboelectric nanogenerator as self-powered force and bend sensor for wireless and distributed landslide monitoring *Adv. Mater. Technol.* **3** 1800144
- [170] Yang Y *et al* 2013 Human skin based triboelectric nanogenerators for harvesting biomechanical energy and as self-powered active tactile sensor system *ACS Nano* **7** 9213–22

- [171] Liu D, Chen B, An J, Li C, Liu G, Shao J, Tang W, Zhang C and Wang Z L 2020 Wind-driven self-powered wireless environmental sensors for internet of things at long distance *Nano Energy* **73** 104819
- [172] Yang Y *et al* 2013 Triboelectric nanogenerator for harvesting wind energy and as self-powered wind vector sensor system *ACS Nano* **7** 9461–8
- [173] Yang J, Chen J, Su Y, Jing Q, Li Z, Yi F, Wen X, Wang Z and Wang Z L 2015 Eardrum-inspired active sensors for self-powered cardiovascular system characterization and throat-attached anti-interference voice recognition *Adv. Mater.* **27** 1316–26
- [174] Zhang X-S, Han M-D, Wang R-X, Zhu F-Y, Li Z-H, Wang W and Zhang H-X 2013 Frequency-multiplication high-output triboelectric nanogenerator for sustainably powering biomedical microsystems *Nano Lett.* **13** 1168–72
- [175] Meng K *et al* 2019 Flexible weaving constructed self-powered pressure sensor enabling continuous diagnosis of cardiovascular disease and measurement of cuffless blood pressure *Adv. Funct. Mater.* **29** 1806388
- [176] Meng B, Tang W, Too Z-h, Zhang X, Han M, Liu W and Zhang H 2013 A transparent single-friction-surface triboelectric generator and self-powered touch sensor *Energy Environ. Sci.* **6** 3235–40
- [177] Shi M, Zhang J, Chen H, Han M, Shankaregowda S A, Su Z, Meng B, Cheng X and Zhang H 2016 Self-powered analogue smart skin *ACS Nano* **10** 4083–91
- [178] Wu H, Su Z, Shi M, Miao L, Song Y, Chen H, Han M and Zhang H 2018 Self-powered noncontact electronic skin for motion sensing *Adv. Funct. Mater.* **28** 1704641
- [179] Meng K, Wu Y, He Q, Zhou Z, Wang X, Zhang G, Fan W, Liu J and Yang J 2019 Ultrasensitive fingertip-contacted pressure sensors to enable continuous measurement of epidermal pulse waves on ubiquitous object surfaces *ACS Appl. Mater. Interfaces* **11** 46399–407
- [180] Meng K *et al* 2020 A wireless textile-based sensor system for self-powered personalized health care *SSRN Electronic Journal* **2** 896–907
- [181] Fan W, He Q, Meng K, Tan X, Zhou Z, Zhang G, Yang J and Wang Z L 2020 Machine-knitted washable sensor array textile for precise epidermal physiological signal monitoring *Sci. Adv.* **6** eaay2840
- [182] Fish R M and Geddes L A 2009 Conduction of electrical current to and through the human body: a review *Eplasty* **9** e44
- [183] Guimerà A, Calderón E, Los P and Christie A M 2008 Method and device for bio-impedance measurement with hard-tissue applications *Physiol. Meas.* **29** S279
- [184] Zhang R, Örtегren J, Hummelgård M, Olsen M, Andersson H and Olin H 2018 Harvesting triboelectricity from the human body using non-electrode triboelectric nanogenerators *Nano Energy* **45** 298–303
- [185] Zhang R, Hummelgård M, Örtегren J, Olsen M, Andersson H, Yang Y and Olin H 2018 Human body constituted triboelectric nanogenerators as energy harvesters, code transmitters, and motion sensors *ACS Appl. Energy Mater.* **1** 2955–60
- [186] Grimnes S 1983 Dielectric breakdown of human skin *in vivo* *Med. Biol. Eng. Comput.* **21** 379–81
- [187] Yang L, Liu H, Xing L, Ren H and Zhang J 2013 Numerical calculations of human-body capacitance in mining tunnel environment *J. Phys.: Conf. Ser.* **418** 012002
- [188] Zhang R *et al* 2019 Sensing body motions based on charges generated on the body *Nano Energy* **63** 103842
- [189] He X *et al* 2017 An ultrathin paper-based self-powered system for portable electronics and wireless human-machine interaction *Nano Energy* **39** 328–36
- [190] Guo X *et al* 2016 A human-machine interface based on single channel EOG and patchable sensor *Biomed. Signal Process. Control* **30** 98–105
- [191] Belkacem A N, Shin D, Kambara H, Yoshimura N and Koike Y 2015 Online classification algorithm for eye-movement-based communication systems using two temporal EEG sensors *Biomed. Signal Process. Control* **16** 40–7
- [192] Usakli A B and Gurkan S 2009 Design of a novel efficient human-computer interface: an electrooculogram based virtual keyboard *IEEE Trans. Instrum. Meas.* **59** 2099–108
- [193] Birbaumer N 2006 Brain-computer-interface research: coming of age *Clin. Neurophysiol.* **117** 479–83
- [194] Barea R, Boquete L, Mazo M and López E 2002 System for assisted mobility using eye movements based on electrooculography *IEEE Trans. Neural Syst. Rehabil. Eng.* **10** 209–18
- [195] Pu X, Guo H, Chen J, Wang X, Xi Y, Hu C and Wang Z L 2017 Eye motion triggered self-powered mechnosensational communication system using triboelectric nanogenerator *Sci. Adv.* **3** e1700694
- [196] Wu C, Ding W, Liu R, Wang J, Wang A C, Wang J, Li S, Zi Y and Wang Z L 2018 Keystroke dynamics enabled authentication and identification using triboelectric nanogenerator array *Mater. Today* **21** 216–22
- [197] Chen J, Zhu G, Yang J, Jing Q, Bai P, Yang W, Qi X, Su Y and Wang Z L 2015 Personalized keystroke dynamics for self-powered human-machine interfacing *ACS Nano* **9** 105–16
- [198] Fan X, Chen J, Yang J, Bai P, Li Z and Wang Z L 2015 Ultrathin, rollable, paper-based triboelectric nanogenerator for acoustic energy harvesting and self-powered sound recording *ACS Nano* **9** 4236–43
- [199] Arora N *et al* 2018 SATURN: a thin and flexible self-powered microphone leveraging triboelectric nanogenerator *Proc. ACM Interact. Mob. Wearable Ubiquitous Technol.* **2** 1–28
- [200] Lai Y-C, Deng J, Niu S, Peng W, Wu C, Liu R, Wen Z and Wang Z L 2016 Electric eel-skin-inspired mechanically durable and super-stretchable nanogenerator for deformable power source and fully autonomous conformable electronic-skin applications *Adv. Mater.* **28** 10024–32
- [201] Mannsfeld S C B, Tee B C-K, Stoltzenberg R M, Chen C V H-H, Barman S, Muir B V O, Sokolov A N, Reese C and Bao Z 2010 Highly sensitive flexible pressure sensors with microstructured rubber dielectric layers *Nat. Mater.* **9** 859–64
- [202] Chortos A and Bao Z 2014 Skin-inspired electronic devices *Mater. Today* **17** 321–31
- [203] Truby R L, Wehner M, Grosskopf A K, Vogt D M, Uzel S G M, Wood R J and Lewis J A 2018 Soft somatosensitive actuators via embedded 3D printing *Adv. Mater.* **30** 1706383
- [204] Larson C, Peeble B, Li S, Robinson S, Totaro M, Beccai L, Mazzolai B and Shepherd R 2016 Highly stretchable electroluminescent skin for optical signaling and tactile sensing *Science* **351** 1071–4
- [205] Yuan Z, Zhou T, Yin Y, Cao R, Li C and Wang Z L 2017 Transparent and flexible triboelectric sensing array for touch security applications *ACS Nano* **11** 8364–9
- [206] Wang X, Zhang Y, Zhang X, Huo Z, Li X, Que M, Peng Z, Wang H and Pan C 2018 A highly stretchable transparent self-powered triboelectric tactile sensor with metallized nanofibers for wearable electronics *Adv. Mater.* **30** 1706738
- [207] Fang H, Wang X, Li Q, Peng D, Yan Q and Pan C 2016 A stretchable nanogenerator with electric/light dual-mode energy conversion *Adv. Energy Mater.* **6** 1600829
- [208] Zhu G, Yang W Q, Zhang T, Jing Q, Chen J, Zhou Y S, Bai P and Wang Z L 2014 Self-powered, ultrasensitive, flexible tactile sensors based on contact electrification *Nano Lett.* **14** 3208–13
- [209] Pu X, Liu M, Chen X, Sun J, Du C, Zhang Y, Zhai J, Hu W and Wang Z L 2017 Ultrastretchable, transparent triboelectric nanogenerator as electronic skin for biomechanical energy harvesting and tactile sensing *Sci. Adv.* **3** e1700015

- [210] Parida K, Kumar V, Jiangxin W, Bhavanasi V, Bendi R and Lee P S 2017 Highly transparent, stretchable, and self-healing ionic-skin triboelectric nanogenerators for energy harvesting and touch applications *Adv. Mater.* **29** 1702181
- [211] Lai Y-C, Deng J, Liu R, Hsiao Y-C, Zhang S L, Peng W, Wu H-M, Wang X and Wang Z L 2018 Actively perceiving and responsive soft robots enabled by self-powered, highly extensible, and highly sensitive triboelectric proximity- and pressure-sensing skins *Adv. Mater.* **30** 1801114
- [212] Wang Z, An J, Nie J, Luo J, Shao J, Jiang T, Chen B, Tang W and Wang Z L 2020 A self-powered angle sensor at nanoradian-resolution for robotic arms and personalized medicare *Adv. Mater.* **32** 2001466
- [213] Wang Z L 2015 Triboelectric nanogenerators as new energy technology and self-powered sensors—Principles, problems and perspectives *Faraday Discuss.* **176** 447–58
- [214] Wang Z L 2017 Catch wave power in floating nets *Nature* **542** 159–60
- [215] Wang X, Niu S, Yin Y, Yi F, You Z and Wang Z L 2015 Triboelectric nanogenerator based on fully enclosed rolling spherical structure for harvesting low-frequency water wave energy *Adv. Energy Mater.* **5** 1501467
- [216] Xu L, Jiang T, Lin P, Shao J J, He C, Zhong W, Chen X Y and Wang Z L 2018 Coupled triboelectric nanogenerator networks for efficient water wave energy harvesting *ACS Nano* **12** 1849–58
- [217] Yang X, Xu L, Lin P, Zhong W, Bai Y, Luo J, Chen J and Wang Z L 2019 Macroscopic self-assembly network of encapsulated high-performance triboelectric nanogenerators for water wave energy harvesting *Nano Energy* **60** 404–12
- [218] Cheng P *et al* 2019 Largely enhanced triboelectric nanogenerator for efficient harvesting of water wave energy by soft contacted structure *Nano Energy* **57** 432–9
- [219] Xu L, Pang Y, Zhang C, Jiang T, Chen X, Luo J, Tang W, Cao X and Wang Z L 2017 Integrated triboelectric nanogenerator array based on air-driven membrane structures for water wave energy harvesting *Nano Energy* **31** 351–8
- [220] Xiao T X, Liang X, Jiang T, Xu L, Shao J J, Nie J H, Bai Y, Zhong W and Wang Z L 2018 Spherical triboelectric nanogenerators based on spring-assisted multilayered structure for efficient water wave energy harvesting *Adv. Funct. Mater.* **28** 1802634
- [221] Zhao X J, Zhu G, Fan Y J, Li H Y and Wang Z L 2015 Triboelectric charging at the nanostructured solid/liquid interface for area-scalable wave energy conversion and its use in corrosion protection *ACS Nano* **9** 7671–7
- [222] Zhao X J, Tian J J, Kuang S Y, Ouyang H, Yan L, Wang Z L, Li Z and Zhu G 2016 Biocide-free antifouling on insulating surface by wave-driven triboelectrification-induced potential oscillation *Adv. Mater. Interfaces* **3** 1600187
- [223] Tang W, Han Y, Han C B, Gao C Z, Cao X and Wang Z L 2015 Self-powered water splitting using flowing kinetic energy *Adv. Mater.* **27** 272–6
- [224] Jiang Q, Han Y, Tang W, Zhu H, Gao C, Chen S, Willander M, Cao X and Lin Wang Z 2015 Self-powered seawater desalination and electrolysis using flowing kinetic energy *Nano Energy* **15** 266–74
- [225] Cheng J, Ding W, Zi Y, Lu Y, Ji L, Liu F, Wu C and Wang Z L 2018 Triboelectric microplasma powered by mechanical stimuli *Nat. Commun.* **9** 1–11
- [226] Cheng G, Zheng H, Yang F, Zhao L, Zheng M, Yang J, Qin H, Du Z and Wang Z L 2018 Managing and maximizing the output power of a triboelectric nanogenerator by controlled tip-electrode air-discharging and application for UV sensing *Nano Energy* **44** 208–16
- [227] Zhao K, Gu G, Zhang Y, Zhang B, Yang F, Zhao L, Zheng M, Cheng G and Du Z 2018 The self-powered CO<sub>2</sub> gas sensor based on gas discharge induced by triboelectric nanogenerator *Nano Energy* **53** 898–905
- [228] Yang F, Zheng M, Zhao L, Guo J, Zhang B, Gu G, Cheng G and Du Z 2019 The high-speed ultraviolet photodetector of ZnO nanowire Schottky barrier based on the triboelectric-nanogenerator-powered surface-ionic-gate *Nano Energy* **60** 680–8
- [229] Zhao L *et al* 2019 The novel transistor and photodetector of monolayer MoS<sub>2</sub> based on surface-ionic-gate modulation powered by a triboelectric nanogenerator *Nano Energy* **62** 38–45
- [230] Yang F *et al* 2020 Tuning oxygen vacancies and improving UV sensing of ZnO nanowire by micro-plasma powered by a triboelectric nanogenerator *Nano Energy* **67** 104210
- [231] Zhan F, Wang A C, Xu L, Lin S, Shao J, Chen X and Wang Z L 2020 Electron transfer as a liquid droplet contacting a polymer surface *ACS Nano* **14** 17565–73
- [232] Lin S and Wang Z L 2021 Scanning triboelectric nanogenerator as a nanoscale probe for measuring local surface charge density on a dielectric film *Appl. Phys. Lett.* **118** 193901
- [233] Zhang C, Tang W, Han C, Fan F and Wang Z L 2014 Theoretical comparison, equivalent transformation, and conjunction operations of electromagnetic induction generator and triboelectric nanogenerator for harvesting mechanical energy *Adv. Mater.* **26** 3580–91
- [234] Zhao J, Zhen G, Liu G, Bu T, Liu W, Fu X, Zhang P, Zhang C and Wang Z L 2019 Remarkable merits of triboelectric nanogenerator than electromagnetic generator for harvesting small-amplitude mechanical energy *Nano Energy* **61** 111–8
- [235] Zhang K, Wang X, Yang Y and Wang Z L 2015 Hybridized electromagnetic–triboelectric nanogenerator for scavenging biomechanical energy for sustainably powering wearable electronics *ACS Nano* **9** 3521–9
- [236] Wu Y, Wang X, Yang Y and Wang Z L 2015 Hybrid energy cell for harvesting mechanical energy from one motion using two approaches *Nano Energy* **11** 162–70
- [237] Wang X, Wang S, Yang Y and Wang Z L 2015 Hybridized electromagnetic–triboelectric nanogenerator for scavenging airflow energy to sustainably power temperature sensors *ACS Nano* **9** 4553–62
- [238] Wang X and Yang Y 2017 Effective energy storage from a hybridized electromagnetic–triboelectric nanogenerator *Nano Energy* **32** 36–41
- [239] Zhang K and Yang Y 2016 Linear-grating hybridized electromagnetic–triboelectric nanogenerator for sustainably powering portable electronics *Nano Res.* **9** 974–84
- [240] Zhong X, Yang Y, Wang X and Wang Z L 2015 Rotating-disk-based hybridized electromagnetic–triboelectric nanogenerator for scavenging biomechanical energy as a mobile power source *Nano Energy* **13** 771–80
- [241] Wang X, Wang Z L and Yang Y 2016 Hybridized nanogenerator for simultaneously scavenging mechanical and thermal energies by electromagnetic–triboelectric–thermoelectric effects *Nano Energy* **26** 164–71
- [242] Quan T, Wang X, Wang Z L and Yang Y 2015 Hybridized electromagnetic–triboelectric nanogenerator for a self-powered electronic watch *ACS Nano* **9** 12301–10
- [243] Han M, Zhang X-S, Meng B, Liu W, Tang W, Sun X, Wang W and Zhang H 2013 r-Shaped hybrid nanogenerator with enhanced piezoelectricity *ACS Nano* **7** 8554–60
- [244] Chen X, Song Y, Su Z, Chen H, Cheng X, Zhang J, Han M and Zhang H 2017 Flexible fiber-based hybrid nanogenerator for biomechanical energy harvesting and physiological monitoring *Nano Energy* **38** 43–50
- [245] Zheng L, Lin Z-H, Cheng G, Wu W, Wen X, Lee S and Wang Z L 2014 Silicon-based hybrid cell for harvesting solar energy and raindrop electrostatic energy *Nano Energy* **9** 291–300
- [246] Lin S, Chen X and Wang Z L 2021 Contact-electrification at liquid-solid interface *Chem. Rev.* <https://doi.org/10.1021/acs.chemrev.1c00176>

- [247] Zhao X, Lu X, Zheng Q, Fang L, Zheng L, Chen X and Wang Z L 2021 Studying of contact electrification and electron transfer at liquid–liquid interface *Nano Energy* **87** 106191
- [248] Lin S and Wang Z L 2021 Scanning triboelectric nanogenerator as a nanoscale probe for measuring local surface charge density on a dielectric film *Appl. Phys. Lett.* **118** 193901



**Dr. Zhong Lin Wang** is the Director of the Beijing Institute of Nanoenergy and Nanosystems, and Regents' Professor and Hightower Chair at Georgia Institute of Technology. Dr. Wang pioneered the nanogenerators field for distributed energy, self-powered sensors and large-scale blue energy. He coined the fields of piezotronics and piezophototronics for the third generation semiconductors. Among 100,000 scientists across all fields worldwide, Wang is ranked #5 in career scientific impact, #1 in Nanoscience, and #2 in Materials Science. His google scholar citation is over 300,000 with an h-index of over 263. Dr. Wang has received the Celsius Lecture Laureate, Uppsala University, Sweden (2020); The Albert Einstein World Award of Science (2019); Diels-Planck lecture award (2019); ENI award in Energy Frontiers (2018); The James C. McGroddy Prize in New Materials from American Physical Society (2014); and MRS Medal from Materials Research Soci. (2011). Dr. Wang was elected as a foreign member of the Chinese Academy of Sciences in 2009, member of European Academy of Sciences in 2002, academician of Academia of Sinica 2018, International fellow of Canadian Academy of Engineering 2019; Foreign member of the Korean Academy of Science and Technology 2019. Dr. Wang is the founding editor and chief editor of an international journal *Nano Energy*, which now has an impact factor of 16.6. Details can be found at: <http://www.nanoscience.gatech.edu>